THE CMS-HF ONLINE RADIATION DAMAGE MONITORING SYSTEM MEASUREMENT RESULTS FOR 2022 AND 2023

by

Berat Gönültaş

B.S., Physics, Boğaziçi University, 2021

Submitted to the Institute for Graduate Studies in Science and Engineering in partial fulfillment of the requirements for the degree of Master of Science

Graduate Program in Physics

Boğaziçi University

2024

THE CMS-HF ONLINE RADIATION DAMAGE MONITORING SYSTEM MEASUREMENT RESULTS FOR 2022 AND 2023

APPROVED BY:

Prof. Erhan Gülmez (Thesis Supervisor)	....
Assist. Prof. Bora Akgün	....
Prof. Mithat Kaya	....

DATE OF APPROVAL: 13.05.2024

ACKNOWLEDGEMENTS

I would like to express my deepest gratitude to my advisor Prof. Erhan Gülmez for his guidance, support and concern which motivated me a lot. It was a great chance for me to work with him.

I am also grateful to all of my teachers contributed in me throughout my journey. Some of my teachers and professors were magnificent people whom I remember with admiration and longing. I would like to thank especially to my first teacher: my mom, Fatma. She was the first person from whom I learned a lot.

Lastly, I also thank my darling Zeynep for her endless support.

This work was supported in part by Turkish Energy, Nuclear and Mineral Research Agency (TENMAK) and Bogazici University Research Fund Grant Number: 18581 (21B03P2).

ABSTRACT

THE CMS-HF ONLINE RADIATION DAMAGE MONITORING SYSTEM MEASUREMENT RESULTS FOR 2022 AND 2023

The HF calorimeter of the CMS detector is designed to detect the most energetic particles generated by the proton-proton collisions at CERN. Particle showers produce Cherenkov Light in the quartz fibers. The signals are produced in the PMTs by the Cherenkov Light passing through the quartz fibers in the HF calorimeter. The transparency of the quartz fibers decreases due to the radiation damage. With regards to the accuracy of the energy calibration, it is important to monitor the radiation damage of these quartz fibers. To do this, a radiation damage monitoring system was implemented. In this thesis, the analysis and results of the 2022 and 2023 data from the HF Radiation Damage Monitoring System are presented. 2022 data are the first data after Long Shutdown II. The ROOT is used as the data analysis framework. Results are presented with respect to time and also with respect to the integrated luminosity.

ÖZET

2022 VE 2023 İÇİN CMS-HF ÇEVRİMİÇİ RADYASYON HASARI İZLEME SİSTEMİ ÖLÇÜM SONUÇLARI

CMS dedektörünün HF kalorimetresi CERN'deki proton-proton çarpışmaları sonucunda ortaya çıkan en yüksek enerjiye sahip parçacıkları tespit etmek üzere tasarlanmıştır. HF kalorimetresinde oluşan parçacık sağanağı kuartz fiberlerde Cherenkov Işımasına yol açar. Bu ışık kuarz fiberlerden geçerek PMT'ler aracılığıyla sinyallere dönüşür. Kuarz fiberlerin saydamlığı radyasyon hasarı arttıkça azalır. Kuarz fiberlerdeki radyasyon hasarını izlemek enerji kalibrasyonunun doğruluğu açısından önemlidir. Bunun için bir radyasyon hasarı izleme sistemi kurulmuştur. Bu tezde HF Radyasyon Hasarı İzleme Sisteminin 2022 ve 2023 verilerinin analiz ve sonuçları sunulmaktadır. 2022 verisi Uzun Ara II'den (LS II) sonraki ilk veridir. Veri analizi için ROOT kullanılmıştır. Sonuçlar zamana ve kümülatif lüminositeye göre verilmiştir.

TABLE OF CONTENTS

LIST OF FIGURES

LIST OF TABLES

LIST OF SYMBOLS

B	Magnetic Field
E	Energy
F_B	Lorentz Force
fb	Femto Barn
fC	Femto Coulomb
K	Kelvin
ln	Natural logarithm
m	Meter
n	Refractive index of the medium
ns	Nano Second
p	Momentum
Q, q	Charge
s	Second
tan	tangent function
TeV	Tera Electron Volt
v	Velocity
η	Pseudorapidity
θ	Angle
μm	Micrometer
ϕ	Azimuthal angle

LIST OF ACRONYMS/ABBREVIATIONS

ALICE	A Large Ion Collider Experiment
ATLAS	A Toroidal LHC Apparatus
CERN	Conseil Européen pour la Recherche Nucléaire (European Organization for Nuclear Research)
CMS	Compact Muon Solenoid
ECAL	Electromagnetic Calorimeter
EM	Electromagnetic
HCAL	Hadron Calorimeter
HF	Hadron Forward
IP	Interaction Point
LHC	Large Hadron Collider
LHCb	Large Hadron Collider beauty
Linac4	Linear Accelerator 4
LS	Long Shutdown
LXPLUS	Linux Public Login User Service
PMT	Photo Multiplier Tube
PS	Proton Synchrotron
PSB	Proton Synchrotron Booster
QIE	Charge Integrator and Encoder
RF	Radio Frequency
RMS	Root Mean Square
SPS	Super Proton Synchrotron
SSH	Secure Shell Protocol
TDC	Time-to-Digital Converter
TS	Time Slot

1. INTRODUCTION

The LHC is the largest and most powerful particle accelerator ever built. On the LHC ring, there are four collision points where the four detectors, namely ATLAS, CMS, ALICE and LHCb are situated.

The CMS detector has several layers, one of which is the HCAL. In the HCAL subdetector, the parts at both ends of the CMS detector are called as the HF calorimeter. The HF calorimeters are exposed to the highest level of radiation. This huge amount of radiation damages the quartz fibers in the HF calorimeters and reduces their transparency. It is important to monitor this radiation damage. For this purpose, the HF Online Radiation Damage Monitoring system was constructed. The latest upgrades to this system were made in the Year End Technical Stop 2017-2018. Since then, various results have been published. [1–5] This thesis includes the analysis and the results of 2022 and 2023 HF RadDam data.

Chapters 2 and 3 give some brief information about the LHC and the CMS. Details on the HCAL and the HF Calorimeter are introduced in Chapters 4 and 5. Chapter 6 focuses on the radiation damage monitoring in the HF calorimeter. In Chapter 7, the analysis method is discussed and the results are shown.

2. THE LARGE HADRON COLLIDER

The 27-km long LHC is the world's largest and most powerful particle accelerator which is also the final part of the CERN accelerator complex shown in Figure 2.1 [6].

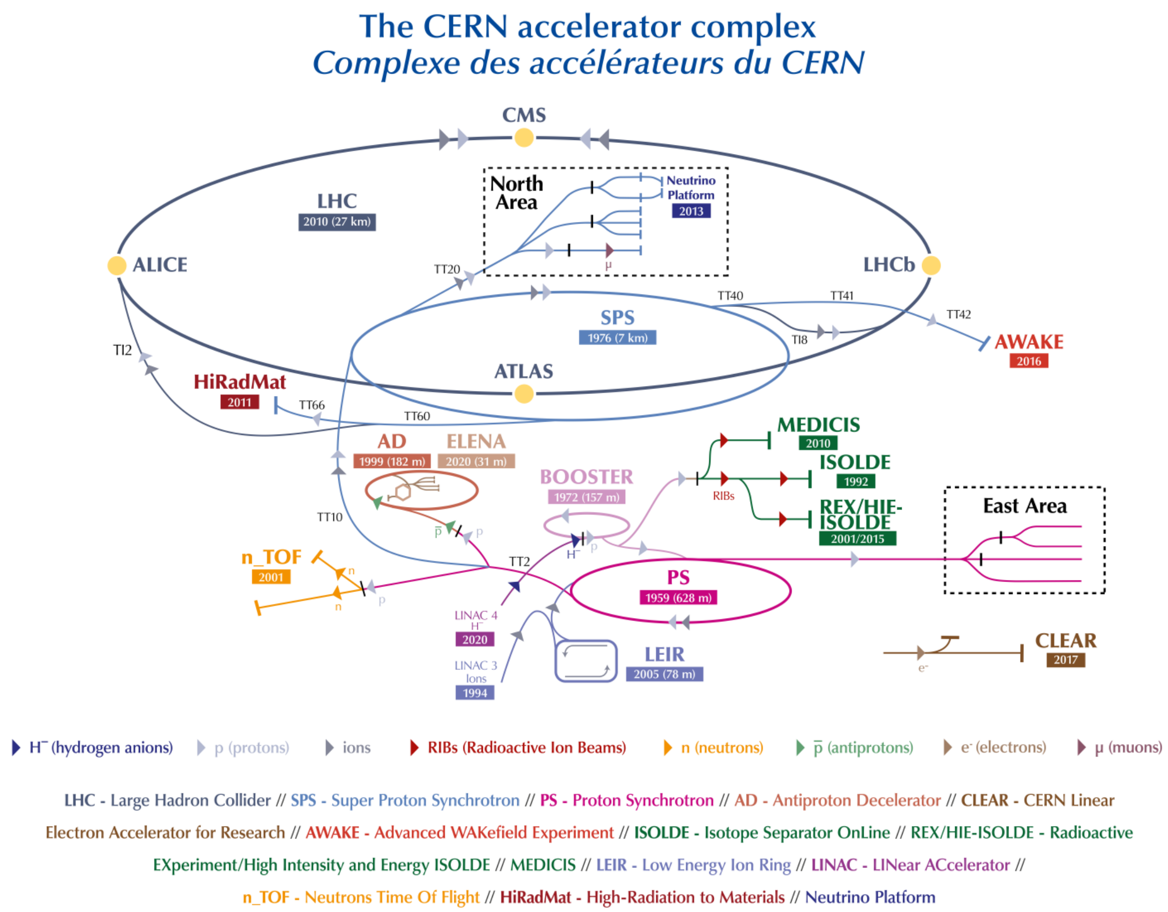

Figure 2.1. The CERN accelerator complex layout in 2022.
(CERN provides the image free of charge for educational and informational use.)

Before reaching their maximum energy in the LHC, the beams are first created in Linear Accelerator 4 (Linac4), which accelerates negative hydrogen ions to 160 MeV. In this regard, Linac4 is the main source of the beams. Passing from Linac4 to the Proton Synchrotron Booster (PSB), two electrons are taken away from the ions so that only protons are left. The PSB accelerates the protons to 2 GeV and transfers them to the Proton Synchrotron (PS). The PS further accelerates the beams to 26 GeV and sends them to Super Proton Synchrotron (SPS) where the beams get up to 450 GeV. After the SPS, the beams are finally sent to the LHC where they get accelerated to 6.5 TeV, which corresponds to a total energy of 13 TeV at the collision point. A view of the LHC beam pipe at the CMS detector is given in Figure 2.2 [7].

Figure 2.2. A close view of the LHC beam pipe at the CMS detector.
(CERN provides the image free of charge for educational and informational use.)

ATLAS and CMS are general-purpose detectors which have the same scientific goals but different technical solutions and designs. Standard Model, extra dimensions and dark matter are some of their research areas. ATLAS detector, which is in Figure 2.3 [8], is the largest volume particle detector with 46 m long and 25 m diameter. It has six different subsystems and recorded first collisions at 0.9 TeV in 2009.

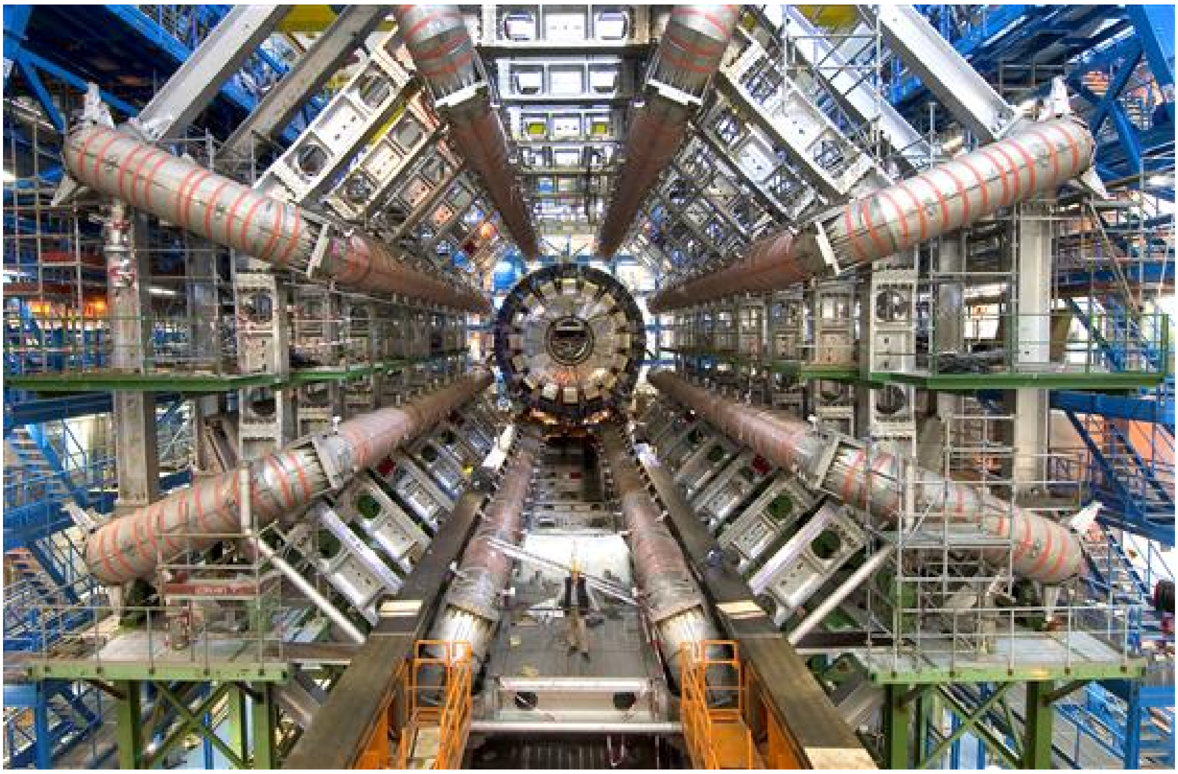

Figure 2.3. A general view from the ATLAS detector.
(CERN CC-BY-4.0.)

ALICE is the detector for heavy-ion physics. It is designed to study the quark-gluon plasma. The quark-gluon plasma is a phase of matter formed at extemely high energy densities. It is thought that the universe is in quark-gluon plasma state just after the Big Bang. ALICE, which can be seen in Figure 2.4 [9], studies how quark-gluon plasma transforms and produces particles, as quarks and gluons become bound together.

LHCb studies “beauty quark” (or “b quark”) to investigate the differences between matter and antimatter. Unlike CMS or ATLAS, LHCb doesn’t have an enclosed detector system surrounding the beam pipe at the entire collision point. Instead, it has several subdetectors involving a forward spectrometer and planar detectors. Since b quarks generated by the collisions go to forward region, the subdetectors of the LHCb are near the beam pipe. A view from the LHCb detector is in Figure 2.5 [10].

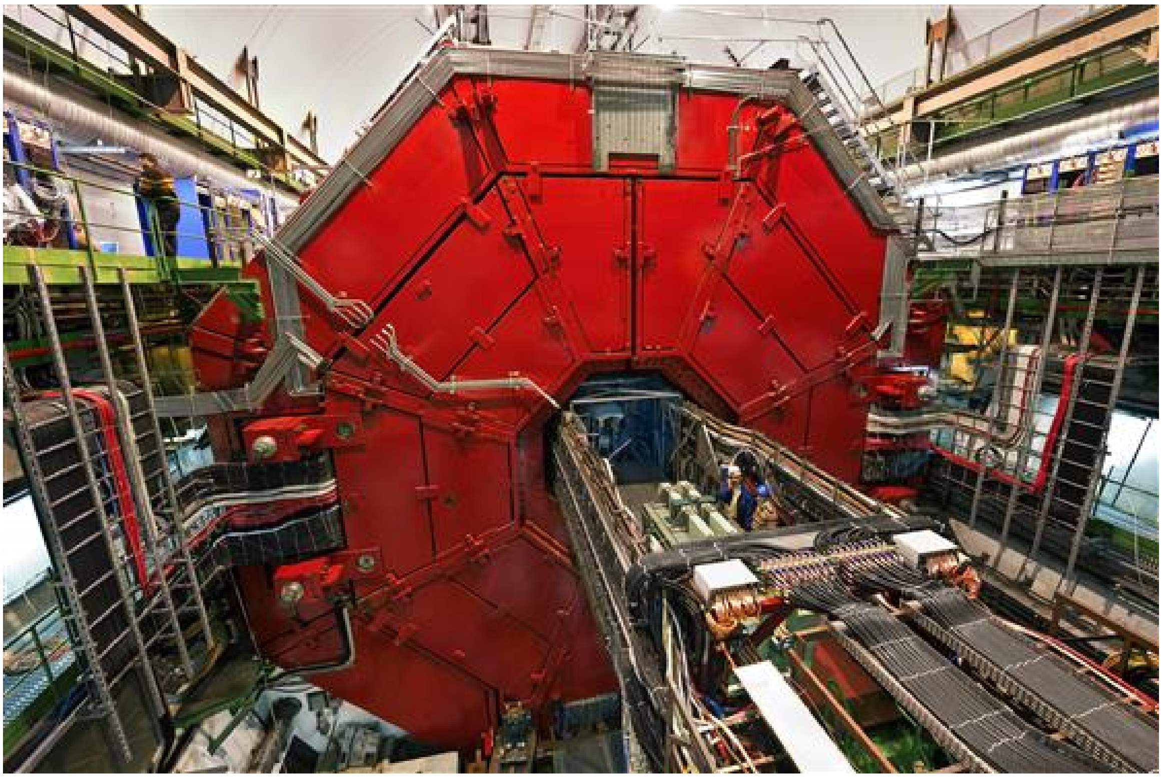

Figure 2.4. A general view from the ALICE detector.
(CERN provides the image free of charge for educational and informational use.)

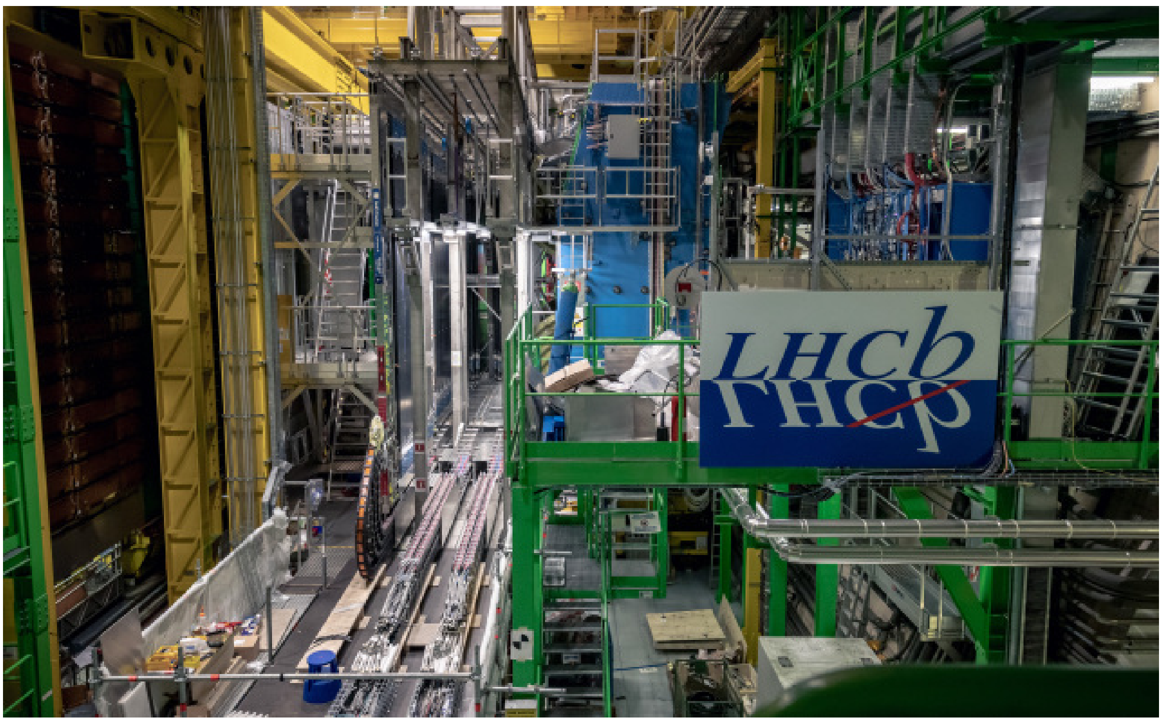

Figure 2.5. A general view from the LHCb detector.
(CERN provides the image free of charge for educational and informational use.)

The fourth detector, the CMS detector, will be discussed in the next chapter.

Some of the important design parameters for the LHC is listed in Table 2.1 below [11].

Table 2.1. Important design parameters for the LHC.

Design Parameter	**Value**
Circumference	26 659 m
Dipole operating temperature	1.9 K
Number of magnets	9593
Number of main dipoles	1232
Number of main quadrupoles	392
Number of RF cavities	8 per direction
Energy, protons	7 TeV
Energy, ions (per nucleon)	2.76 TeV/u
Peak magnetic dipole field	8.3 T
Distance between bunches	$\sim$7.5 m
Luminosity (protons)	10^{34} cm^{-2} s^{-1}
No. of bunches per proton beam	2808
No. of protons per bunch	1.15×10^{11}
Bunch separation for protons	25 ns
Number of turns per second	11 245
Number of collisions per second	1 billion
RMS beam radius at IP for proton beam	16.7 μm

3. THE COMPACT MUON SOLENOID (CMS)

The CMS detector is one of the four detectors on the LHC. The CMS detector, which can be seen in Figure 3.1 [12], has a giant solenoid magnet which generates a magnetic field of around 4 Tesla, about 100,000 times of Earth's magnetic field. The CMS detector has a weight of 14,000 tonnes. It is 21 meters long, 15 meters wide and 15 meters high.

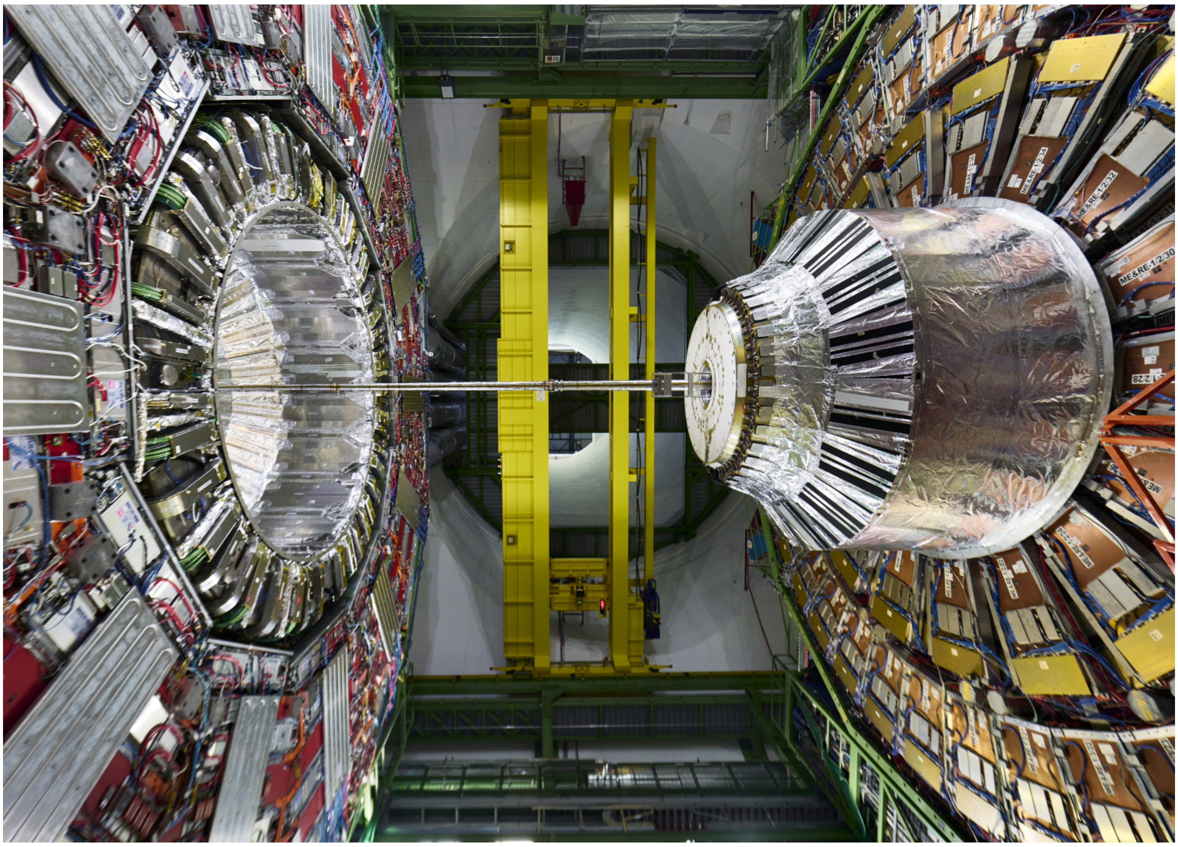

Figure 3.1. A general view of the CMS detector.

(CERN provides the image free of charge for educational and informational use.)

3.1. Structure

The structure of the CMS is similar to an onion in terms of having a lot of layers. A representation of layers of the CMS is given in Figure 3.2. In this figure, the scale could be understood by looking at the man drawn by black color.

The main parts of the CMS can be listed as Solenoid Magnet, Tracking System, Electromagnetic Calorimeter, Hadron Calorimeter and Muon System. A schmatic view of the CMS detector is in Figure 3.2 [13].

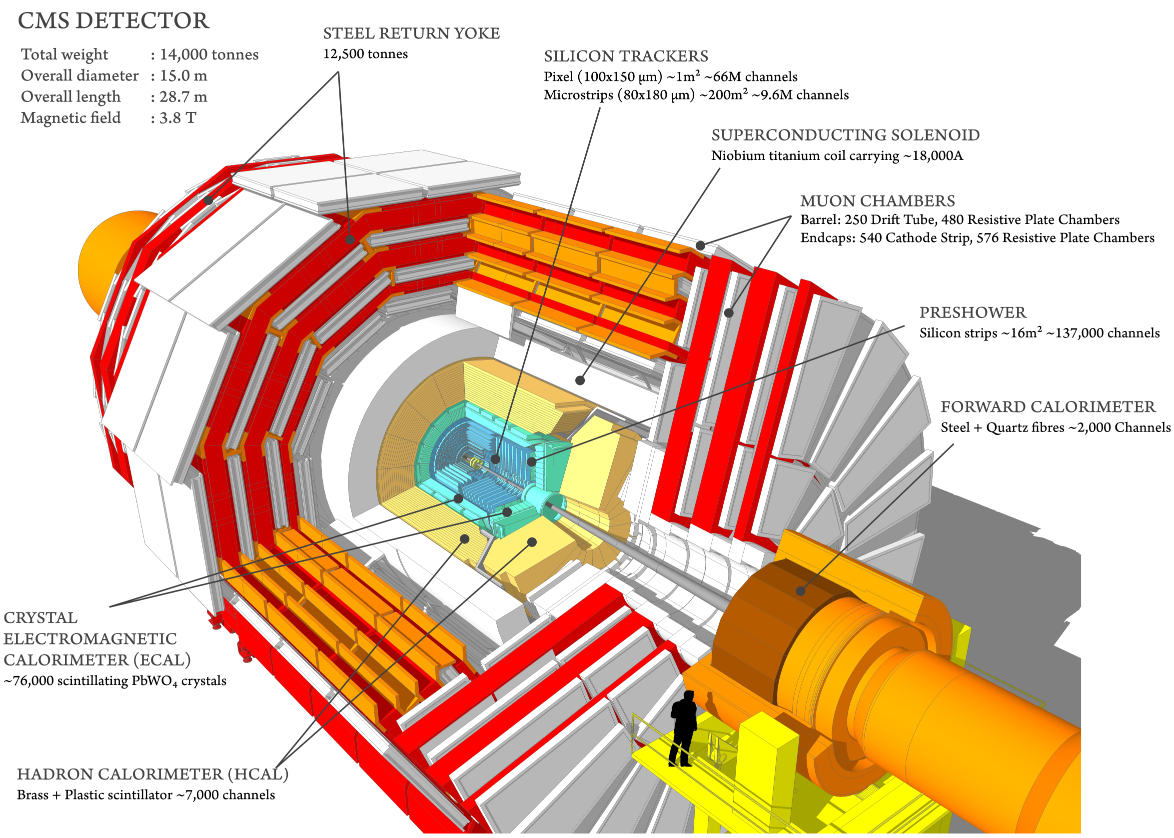

Figure 3.2. A schematic view of the CMS detector.

3.1.1. Solenoid Magnet

The force on a charged particle moving in a magnetic field is given as

$$\vec{\mathbf{F}}_B = q\vec{\mathbf{v}} \times \vec{\mathbf{B}} \tag{3.1}$$

where $\vec{\mathbf{B}}$ is the magnetic field, $\vec{\mathbf{v}}$ is the velocity of the particle and q is the charge of the particle. Therefore, the charge of a moving particle can be determined from the bending of the particle in a magnetic field.

The main purpose of the Solenoid Magnet is to bend particles which fly outwards from the collision point. Magnetic bending is important since it helps to determine the charge and momentum of the particles. A cross-sectional representation of how different particles interact with the CMS sub-detectors is in Figure 3.3 [14].

The solenoid magnet has a cylindrical coil formed by superconducting wires in which 18,500 Ampere current circulates. This generates a magnetic field of around 4 Tesla, which is 100,000 times of the Earth's magnetic field. The steel return yoke confines the generated magnetic field in the detector.

3.1.2. Tracking System

In order to track the trajectories of the particles bent by the magnetic field, a silicon tracker, which consists of 75 million individual electronic sensors is used. The particles interact with the silicon electromagnetically and leave a track of the path through which they move.

3.1.3. Electromagnetic Calorimeter (ECAL)

There are two types of calorimeters inside the CMS detector. The ECAL is the inner one. As its name suggests, it is used to measure the energies of non-hadronic electromagnetic particles, namely electrons, positrons and photons. The ECAL has nearly 80,000 lead tungstate crystals which scintillate when electrons, positrons and photons pass through them. The photons generated by scintillations generate electrons and positrons by pair production, and these new electrons and photons cause new scintillations. This phenomenon is called Electromagnetic (EM) shower and it continues until a certain energy threshold. The energy of the electrons, positrons and photons are deduced by the total energy of the corresponding EM shower.

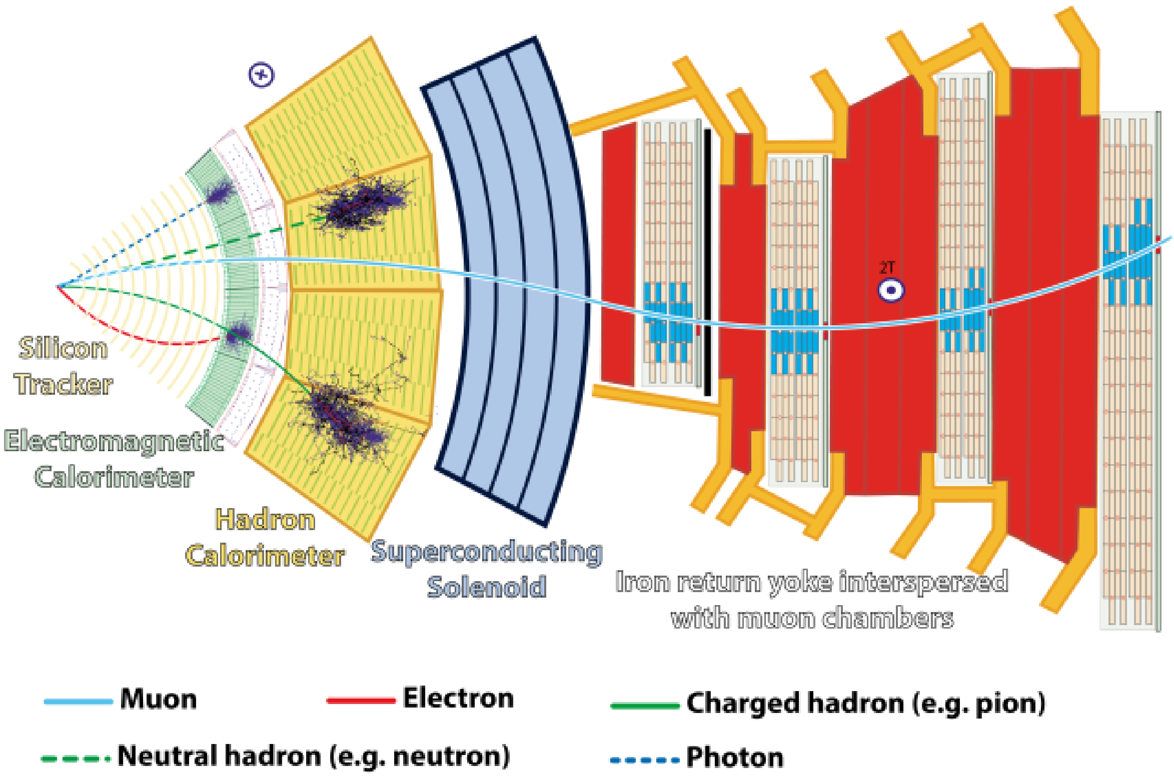

Figure 3.3. A representation of the cross-sectional slice of the CMS sub-detectors and how different particles interact with them.

3.1.4. Hadron Calorimeter (HCAL)

The other calorimeter in the CMS detector is the HCAL. The HCAL is used to measure the energy of hadrons, which are composite particles made of quarks and gluons. More details about the HCAL are given in Chapter 4.

3.1.5. Muon System

Muons do not interact much with any part of the CMS presented above. Therefore, a special muon system was designed only for the detection of muons. The muon system is located outside of the solenoid magnet. It is the outermost part of the CMS.

The muon system consists of three parts, which are the barrel drift tube chambers, the cathode strip chambers and the resistive plate chambers.

3.2. Geometry

The collision point is the origin point of the coordinate system of the CMS. Azimuthal angle ϕ and pseudorapidity η are used for referring to the different parts of sub-detectors. A visualisation of the geometry and the coordinate conventions of the CMS detector is in Figure 3.4 [15].

Azimuthal angle is the angle measured from x-axis on x-y plane, where z-axis is along the beam direction. The psuedorapidity is expressed as

$$\eta = -ln\left(\frac{tan\theta}{2}\right) \tag{3.2}$$

where θ is the angle between particle's three-momentum and the beam.

The pseudorapidity is highly-relativistic approximation of the rapidity, which is defined as

$$y \equiv \frac{1}{2}ln\left(\frac{E+p_z}{E-p_z}\right) \tag{3.3}$$

where p_z is the momentum along the z-axis and E is the total energy of the particle.

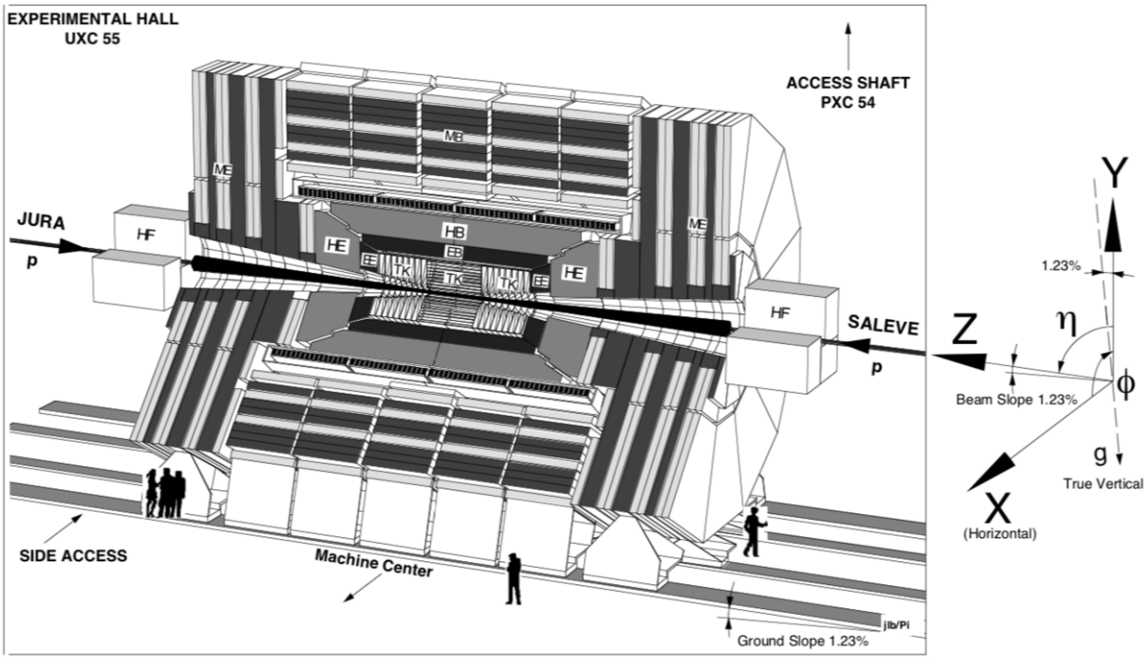

Figure 3.4. A representation of the coordinate conventions of the CMS. (CERN provides the image free of charge for educational and informational use.)

4. THE HADRON CALORIMETER

The HCAL measures the energy of hadronic particles such as protons and pions, which are made of quarks and gluons. The HCAL is a sampling calorimeter with four main sub-parts, namely the Hadron Barrel (HB), the Hadron Outer (HO), the Hadron Endcap (HE) and the Hadron Forward (HF), which positions are shown in Figure 4.1 [16]. The method of measuring the energy is by absorbing the particle with a dense absorber, producing showers in the process. The particles in the showers are detected and their energies are measured by various methods in these calorimeters. In the HF part, there are quartz fibers as active elements and the particles produce Cherenkov radiation in them.

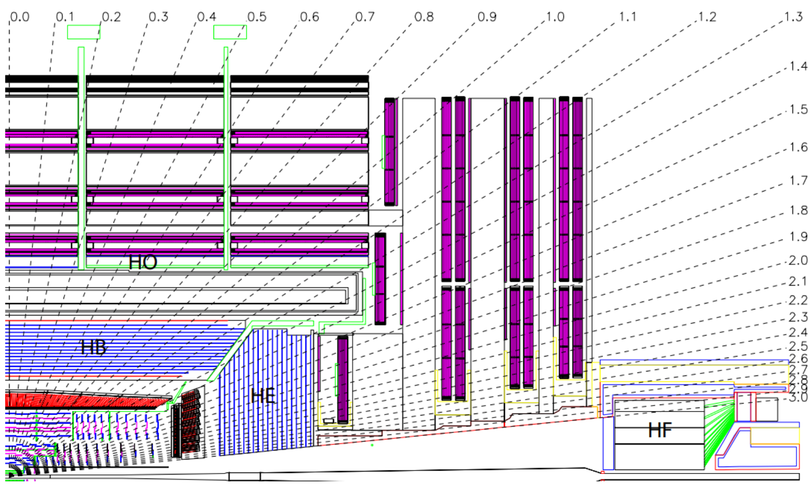

Figure 4.1. Drawing which shows the positions of HB, HO, HE and HF.

4.1. Hadron Barrel

The HB calorimeter, which is seen in Figure 4.2 [17], extends out to $|\eta| < 1.4$. It is an assembly of two half barrels, each of which has 18 identical wedges covering 20° in ϕ. These wedges consist of layers of flat brass alloy and scintillators of various widths. The top and the bottom layers have stainless steel instead of brass as absorber.

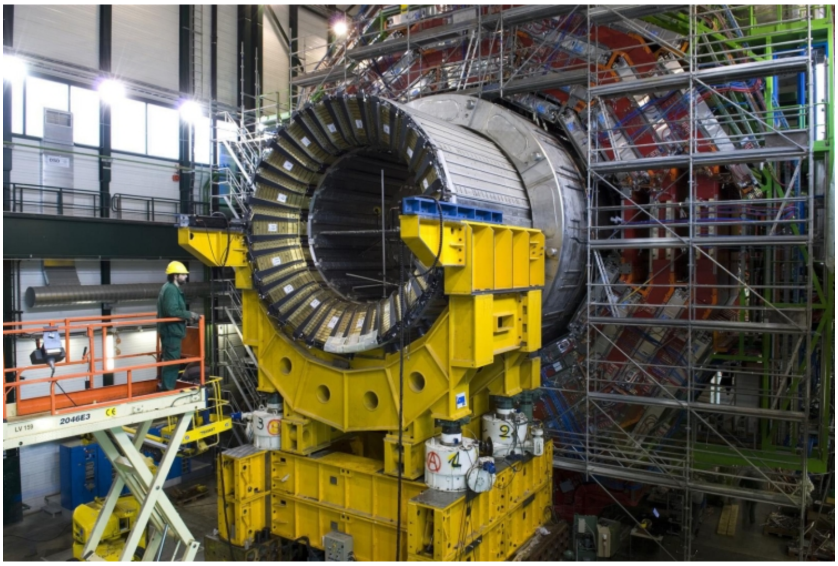

Figure 4.2. Hadron Barrel being inserted inside the solenoid magnet.
(CERN provides the image free of charge for educational and informational use.)

4.2. Hadron Outer

Outside the solenoid magnet, an additional layer of scintillators is placed, which is called the HO calorimeter. It is in the region of $|\eta| < 1.26$.

4.3. Hadron Endcap

The HE calorimeter is composed of brass and scintillators similar to the HB. It also has two parts on each side of the HB. The pseudorapidity range of $1.3 < |\eta| < 3.0$ is covered by the HE.

4.4. Hadron Forward

The Hadron Forward (HF) calorimeter is in the range of $2.9 < |\eta| < 5.2$. More details on the HF is given in Chapter 5.

5. THE HADRON FORWARD CALORIMETER

The HF calorimeter is the sub-part of the HCAL which is the nearest to the beam with its high pseudorapidity range ($2.9 < |\eta| < 5.2$). It is designed to detect high energy jets and particles. The HF has two modules called as HF+ and HF-. They are located 11.2 m away from the collision point at each end of the CMS detector.

5.1. Design and Structure

5.1.1. Absorber

The HF has a steel absorber as 18 wedges with 20° in ϕ. The steel absorber has 5 mm thick plates with about 1 mm grooves which are separated by 5.0±0.1 mm center-to-center. The radiation hard quartz fibers with two different lengths are alternately inserted in these grooves. The full depth of the absorber material is 165 cm. Half of the fibers run over this 165 cm full depth whereas half of them starts at 22 cm depth from the front side. This design makes it possible to distinguish between EM showers and hadronic showers since EM showers are absorbed mostly in the first 22 cm and therefore do not create a signal in short fibers [18].

The wedges of the HF have 24 towers as shown in Figure 5.1 [18]. All of the towers cover 10° except the two nearest to the beam, enumerated by 12 and 13 in Figure 5.1.

Towers cover certain η ranges as shown in Figure 5.1. For convenience, these ranges are indexed. These indices called "iEta"s and are given in Table 5.1 [18] with their η ranges and sizes. Notice that 10° approximately corresponds to 0.175 radians. Therefore, almost each tower has a size of $\Delta\eta \times \Delta\phi = 0.175 \times 0.175$.

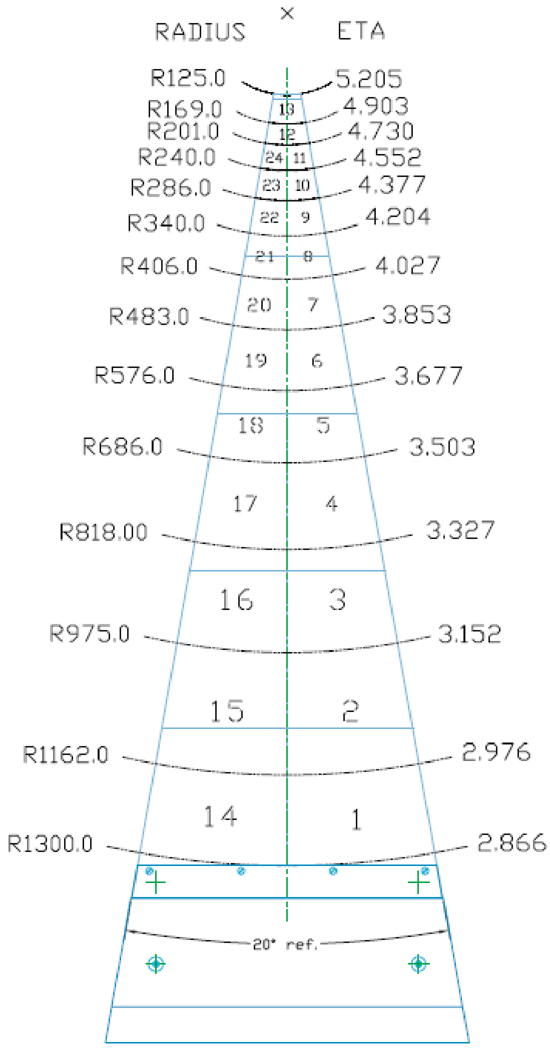

Figure 5.1. Representation of a wedge of the HF (towers are enumerated).

Azimuthal angle ϕ ranges are also indexed as iPhi similar to iEta for η. iPhi indices start at 1 and have increments of 2 for each 10°. Table 5.2 shows iPhi indices with corresponding ϕ ranges.

5.1.2. Cherenkov Radiation

Cherenkov radiation is the radiation emitted when a charged particle moves with a velocity greater than the speed of light in the medium (c/n), where c is the speed of light in vacuum and n is the refractive index of the medium. The signal in the HF is the Cherenkov radiation due to particle showers.

5.1.3. Photomultiplier Tubes

Photomultiplier tubes are used to convert the light into the signal in the HF. A PMT consists of a cathode, an anode and several dynodes, with potential difference between them. When the Cherenkov light falls on the cathode, it emits an electron. Emitted electron falls on the first dynode and takes off more electrons. The process continues and it generates multiple electrons. Thus, the weak signal gets amplified in the PMT. The PMTs used in the HF are four-anode PMTs. The anode is divided into four regions to distinguish between the signals produced by the stray pions and the Cherenkov light.

Table 5.1. List of iEta values with corresponding ranges and sizes.

iEta	η range		Size	
	Low	High	η	ϕ (degrees)
29	2.866	2.976	0.110	10
30	2.976	3.152	0.176	10
31	3.152	3.327	0.175	10
32	3.327	3.503	0.176	10
33	3.503	3.677	0.174	10
34	3.677	3.853	0.176	10
35	3.853	4.027	0.174	10
36	4.027	4.204	0.177	10
37	4.204	4.377	0.173	10
38	4.377	4.552	0.175	10
39	4.552	4.730	0.178	10
40	4.730	4.903	0.173	20
41	4.903	5.205	0.302	20

Table 5.2. List of iPhi values with corresponding ranges

iPhi	ϕ range (degrees)
1	0-10
3	10-20
5	20-30
7	30-40
...	...
...	...
65	320-330
67	330-340
69	340-350
71	350-360

6. THE ONLINE RADIATION DAMAGE MONITORING

6.1. Purpose

The HF calorimeter covers a high pseudorapidity range of precisely $2.9 < |\eta| < 5.2$. These high pseudorapidity values involve the particles with the highest energy which cause the emission of Cherenkov Radiation in the quartz fibers of the HF calorimeter. Due to the powerful radiation, the quartz fibers get damaged and the transparency of the quartz fibers decreases. For correct energy measurements, calibration must be corrected to compensate the increased light attenuation in the fibers. Therefore, the decrease in the transparency of the quartz fibers should be monitored continuously. The purpose of the HF Online Radiation Damage Monitoring System is to provide the correction to the calibration by monitoring the transparency of the quartz fibers due to the radiation damage.

6.2. HF Online Radiation Damage Monitoring System

The quartz fibers inserted in the absorber wedges were mentioned in Section 5.1.1. To construct HF Online Radiation Damage Monitoring System, four wedges were chosen from each HF. Selected wedges are shown in Figure 6.1 [1].

In these wedges, 7 iEta values were selected so that all the range is covered as much as possible. In each tower with selected iPhi and iEta values, the HF Online Radiation Damage Monitoring System fiber is implemented. Therefore, in total, 56 channels corresponding to 56 fibers are in the HF Online Radiation Damage Monitoring System.

The actual iEta and iPhi values of towers in which the HF Radiation Damage Monitoring System is implemented are given in Table 6.1. These fibers are often called as “channels” in the analysis. For example “Channel (30 1)” refers to the data from the fiber in the tower of iEta = 30 and iPhi = 1.

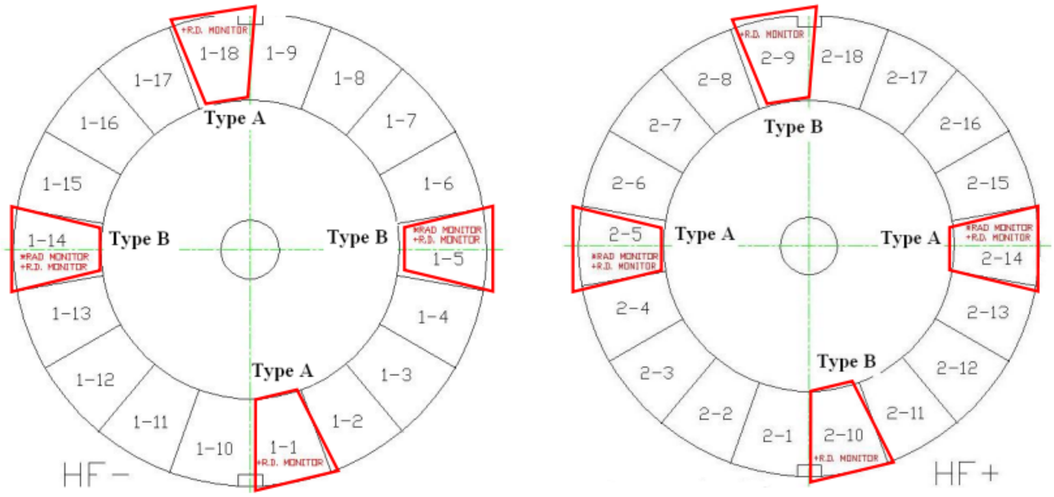

Figure 6.1. Selected wedges for the HF Online Radiation Damage Monitoring System. (© 2018 IEEE.)

Table 6.1. iEta and iPhi values of towers in which the HF Radiation Damage Monitoring System is implemented.

HF+		**HF-**	
iEta	**iPhi**	**iEta**	**iPhi**
30	1,21,37,57	-30	15,35,51,71
32	1,21,37,57	-32	15,35,51,71
34	1,21,37,57	-34	15,35,51,71
36	1,21,37,57	-36	15,35,51,71
38	1,21,37,57	-38	15,35,51,71
40	19,35,55,71	-40	15,35,51,71
41	19,35,55,71	-41	15,35,51,71

Notice that iPhi values for iEta 40&41 are different from the other selected HF+ towers. This might look like wrong as it was previously mentioned that 4 wedges selected for each HF. But notice that each wedge is 20° and covers two iPhi's, which are 10° each. In this manner, iPhi values 19&21, 35&37, 55&57 and 71&1, which are consecutive, are in the same wedge.

The system works as shown in Figure 6.2 [1]. A laser light is fired into the fiber. At the front end of the fiber there is a reflecting surface which reflects some portion of the light directly back towards the PMT, without entering the fiber, therefore without any attenuation in the fiber. The signal produced by this light pulse is called S1. The rest of the laser beam goes into the fiber and is reflected from the end of the fiber to the PMT. The signal produced by this light pulse is called S2. The time it takes for the laser beam to travel to the end of the fiber and reflect back to the front end of the fiber is 25 ns. Therefore there is a 25 ns delay between S2 and S1.

The laser in the HF Online Radiation Damage Monitoring System has a wavelength of 450 nm because the PMTs in the HF are most sensitive to the light having wavelength between 400-500 nm.

It might seem like it is important to divide the laser to exactly half for S1 and S2 but the division is irrelevant unless one of them is too low. Because the analysis method is not based on the actual ratio of S2/S1. Rather, the analysis method is based on the relative S2/S1 ratio. S2/S1 ratio for each run is normalized by S2/S1 of the first run in the analysis. More details will be given in Chapter 7.

6.3. Radiation Damage Recovery

When the collisions stop, certain amount of recovery is observed in the radiation damage of the fibers. This recovery effect is clearly observed in the graphs at Chapter 7.9. Around 450 nm, which is the wavelength of the laser used in the HF Radiation Damage Monitoring System, the recovery is the highest [19].

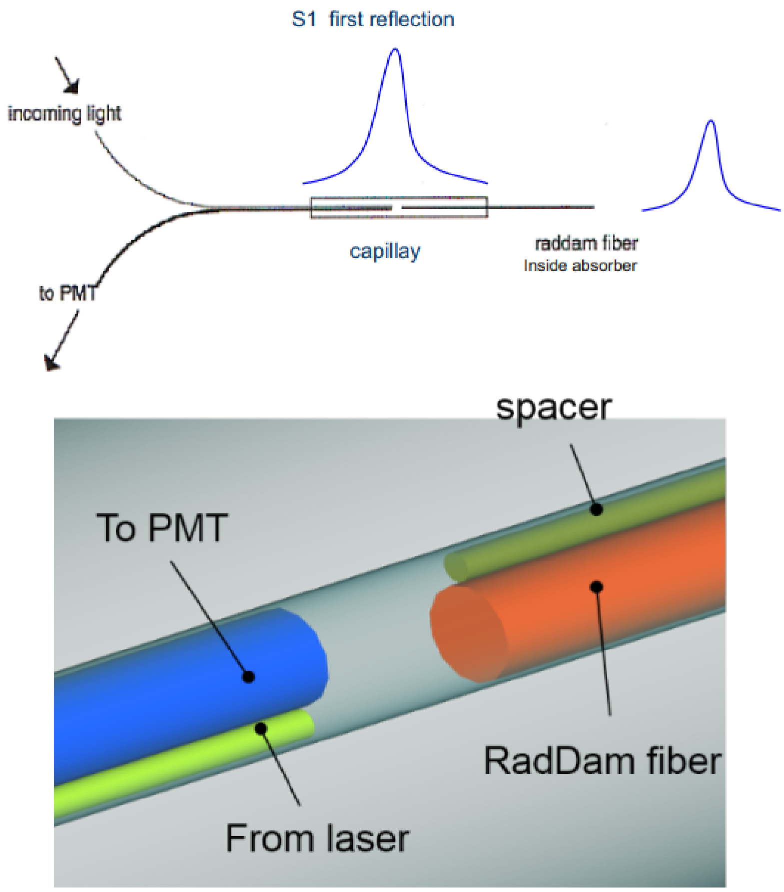

Figure 6.2. Sketch which describes the principle of operation for the HF Online Radiation Damage Monitoring System.

7. ANALYSIS

7.1. ROOT and LXPLUS (Linux Public Login User Service)

The analysis was done using ROOT, which is an open-source data analysis framework created at CERN. [20] ROOT is written in C++ and commonly used by high energy physicists.

Linux Public Login User Service (LXPLUS) is logon service to Linux for CERN users. Using LXPLUS, the code used in this analysis was run on computers running Linux at CERN. The access to LXPLUS is by using SSH (Secure Shell Protocol).

7.2. Delay Time Settings

To determine delay times for each 56 channel, "$\frac{Q_1+Q_2}{Q_t}$ versus Events" graphs are used. For ideal case, $Q_1 + Q_2$ should be equal to Q_t, which is total Q. This implies that the events with the ratio of $\frac{Q_1+Q_2}{Q_t}$ as near as possible to 1 should be selected.

Figure 7.1 shows the $\frac{Q_1+Q_2}{Q_t}$ versus Events graph for channel (30 21) for run 355886. The set of events with the nearest $\frac{Q_1+Q_2}{Q_t}$ ratio to 1 is the events between 0 and 5000. The delay time of this set of events is labeled as set 0.

But getting proper graphs to be able to select a region with $\frac{Q_1+Q_2}{Q_t}$ almost equal to 1 is not trivial. QIE phase scans are done by taking data over the full range of laser time delay. These different timing delays resulted in different $\frac{Q_1+Q_2}{Q_t}$ graphs, some of which have sets with ratio approaching to 1, some have not. As an example, a graph with a bad timing delay is shown in Figure 7.2. In this case, none of the sets can be selected for the analysis.

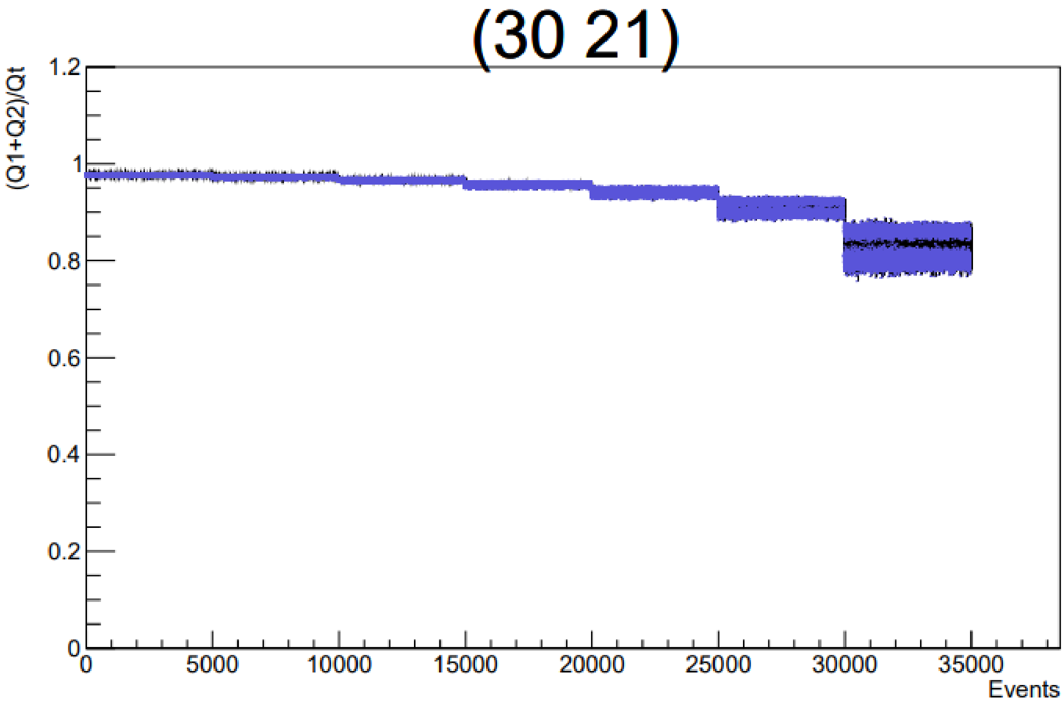

Figure 7.1. Graph of $\frac{Q_1+Q_2}{Q_t}$ versus Events for channel (30 21) for run 35588.

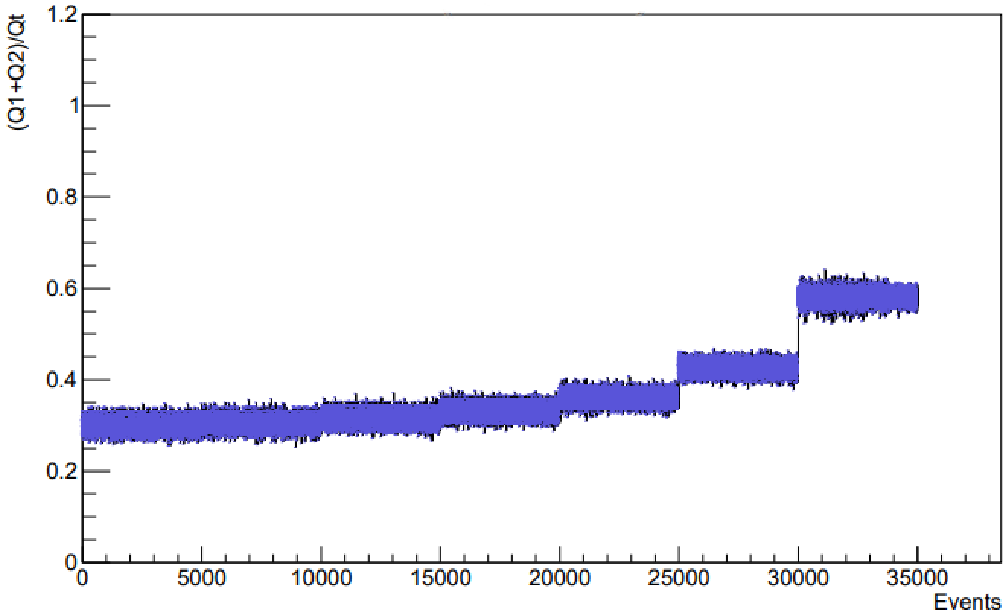

Figure 7.2. An example of a bad raddam laser timing delay for a graph of $\frac{Q_1+Q_2}{Q_t}$ versus events.

7.3. Pulse Shape Histograms

After selecting the ideal delay time set for a channel, pulse shape of the channel fits nicely in two time slots as in Figure 7.3. The first one of these slots (i.e. slot labeled as 3) is S1, the signal from the light directly coming to PMT. The other slot (i.e. slot labeled as 4) is S2, the signal from the light reflected back from the end of the fiber.

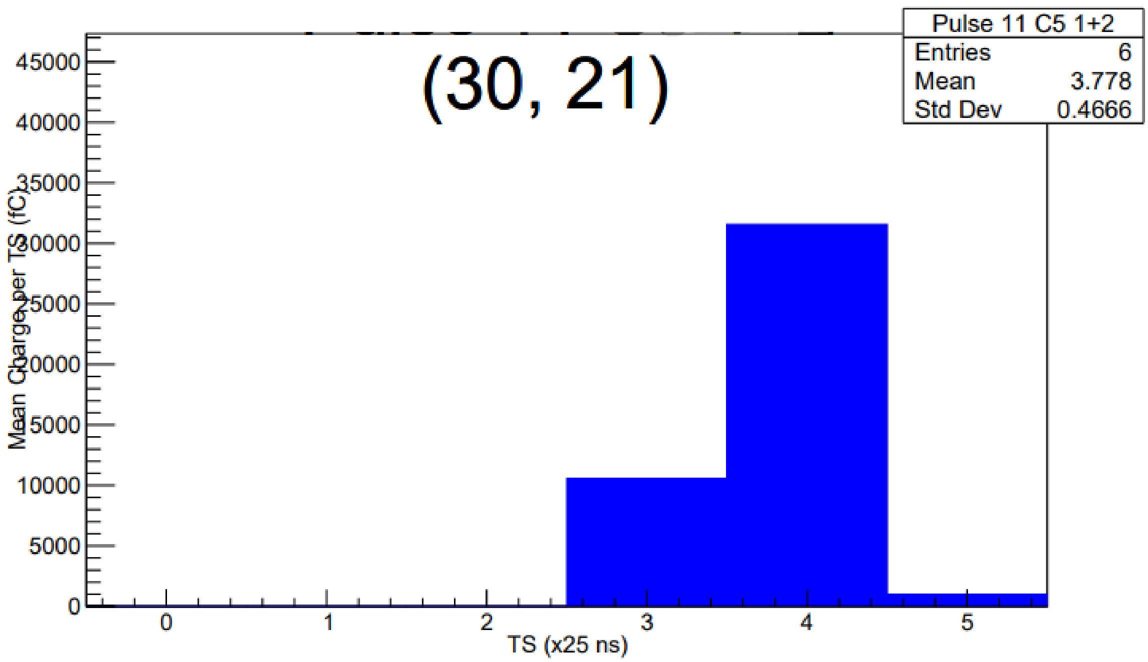

Figure 7.3. Pulse shape histogram: Mean Charge per TS (fC) versus TS (x25ns) for channel (30 21) for run 355886.

In Section 6.2, it was mentioned that the delay between S2 and S1 is 25 ns. Correspondingly, notice that each slot in Figure 7.3 is exactly 25 ns.

If the delay time set is not selected appropriately, the pulse shape would be seen as spread in three slots instead of two slots. For example, Figure 7.4 shows the pulse shape if the set of events between 30000-35000 which is labeled as set 6 is chosen instead of set 0.

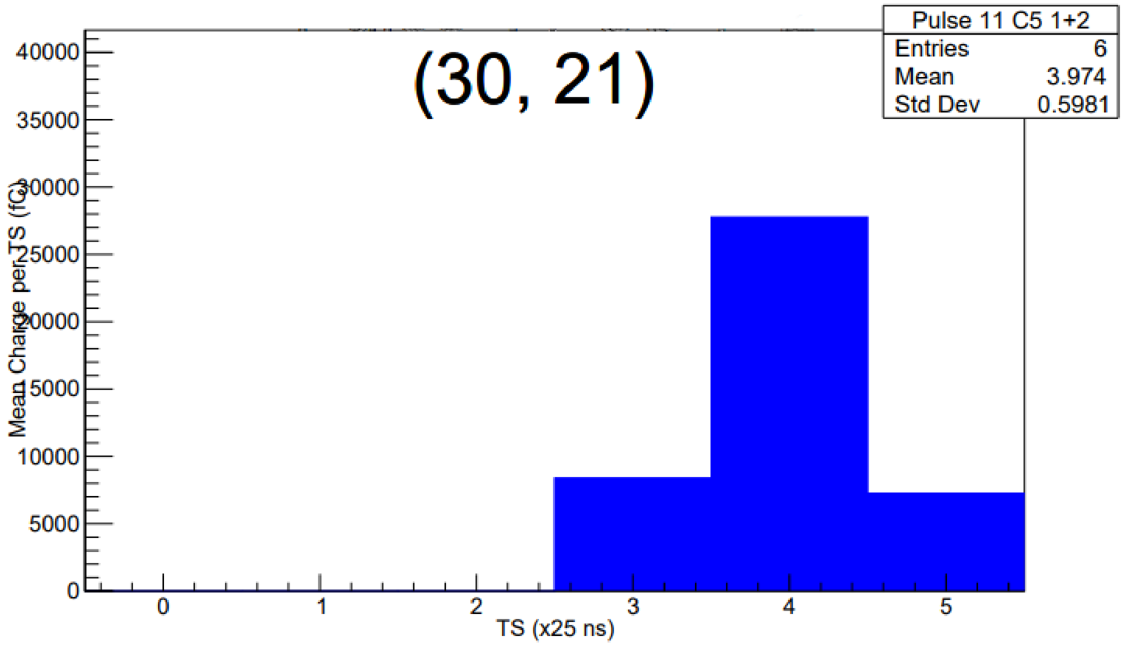

Figure 7.4. Pulse shape histogram for channel (30 21) for run 355886 if set 6 is wrongly chosen instead of set 0.

7.4. Pedestals

Pedestals are calculated as the arithmetic average of the charges in slots 1 and 2 of Figure 7.3. The calculated pedestal value is subtracted from the charges in slot 4 and slot 3. The results of subtractions are called Q2 and Q1, respectively.

7.5. Cuts

TDC cuts and charge cuts are applied to the data. With these cuts, certain events are ignored to improve the quality of the analysis.

7.5.1. TDC Cuts

Signals from two anodes are combined together to give two signals from the four anodes in the PMTs. Hence each PMT has two channels. TDC values of two channels of a PMT are expected to be close. To check this, TDC values of two channels are plotted. As seen in Figure 7.5, there are some events (data points) which are low in one channel and high in the other. These events must be ignored. By applying TDC cuts on these plots, only events which lie around the diagonal and the peak are kept as seen in Figure 7.6.

7.5.2. Charge Cuts

A charge cut is applied where either Q1 or Q2 is under 10fC. Events with under 10fC for Q1 or Q2 are ignored.

7.6. Charge Histograms

Charge histograms were drawn for Q1 and Q2, which are the charges due to the signal directly coming to PMT and the signal reflected back from the end of the fiber, after subtracting pedestals.

Charge histograms are used to check if anything goes wrong. Entries should not be too much lower than 5000, the number of events taken into account by choosing one set. Moreover, the histograms are expected to have a nice bell shape feature. If, for example, there is a mistake in TDC cuts, it is possible that a big portion of the events is cut and thus the entry value is too low and the bell shape feature is not observed.

7.7. Q2/Q1 Histograms

$\frac{Q2}{Q1}$ histograms are also drawn. After drawing the histograms, Gaussian fits are performed on the histograms. By doing this, mean and sigma values of the Gaussian fit are obtained. At this point, the mean values of $\frac{Q2}{Q1}$ for each channel of each run are obtained with related uncertainty values.

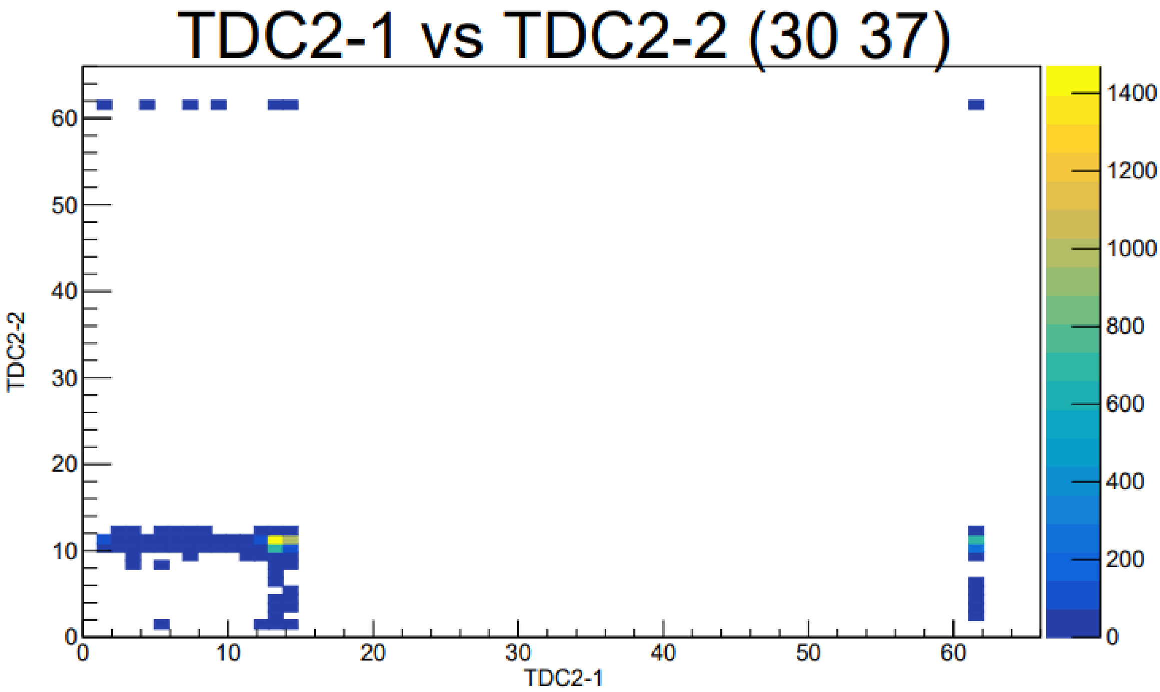

Figure 7.5. Graph of TDC2-1 versus TDC2-2 for channel (30 37) for run 355886 before applying TDC Cuts.

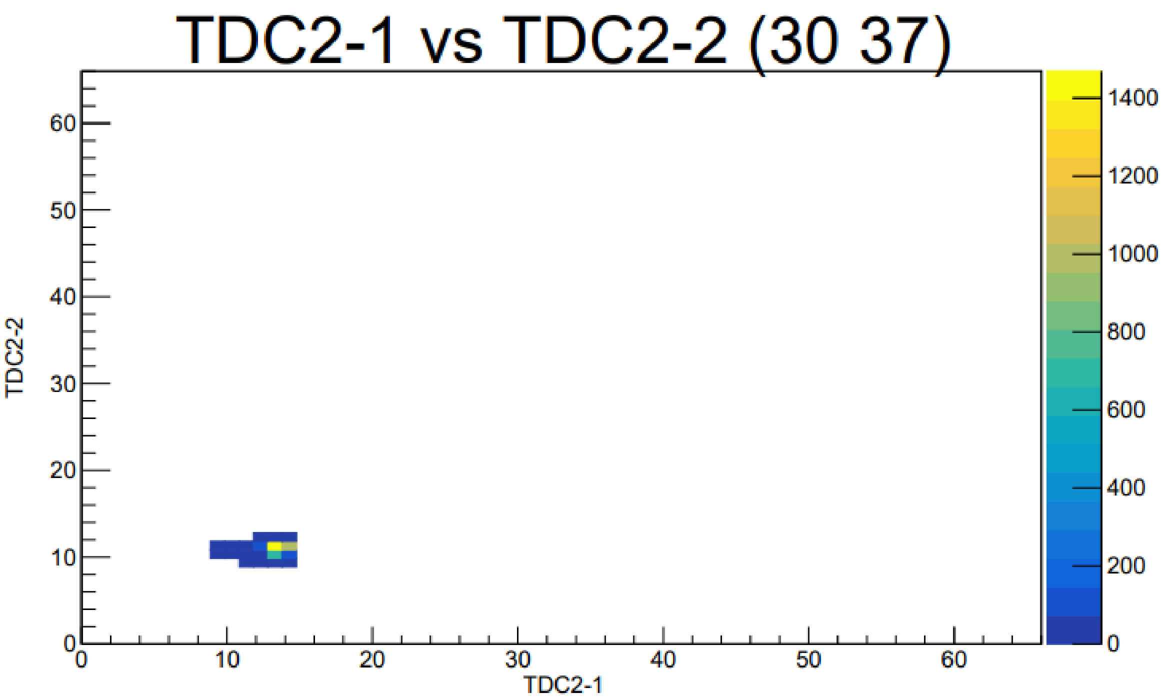

Figure 7.6. Graph of TDC2-1 versus TDC2-2 for channel (30 37) for run 355886 after applying TDC Cuts.

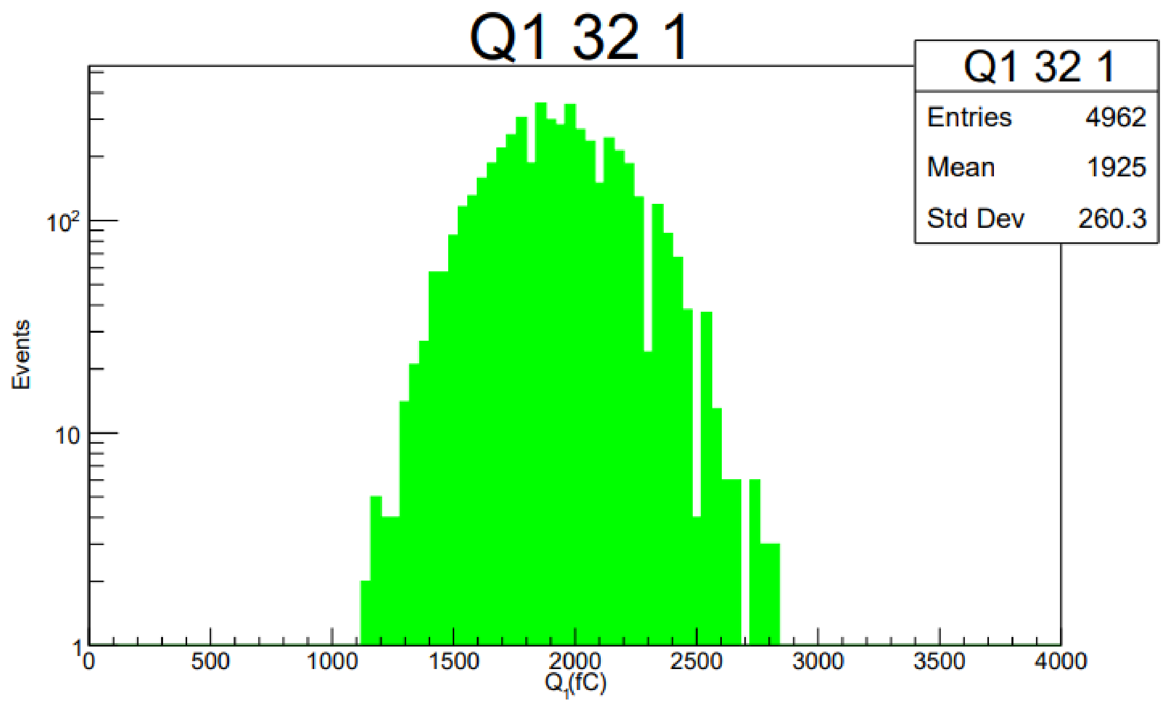

Figure 7.7. Q1 histogram for channel (32 1) for run 355886.

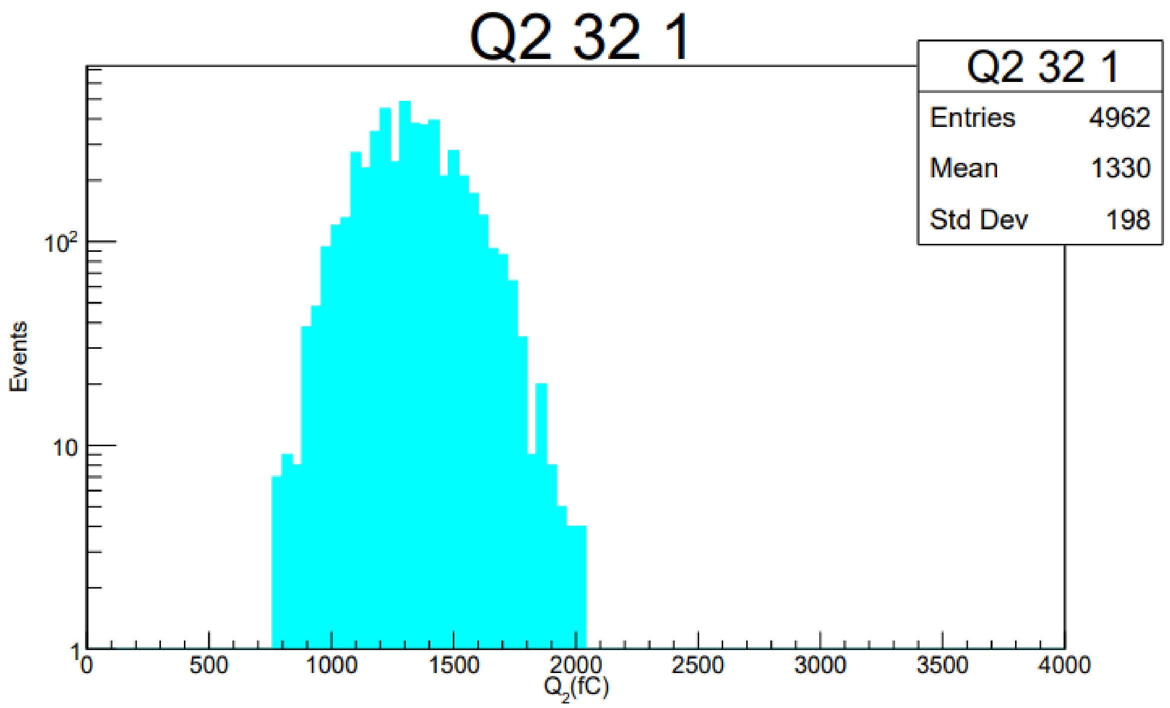

Figure 7.8. Q2 histogram for channel (32 1) for run 355886.

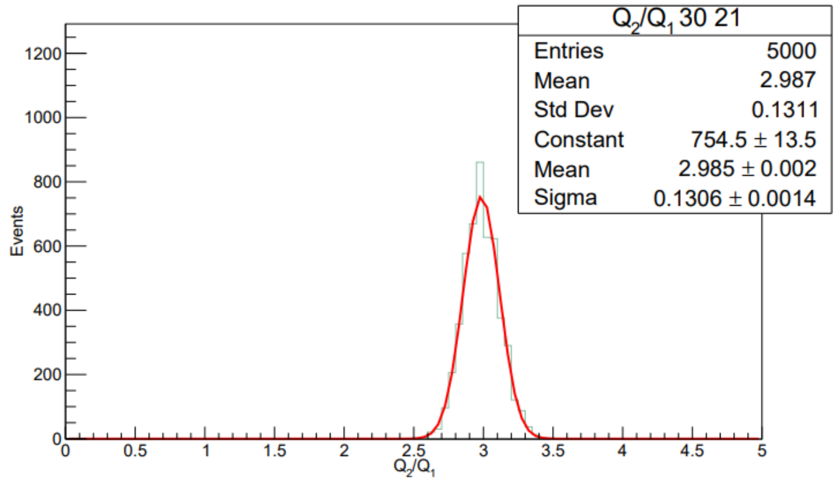

Figure 7.9. $\frac{Q2}{Q1}$ histogram for channel (30 21) for run 355886 after applying TDC Cuts.

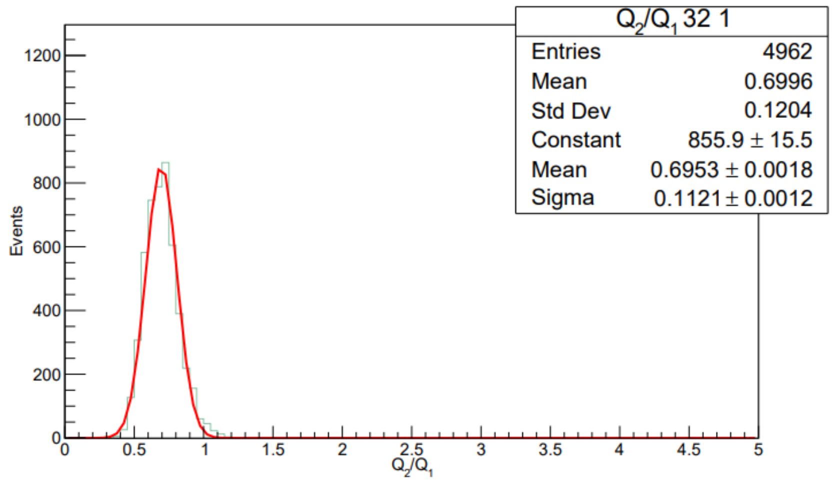

Figure 7.10. $\frac{Q2}{Q1}$ histogram for channel (32 1) for run 355886 after applying TDC Cuts.

7.8. Normalized Ratio Plots

Using the mean and uncertainty values from the Gaussian fits of $\frac{Q2}{Q1}$ histograms and combining the data for all runs in a plot, normalized ratio plots were drawn for each channel. The $\frac{Q2}{Q1}$ for a run is first normalized by dividing it to $\frac{Q2_0}{Q1_0}$, which is $\frac{Q2}{Q1}$ ratio of the first run in the list. Then, the square root of the normalized ratio $\frac{\frac{Q2}{Q1}}{\frac{Q2_0}{Q1_0}}$ was calculated. The square root is necessary here because the reflected laser beam travels the fiber twice, therefore the attenuation factor is applied twice or the total attenuation factor is the square of the attenuation factor.

For each channel, the square root of the normalized ratios are plotted against "Days", which represents the number of days since the first run in the list. Additionally, the same data are plotted against the integrated luminosity. (Section 7.9.2) And finally, these two type plots are averaged over iPhi for each iEta. (Section 7.9.3)

As an another step, each plus iEta is normalized by iEta = 30 and each minus iEta is normalized by iEta = -30. These are called doubly normalized ratio plots. These were necessary for comparison with collision data.

7.9. 2022 Results

7.9.1. Run List and Delay Time Settings

In total, 86 runs were analysed from year 2022. Table 7.1 gives a list of these 86 runs with their date. For all channels of the 2022 runs, appropriate delay time setting was 0, as in Figure 7.1.

Table 7.1. 2022 run list with corresponding dates.

	Run Number	**Date**	**Int. Lumi.(1/fb)**
1	355886	20/07/22	0.257
2	355952 *	21/07/22	0.269
3	356020	22/07/22	0.342
4	356214	26/07/22	0.506
5	356258	27/07/22	0.529
6	356340	28/07/22	0.713
7	356421	29/07/22	0.998
8	356459	30/07/22	1.278
9	356540	01/08/22	1.688

Table 7.1. 2022 run list with corresponding dates. (cont.)

	Run Number	**Date**	**Int. Lumi.(1/fb)**
10	356595 *	02/08/22	2.07
11	356837	05/08/22	2.916
12	356930	06/08/22	3.232
13	356960 *	07/08/22	3.670
14	357010 *	08/08/22	3.789
15	357146	10/08/22	4.792
16	357289	11/08/22	5.237
17	357340	12/08/22	5.623
18	357416	13/08/22	6.053
19	357457	14/08/22	6.185
20	357505	15/08/22	6.673
21	357567	16/08/22	6.673
22	357626	17/08/22	7.033
23	357647	18/08/22	7.033
24	357746 *	20/08/22	8.264
25	357789 *	21/08/22	9.023
26	357837	22/08/22	9.484
27	357848	22/08/22	9.484
28	357972	23/08/22	9.988
29	358000	24/08/22	9.998
30	359027	20/09/22	9.998
31	359097	21/09/22	9.998
32	359170	22/09/22	9.998
33	359237	23/09/22	9.998
34	359301	26/09/22	9.991
35	359383	27/09/22	9.991
36	359501	28/09/22	9.991
37	359555	29/09/22	10.005

Table 7.1. 2022 run list with corresponding dates. (cont.)

	Run Number	**Date**	**Int. Lumi.(1/fb)**
38	359657	30/09/22	10.106
39	359708	02/10/22	11.304
40	359736	03/10/22	11.718
41	359788	04/10/22	12.265
42	359828	05/10/22	12.703
43	359914	06/10/22	12.712
44	359968	07/10/22	13.121
45	360011	08/10/22	13.783
46	360044	09/10/22	13.991
47	360104 *	10/10/22	14.900
48	360150 *	11/10/22	15.305
49	360247	12/10/22	15.529
50	360313	13/10/22	16.187
51	360366	14/10/22	16.427
52	360471 *	16/10/22	17.840
53	360771	19/10/22	18.052
54	360807 *	20/10/22	19.132
55	360848	21/10/22	19.239
56	360905 *	22/10/22	20.222
57	360935 *	23/10/22	21.331
58	360958	24/10/22	21.598
59	361070 *	25/10/22	22.290
60	361161	26/10/22	22.873
61	361210 *	27/10/22	23.819
62	361254 *	28/10/22	24.752
63	361310 *	29/10/22	25.703

Table 7.1. 2022 run list with corresponding dates. (cont.)

	Run Number	**Date**	**Int. Lumi.(1/fb)**
64	361327	30/10/22	26.196
65	361374 *	31/10/22	26.746
66	361428 *	01/11/22	27.735
67	361455 *	02/11/22	28.852
68	361481 *	03/11/22	29.551
69	361522	04/11/22	30.052
70	361587 *	05/11/22	30.770
71	361613	06/11/22	30.770
72	361666	07/11/22	30.770
73	361763	08/11/22	30.770
74	361836	09/11/22	30.770
75	361967	12/11/22	31.673
76	361981	13/11/22	32.270
77	362116 *	16/11/22	34.674
78	362203	17/11/22	35.161
79	362270	18/11/22	35.161
80	362343	19/11/22	35.161
81	362395	20/11/22	35.161
82	362424	21/11/22	35.849
83	362481	22/11/22	35.849
84	362547	23/11/22	35.918
85	362637	24/11/22	36.424
86	362666 *	25/11/22	36.765

Among these 86 runs, 23 of them which took place in less than 1 hour after the nearest collision are selected to analyse separately. These 23 runs are indicated with * in the table.

7.9.2. Normalized Ratio Plots

The normalized ratio plots against days and against integrated luminosity are given below for channel with iEta = 32 and iPhi = 21. The steps of analysis method for generating these plots is described above. Plots of all chanells are given in Appendix A and Appendix B.

7.9.3. Normalized Ratio Plots Averaged On iPhi

The normalized ratio plots against days and against integrated luminosity are given below for iEta = 32 averaged over iPhi in Figure 7.13 and Figure 7.14. Plots of all iEta values are given in Appendix C.

As stated in 7.9.1, 23 runs which took place in less than 1 hour after the nearest collision are selected and they are analysed separately. For these 23 runs, the normalized ratio plots against days and against integrated luminosity are given below for iEta = 32 averaged over iPhi in Figure 7.15 and Figure 7.16. Plots of all iEta values are given in Appendix D. The plots drawn with respect to the integrated luminosity are also fitted quadrically, where p2 is the coefficient of the quadratic term, p1 is the coefficient of the linear term and p0 is the constant term.

A list of the coefficients of the quadratic fit to the data is given in Table 7.2, where it can be seen that the quadratic term is very small and even smaller than its error for many iEta values.

Since the quadratic term is very small and even smaller than its error value for many iEta values, imposing a linear fit seems reasonable. The linear fit is given below for iEta = 32, where p1 is the coefficient of the linear term and p0 is the constant term. Plots with linear fits for all other iEta values are at the end of the Appendix D. A list of the coefficients of linear and the constant terms is given in Table 7.3.

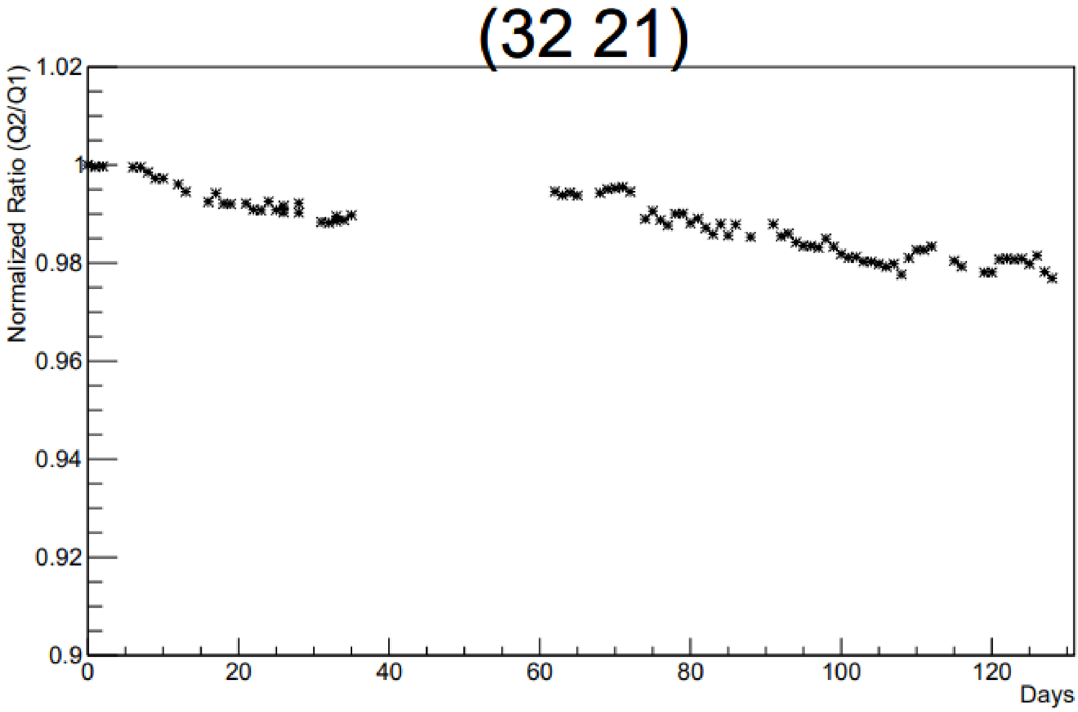

Figure 7.11. Graph of normalized ratio with respect to time for channel (32 21)

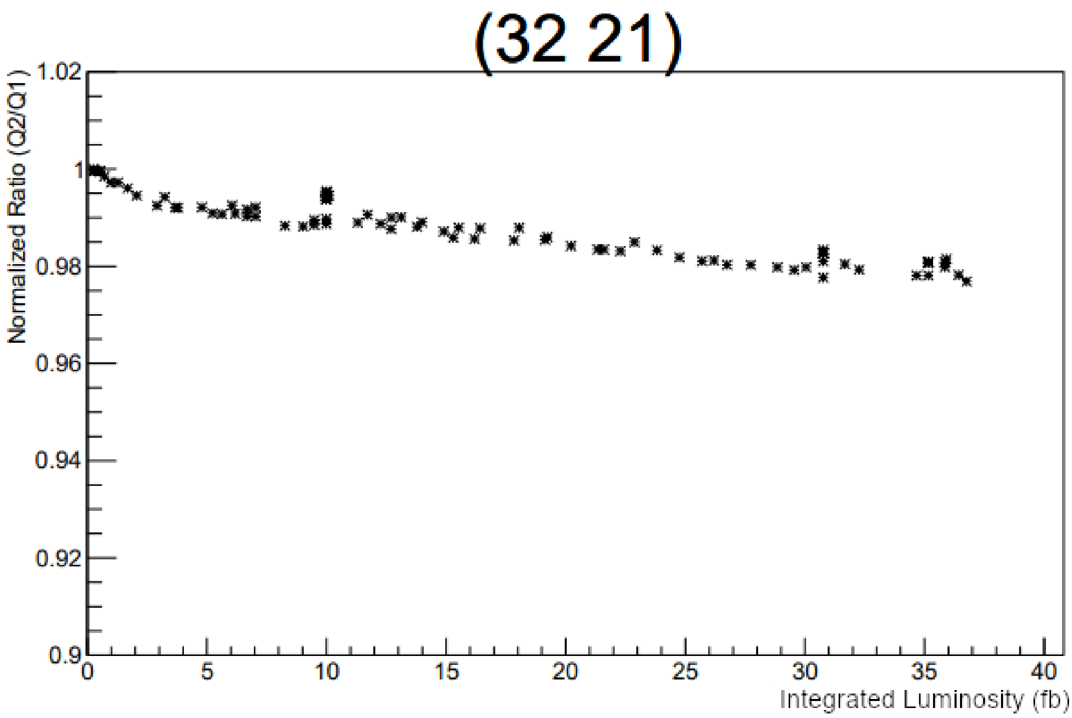

Figure 7.12. Graph of normalized ratio with respect to the integrated luminosity for channel (32 21)

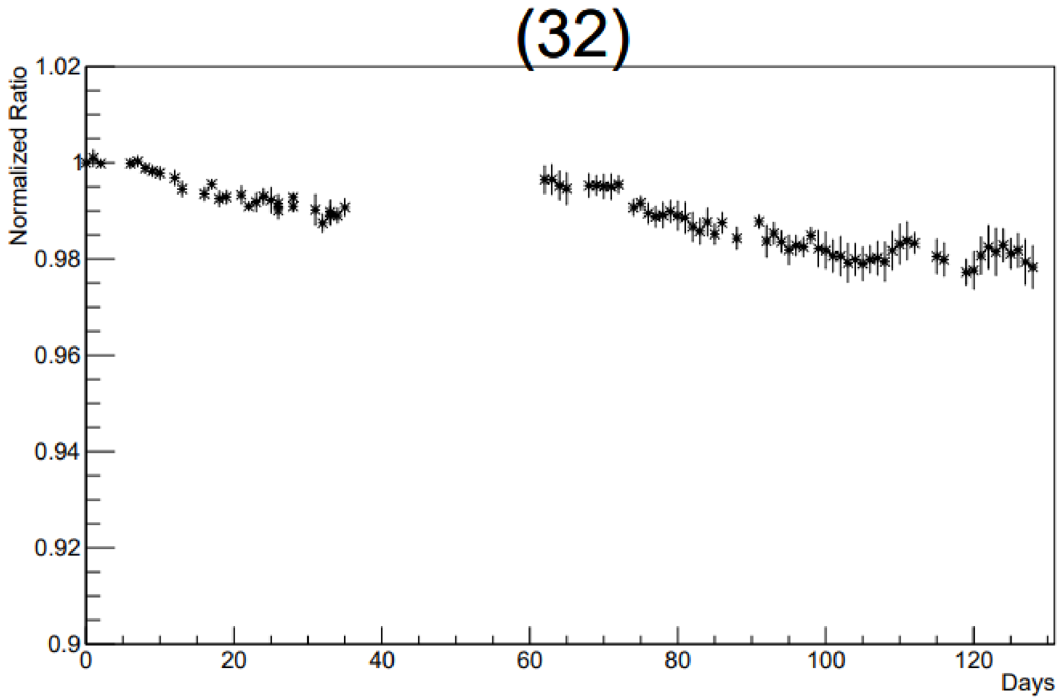

Figure 7.13. Graph of normalized ratio with respect to time averaged over iPhi for iEta 32.

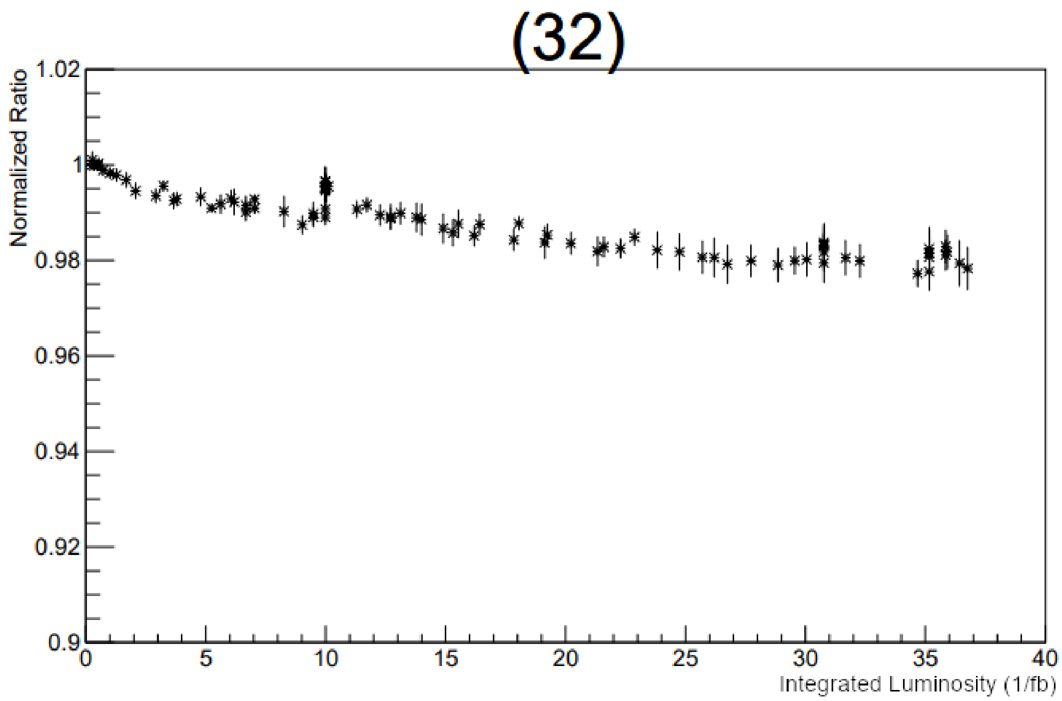

Figure 7.14. Graph of normalized ratio with respect to the integrated luminosity averaged over iPhi for iEta 32.

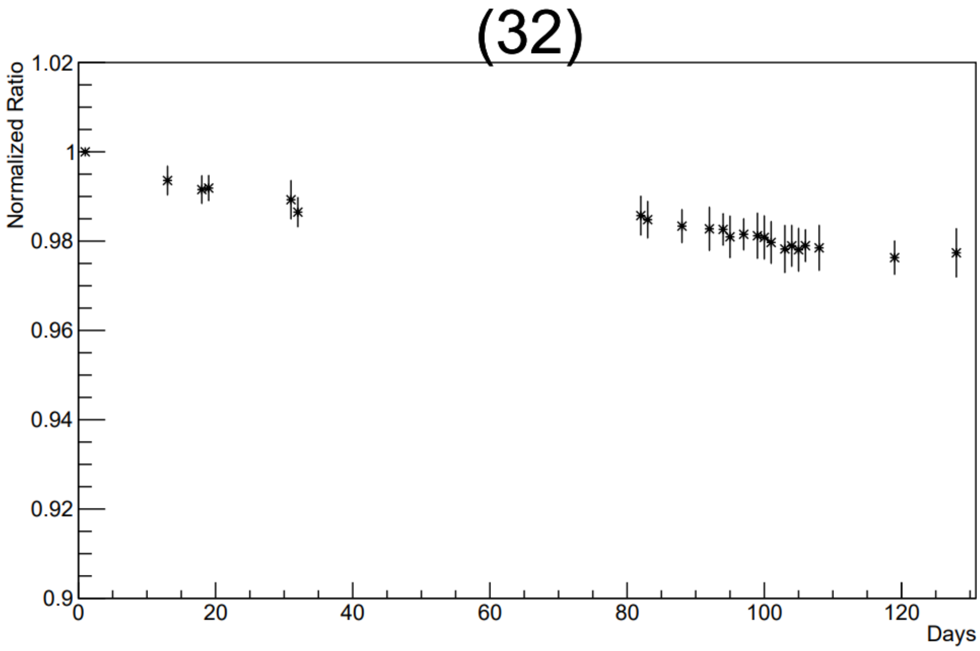

Figure 7.15. Graph of normalized ratio with respect to time averaged over iPhi for iEta 32 for the runs which took place in less than 1 hour after the nearest collision.

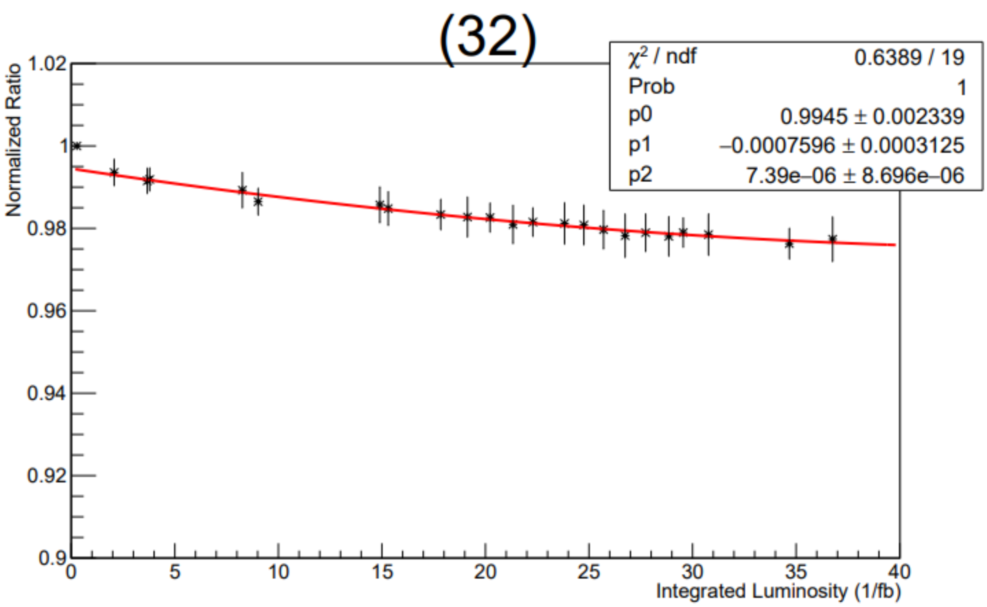

Figure 7.16. Graph of normalized ratio with respect to the integrated luminosity averaged over iPhi for iEta 32 for the runs which took place in less than 1 hour after the nearest collision (with quadratic fit).

Table 7.2. The list of the coefficients of quadratic terms (p2), linear terms (p1) and constant terms (p0) of all iEta values obtained from the quadratic fits of normalized ratio graphs with respect to the integrated luminosity averaged over iPhi for the runs which took place in less than 1 hour after the nearest collision.

iEta	**p2**	**p1**	**p0**
30	1.015e-07 ± 2.384e-06	-0.0002846 ± 9.735e-05	0.9973 ± 0.0009257
-30	4.073e-06 ± 3.648e-06	-0.0004423 ± 0.0001254	0.9982 ± 0.0007482
32	7.39e-06 ± 8.696e-06	-0.0007596 ± 0.0003125	0.9945 ± 0.002339
-32	7.351e-06 ± 6.122e-06	-0.0008041 ± 0.0001996	0.996 ± 0.001247
34	1.279e-05 ± 6.294e-06	-0.001184 ± 0.0002385	0.9894 ± 0.002023
-34	8.533e-06 ± 9.67e-06	-0.001089 ± 0.0002968	0.9887 ± 0.001669
36	1.645e-05 ± 6.261e-06	-0.001526 ± 0.0002143	0.982 ± 0.001595
-36	1.689e-05 ± 8.833e-06	-0.001518 ± 0.0003104	0.9827 ± 0.002256
38	1.789e-05 ± 6.058e-06	-0.001598 ± 0.0002206	0.9736 ± 0.001717
-38	1.052e-05 ± 9.879e-06	-0.001449 ± 0.0003547	0.9755 ± 0.002477
40	1.187e-05 ± 5.448e-06	-0.00139 ± 0.0002163	0.9693 ± 0.001876
-40	1.834e-05 ± 3.57e-06	-0.001647 ± 0.00009985	0.9732 ± 0.0005051
41	3.22e-07 ± 1.479e-05	-0.0007186 ± 0.000533	0.9701 ± 0.00416
-41	1.035e-05 ± 7.736e-06	-0.001044 ± 0.0002302	0.971 ± 0.0009595

7.9.4. Doubly Normalized Ratio Plots Averaged Over iPhi

The doubly normalized ratio plots against days and against integrated luminosity are given below for iEta = 32 averaged over iPhi. Plots of all iEta values are given in Appendix E.

For the 23 runs mentioned above, the doubly normalized ratio plots against days and against integrated luminosity are given below for iEta = 32 averaged over iPhi. Plots of all iEta values are given in Appendix F. The plot drawn with respect to the integrated luminosity are also fitted quadratically, where p2 is the coefficient of the quadratic term, p1 is the coefficient of the linear term and p0 is the constant term.

A list of the coefficients of the quadratic fit to the data is given in Table 7.4, where it can be seen that the quadratic term is very small and even smaller than its error for many iEta values.

Since the quadratic term is very small and even smaller than its error value for many iEta values, imposing a linear fit seems reasonable. The linear fit is given below for iEta = 32, where p1 is the coefficient of the linear term and p0 is the constant term. Plots with linear fits for all other iEta values are at the end of the Appendix F.

A list of the coefficients of linear and constant terms is given in Table 7.5.

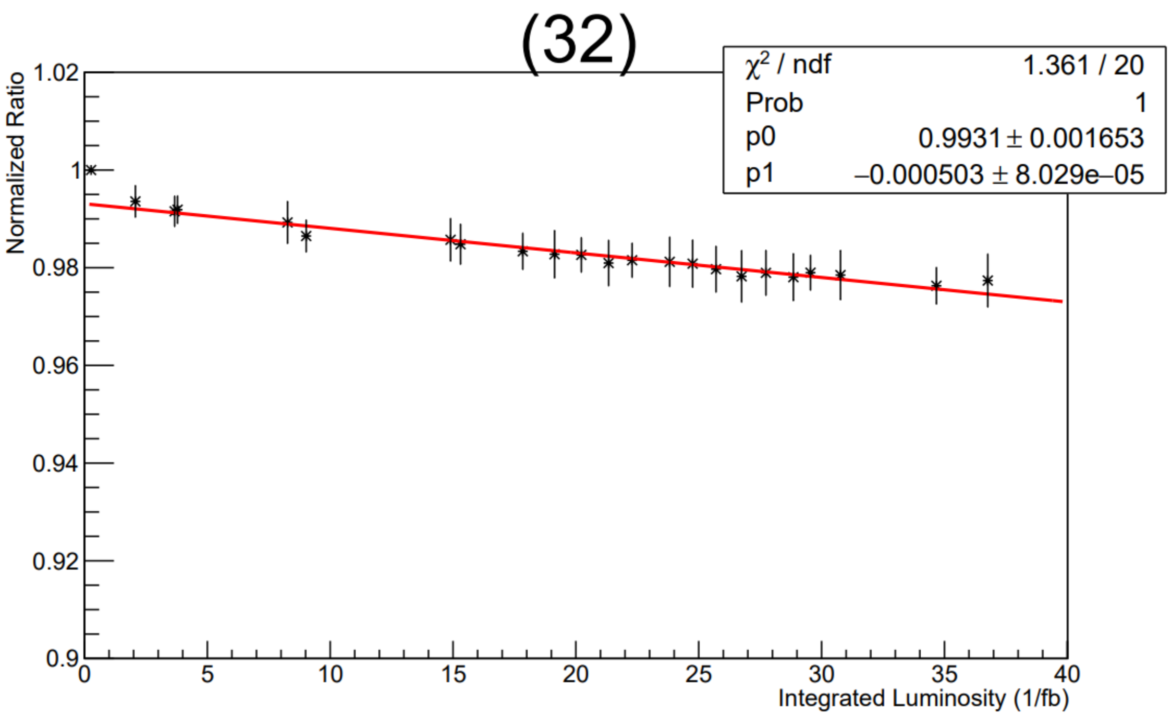

Figure 7.17. Graph of normalized ratio with respect to the integrated luminosity averaged over iPhi for iEta 32 for the runs which took place in less than 1 hour after the nearest collision (with linear fit).

Table 7.3. The list of the coefficients of linear and constant terms of all iEta values from the linear fits of normalized ratio graphs with respect to the integrated luminosity averaged over iPhi for the runs which took place in less than 1 hour after the nearest collision.

iEta	**p1**	**p0**
30	-0.0002806 ± 0.00002729	0.9973 ± 0.0006763
-30	-0.0003062 ± 0.00002939	0.9976 ± 0.000549
32	-0.000503 ± 0.00008029	0.9931 ± 0.001653
-32	-0.0005726 ± 0.00005189	0.9949 ± 0.0008918
34	-0.0007166 ± 0.00006265	0.9866 ± 0.001484
-34	-0.0008342 ± 0.00006874	0.9876 ± 0.001141
36	-0.0009857 ± 0.00006023	0.9791 ± 0.001157
-36	-0.0009454 ± 0.00008077	0.9796 ± 0.001583
38	-0.0009666 ± 0.0000544	0.9698 ± 0.001111
-38	-0.001081 ± 0.00008161	0.9737 ± 0.00181
40	-0.0009334 ± 0.00005399	0.9662 ± 0.001211
-40	-0.001154 ± 0.00002719	0.9715 ± 0.0003803
41	-0.0007074 ± 0.0001428	0.97 ± 0.002941
-41	-0.0007468 ± 0.00006109	0.9701 ± 0.0006223

7.9.5. Averaging HF- and HF+ Results

In previous sections and also in commissioning [5], it is seen that minus iEta and plus iEta display similar results (which is expected due to the symmetry). Therefore, they are averaged to get plots representing both HF- and HF+ in a single picture for each iEta value.

The linear fits of the normalized plots for all iEta values averaged over HF- and HF+ are given in Figure 7.23.

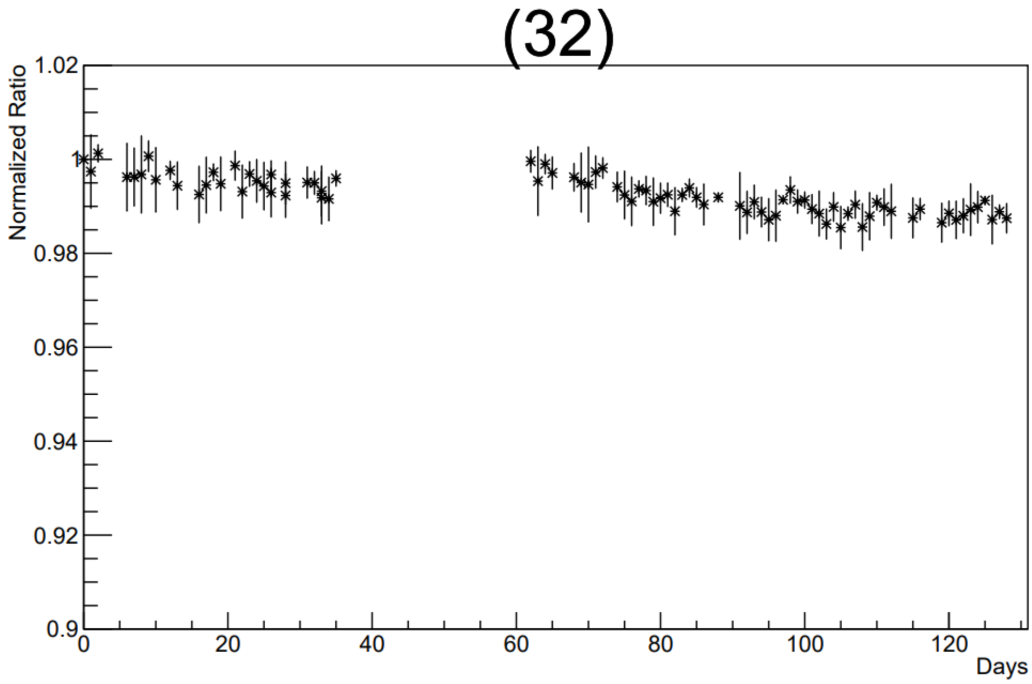

Figure 7.18. Graph of doubly normalized ratio with respect to time averaged over iPhi for iEta 32

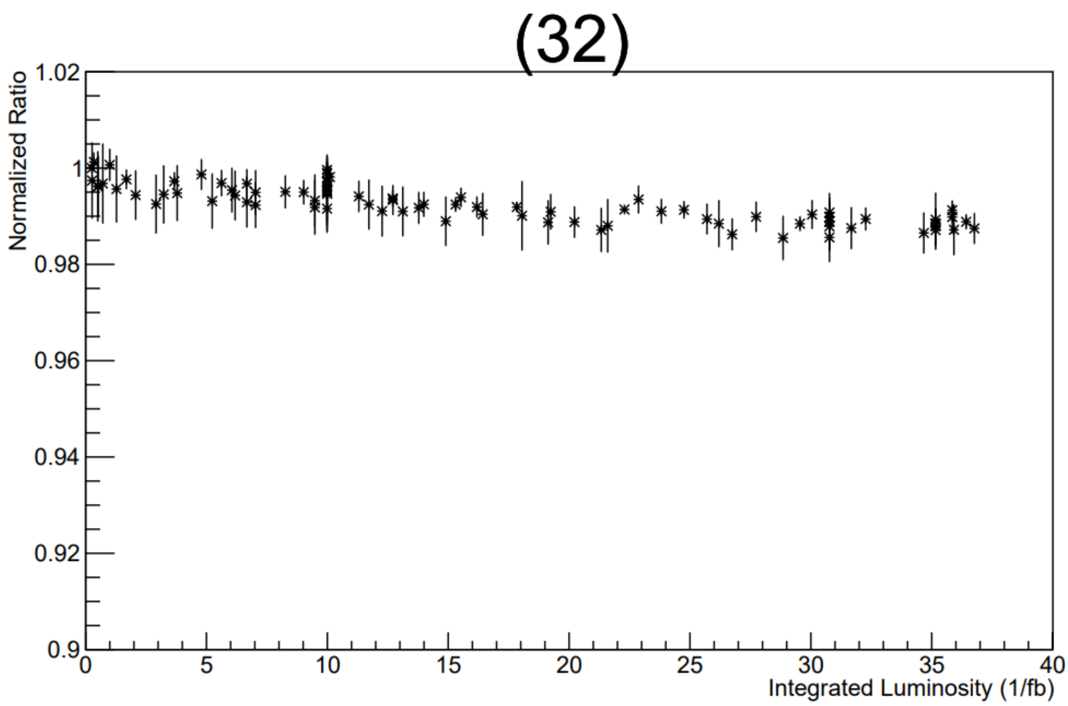

Figure 7.19. Graph of doubly normalized ratio with respect to the integrated luminosity averaged over iPhi for iEta 32

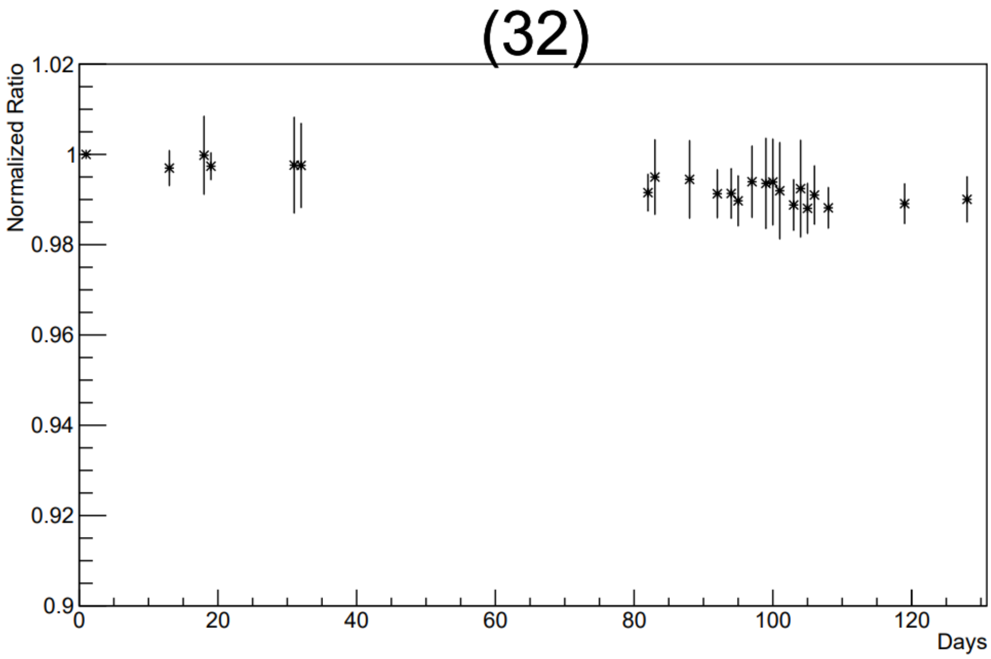

Figure 7.20. Graph of doubly normalized ratio with respect to time averaged over iPhi for iEta 32 for the runs which took place in less than 1 hour after the nearest collision.

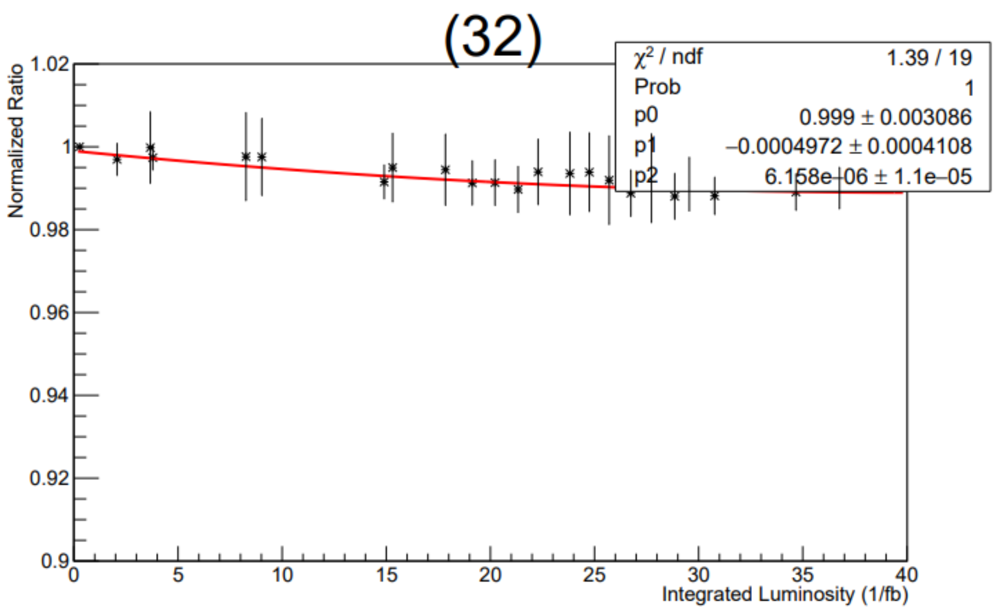

Figure 7.21. Graph of doubly normalized ratio with respect to the integrated luminosity averaged over iPhi for iEta 32 for the runs which took place in less than 1 hour after the nearest collision (with quadratic fit).

Table 7.4. The list of the coefficients of quadratic terms (p2), linear terms (p1) and constant terms (p0) of all iEta values from the quadratic fits of normalized ratio graphs with respect to the integrated luminosity averaged over iPhi for the runs which took place in less than 1 hour after the nearest collision.

iEta	**p2**	**p1**	**p0**
30	0	0	1
-30	0	0	1
32	0.000006158 ± 0.000011	-0.0004972 ± 0.0004108	0.999 ± 0.003086
-32	0.00000359 ± 0.000007717	-0.0003811 ± 0.0002618	0.9979 ± 0.001663
34	0.000007668 ± 0.000005486	-0.0007875 ± 0.0001955	0.9934 ± 0.001602
-34	0.00001049 ± 0.000006074	-0.0008436 ± 0.00019	0.9911 ± 0.001235
36	0.00001535 ± 0.000006826	-0.001301 ± 0.0002582	0.9872 ± 0.002425
-36	0.00001593 ± 0.00001069	-0.001207 ± 0.0003912	0.9851 ± 0.002834
38	0.00001639 ± 0.000005869	-0.001407 ± 0.0002127	0.9801 ± 0.001738
-38	0.000006358 ± 0.00000696	-0.001016 ± 0.0002611	0.977 ± 0.002003
40	0.00001512 ± 0.000007383	-0.0014 ± 0.0003342	0.9769 ± 0.003481
-40	0.00001432 ± 0.000006402	-0.001221 ± 0.0002076	0.974 ± 0.001131
41	-0.000001879 ± 0.00001685	-0.000465 ± 0.0006443	0.9751 ± 0.005478
-41	-0.0000002347 ± 0.000009738	-0.0004537 ± 0.0003125	0.9727 ± 0.001476

A list of the coefficients of linear and constant terms from the linear fits is given in Table 7.6.

The linear fits of the doubly normalized plots for all iEta values averaged over HF- and HF+ are given in Figure 7.24.

A list of the coefficients of linear and constant terms from the linear fits of doubly normalized graphs is given in Table 7.7.

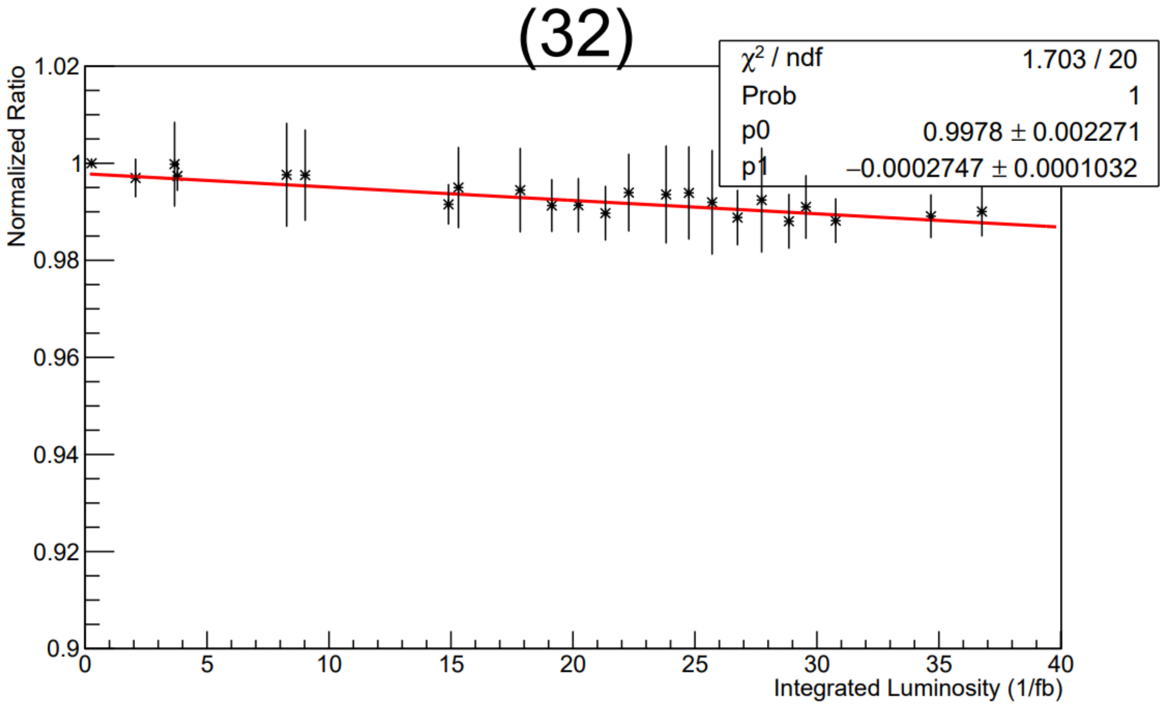

Figure 7.22. Graph of doubly normalized ratio with respect to the integrated luminosity averaged over iPhi for iEta 32 for the runs which took place in less than 1 hour after the nearest collision (with linear fit).

The constant terms obtained in the fits to the results of the HF Online Radiation Damage Monitoring System are expected to be 1 since the ratio should be 1 at zero luminosity. However, the constant terms of the fits are not exactly 1, since the ratio that we used to normalize our results belongs to a run taken at a nonzero luminosity value. Therefore, an offset equal to 1 minus the value of the constant term is applied to all data points to shift the fit upwards to bring the constant term near to one, without changing the slope (Figure 7.25 and Figure 7.26).

The list of the coefficients of linear and constant terms from the linear refits of the normalized ratio graphs after the correction mentioned above is given in Table 7.8.

The list of the coefficients of linear and constant terms from the linear refits of the corrected doubly normalized graphs is given in Table 7.9.

Table 7.5. The list of the coefficients of linear and constant terms of all iEta values from the linear fits of doubly normalized ratio graphs with respect to the integrated luminosity averaged over iPhi for the runs which took place in less than 1 hour after the nearest collision.

iEta	**p1**	**p0**
30	0	1
-30	0	1
32	-0.0002747 $\pm$ 0.0001032	0.9978 $\pm$ 0.002271
-32	-0.0002634 $\pm$ 0.00006705	0.9973 $\pm$ 0.001178
34	-0.0005261 $\pm$ 0.0000568	0.992 $\pm$ 0.001238
-34	-0.0005251 $\pm$ 0.0000455	0.9895 $\pm$ 0.000813
36	-0.0007517 $\pm$ 0.00008432	0.9834 $\pm$ 0.001756
-36	-0.0006436 $\pm$ 0.0000993	0.9822 $\pm$ 0.002045
38	-0.0008393 $\pm$ 0.00006207	0.9771 $\pm$ 0.00136
-38	-0.0007837 $\pm$ 0.00006014	0.9757 $\pm$ 0.001435
40	-0.0007329 $\pm$ 0.00007444	0.971 $\pm$ 0.001965
-40	-0.0007725 $\pm$ 0.00005304	0.9723 $\pm$ 0.0008289
41	-0.0005342 $\pm$ 0.0001741	0.9755 $\pm$ 0.003942
-41	-0.000461 $\pm$ 0.00007708	0.9727 $\pm$ 0.001055

The results of radiation damage estimates calculated from the collision data were received. The estimated correction factors are given in Figure 7.27 (A. Stepennov, personal communication, January 23, 2024).

Adding the correction factors over the doubly normalized ratio plots averaged over HF- and HF+, the plots in Figure 7.28 are obtained.

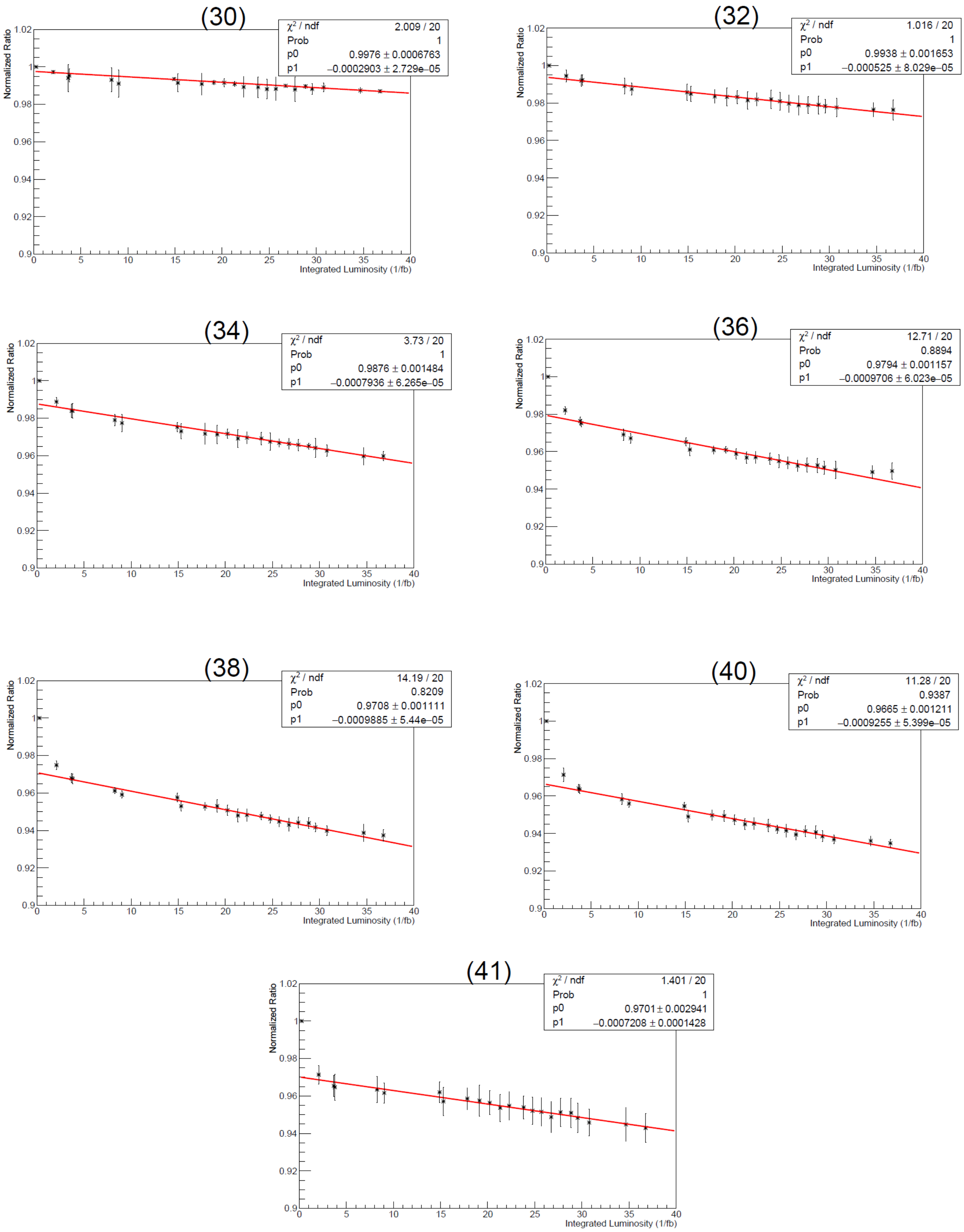

Figure 7.23. Graphs of normalized ratio with respect to integrated luminosity averaged over HF- and HF+ (with linear fit).

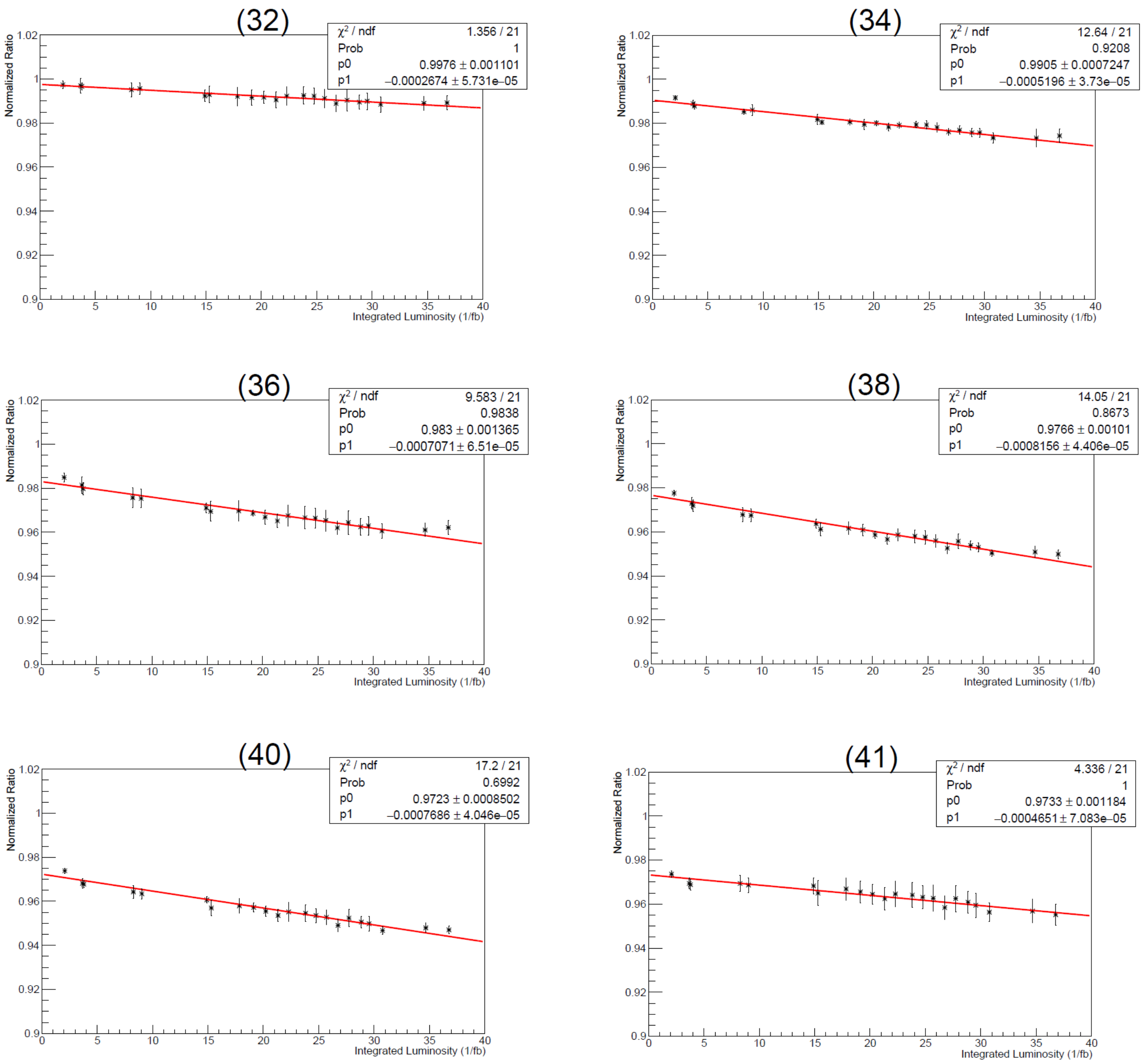

Figure 7.24. Graphs of doubly normalized ratio with respect to integrated luminosity averaged over HF- and HF+ (with linear fit).

Table 7.6. The list of the coefficients of linear and constant terms of all iEta values from the linear fits of normalized ratio graphs with respect to the integrated luminosity averaged over HF- and HF+.

iEta	**p1**	**p0**
30	-0.0002903 ± 2.729e-05	0.9976 ± 0.0006763
32	-0.000525 ± 8.029e-052	0.9938 ± 0.001653
34	-0.0007936 ± 6.265e-05	0.9876 ± 0.001484
36	-0.0009706 ± 6.023e-05	0.9794 ± 0.001157
38	-0.0009885 ± 5.44e-05	0.9708 ± 0.001111
40	-0.0009255 ± 5.399e-05	0.9665 ± 0.001211
41	-0.0007208 ± 0.0001428	0.9701 ± 0.002941

Table 7.7. The list of the coefficients of linear and constant terms of all iEta values from the linear fits of doubly normalized ratio graphs with respect to the integrated luminosity averaged over HF- and HF+.

iEta	**p1**	**p0**
32	-0.0002674 ± 5.731e-05	0.9976 ± 0.001101
34	-0.0005196 ± 3.73e-05	0.9905 ± 0.0007247
36	-0.0007071 ± 6.51e-05	0.983 ± 0.001365
38	-0.0008156 ± 4.406e-05	0.9766 ± 0.00101
40	-0.0007686 ± 4.046e-05	0.9723 ± 0.0008502
41	-0.0004651 ± 7.083e-05	0.9733 ± 0.001184

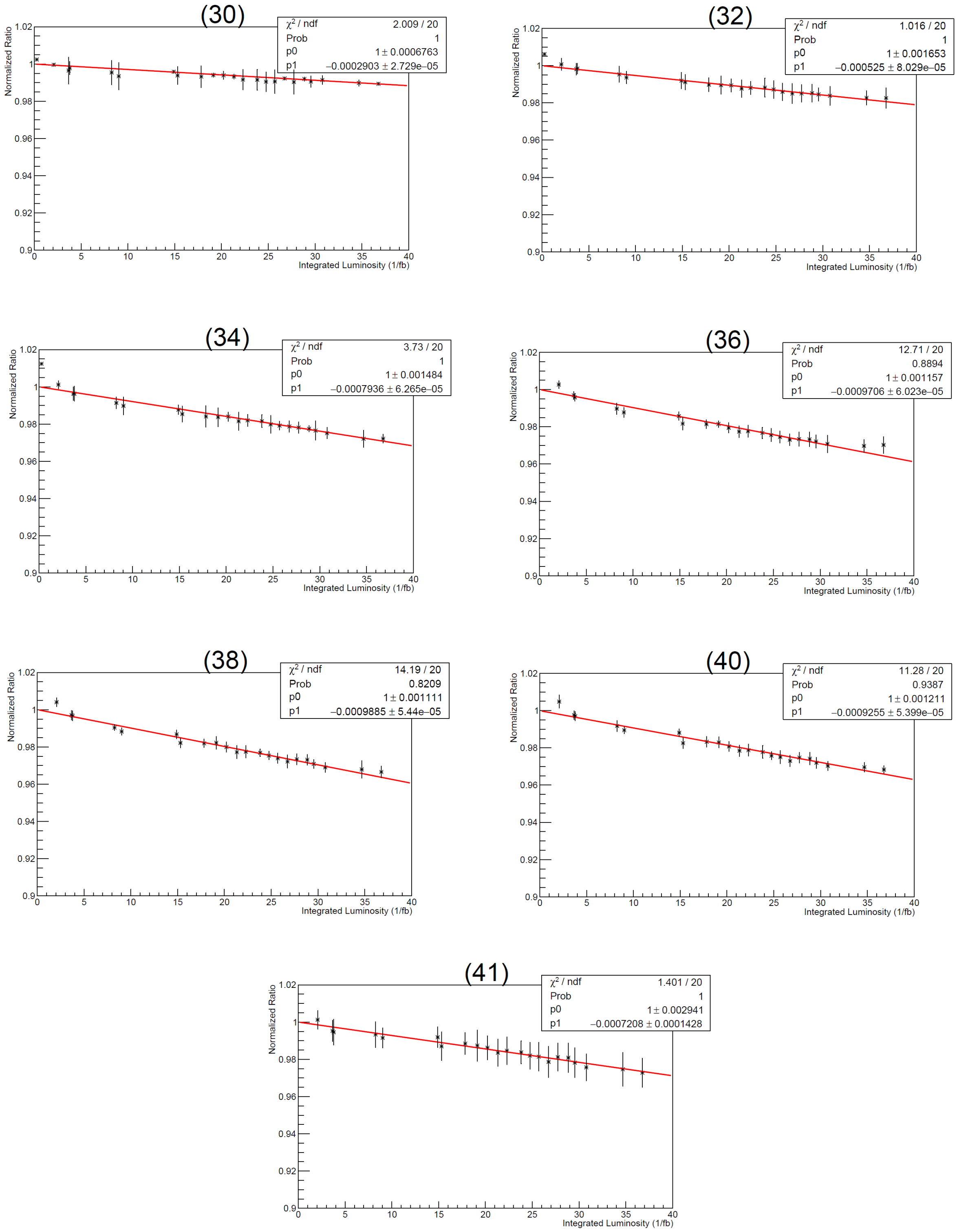

Figure 7.25. Graphs of normalized ratio with respect to integrated luminosity averaged over HF- and HF+ (with linear fit, corrected).

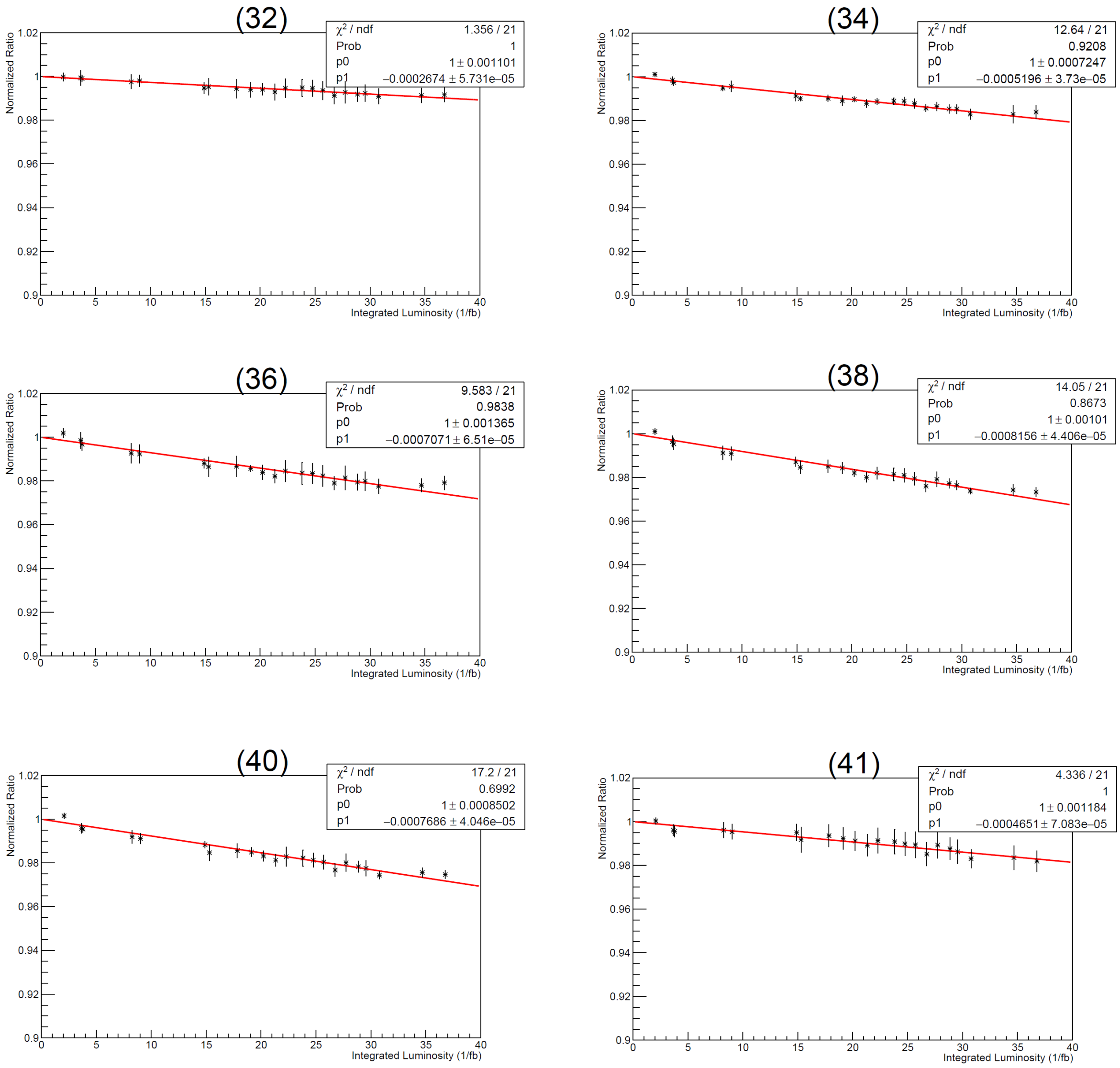

Figure 7.26. Graphs of doubly normalized ratio with respect to integrated luminosity averaged over HF- and HF+ (with linear fit, corrected).

Table 7.8. The list of the coefficients of linear and constant terms of all iEta values from the linear fits of the corrected normalized ratio graphs with respect to the integrated luminosity averaged over HF- and HF+.

iEta	**p1**	**p0**
30	-0.0002903 ± 2.729e-05	1 ± 0.0006763
32	-0.000525 ± 8.029e-052	1 ± 0.001653
34	-0.0007936 ± 6.265e-05	1 ± 0.001484
36	-0.0009706 ± 6.023e-05	1 ± 0.001157
38	-0.0009885 ± 5.44e-05	1 ± 0.001111
40	-0.0009255 ± 5.399e-05	1 ± 0.001211
41	-0.0007208 ± 0.0001428	1 ± 0.002941

Table 7.9. The list of the coefficients of linear and constant terms of all iEta values from the linear fits of the corrected doubly normalized ratio graphs with respect to the integrated luminosity averaged over HF- and HF+.

iEta	**p1**	**p0**
32	-0.0002674 ± 5.731e-05	1 ± 0.001101
34	-0.0005196 ± 3.73e-05	1 ± 0.0007247
36	-0.0007071 ± 6.51e-05	1 ± 0.001365
38	-0.0008156 ± 4.406e-05	1 ± 0.00101
40	-0.0007686 ± 4.046e-05	1 ± 0.0008502
41	-0.0004651 ± 7.083e-05	1 ± 0.001184

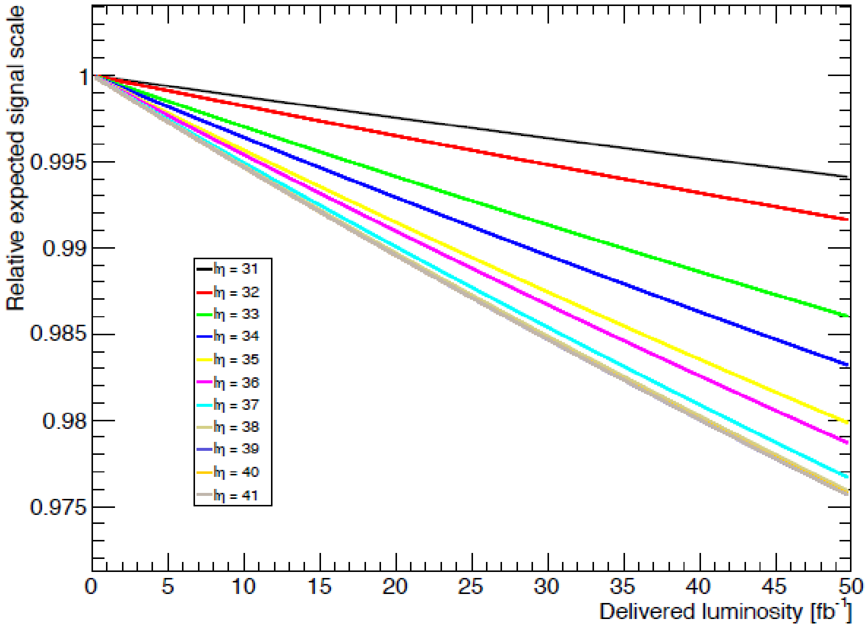


```
#ieta CorrFactor
ieta   31:1, 0.999293, 0.998598, 0.997914, 0.99724, 0.996577, 0.995923, 0.99528, 0.994645
ieta   32:1, 0.998989, 0.997996, 0.997019, 0.996058, 0.995113, 0.994181, 0.993265, 0.992361
ieta   33:1, 0.998286, 0.996605, 0.994954, 0.993334, 0.991741, 0.990177, 0.988638, 0.987126
ieta   34:1, 0.997917, 0.995876, 0.993875, 0.991912, 0.989986, 0.988095, 0.986238, 0.984413
ieta   35:1, 0.997458, 0.994971, 0.992538, 0.990155, 0.98782, 0.985533, 0.98329, 0.98109
ieta   36:1, 0.99729, 0.994642, 0.992052, 0.989517, 0.987037, 0.984607, 0.982227, 0.979894
ieta   37:1, 0.996963, 0.994001, 0.99111, 0.988289, 0.985533, 0.98284, 0.980207, 0.977632
ieta   38:1, 0.996807, 0.993697, 0.990668, 0.987716, 0.984836, 0.982027, 0.979284, 0.976606
ieta   39:1, 0.996724, 0.993538, 0.990439, 0.987422, 0.984484, 0.981621, 0.978831, 0.976109
ieta   40:1, 0.996691, 0.993478, 0.990355, 0.987318, 0.984363, 0.981488, 0.978687, 0.975958
ieta   41:1, 0.996727, 0.993544, 0.990447, 0.987432, 0.984496, 0.981635, 0.978846, 0.976125
```

```
ranges (fb):
0 - 5, 5 - 10, 10 - 15, 15 - 20, 20 - 25, 25 - 30, 30 - 35, 35 - 40, 40 - 45,
```

Figure 7.27. The estimated correction factors from the collision data.

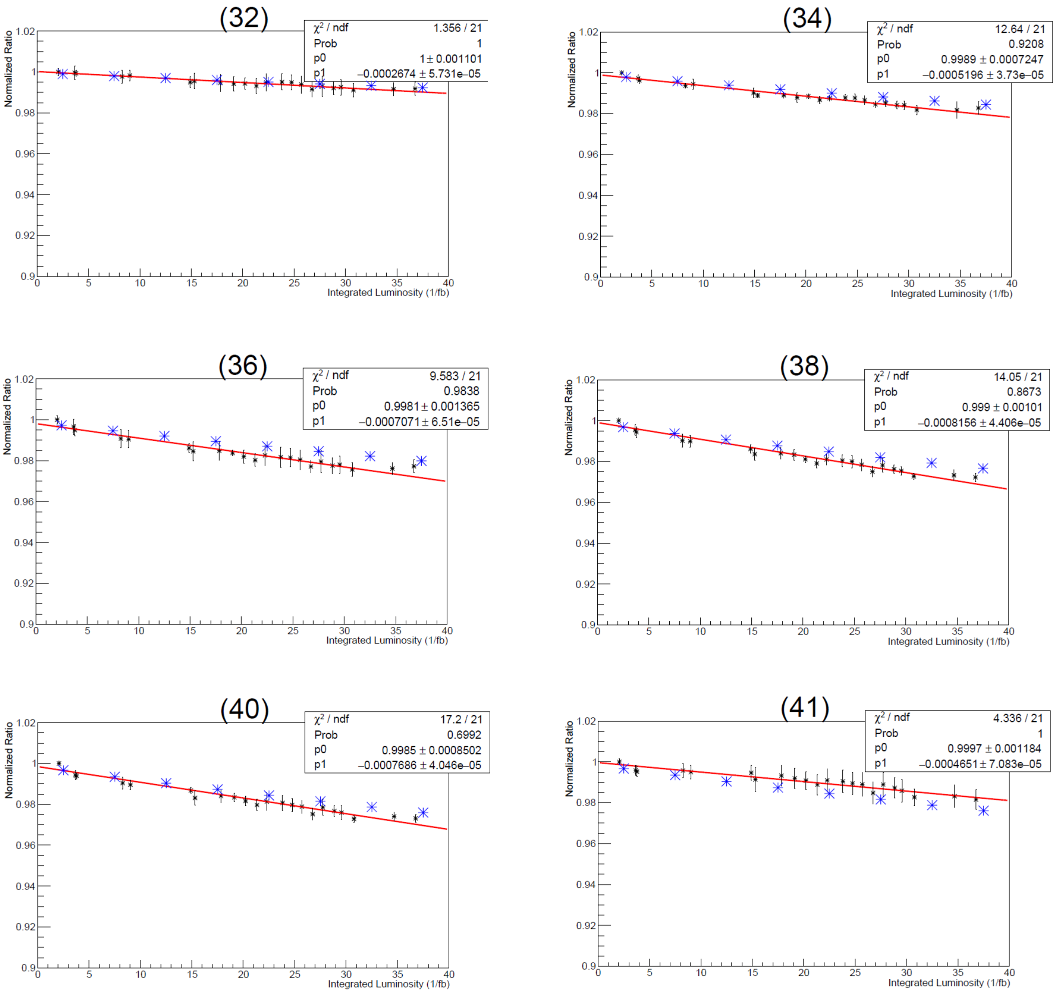

Figure 7.28. Graphs of doubly normalized ratio with respect to integrated luminosity averaged over HF- and HF+ with linear fit on which the correction factors obtained from the collision data are added.

7.10. 2023 Results

In total, there were 158 runs examined in 2023 data. Among these 158 runs, 29 of them are either empty or have meaningless "$\frac{Q_1+Q_2}{Q_t}$ versus Events" graphs, which are labeled as "broken runs". An example for a broken run is given in Figure 7.29.

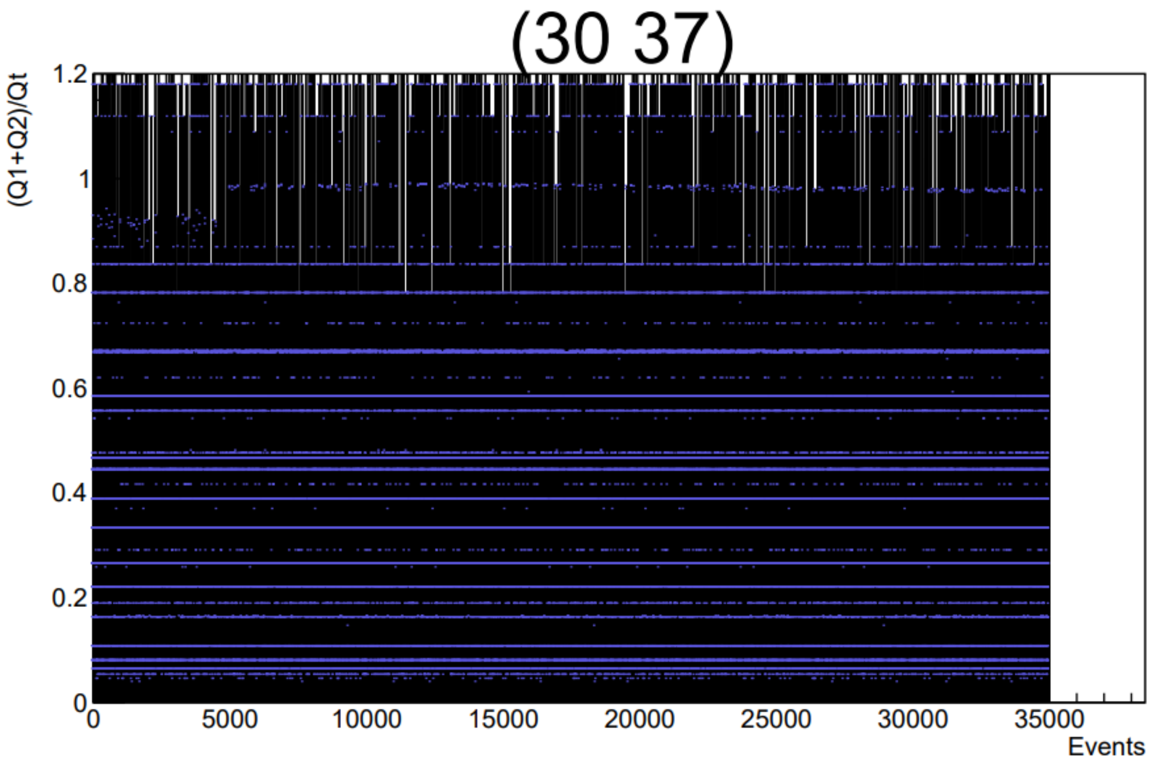

Figure 7.29. Graph of $\frac{Q_1+Q_2}{Q_t}$ versus Events for iEta 32 channel (30 37) for run 376005, as an example for a broken run.

Among the total 158 runs, 49 of them have "$\frac{Q_1+Q_2}{Q_t}$ versus Events" graphs reaching 1 for some set of events for every channels. These 49 runs are labeled as "good runs". Unfortunately, most of them were much after 16th of July, when collisions stopped until September. After September, there were heavy ion collisions where damage due to delivered luminosity is negligible. Only eight of the "good runs" are before 16th of July. These eight runs are also some of the first runs of 2023.

The rest are 80 runs with "$\frac{Q_1+Q_2}{Q_t}$ versus Events" graphs which do not reach 1 at any set of events for some channels. These are labeled as "bad runs". These bad runs could still be useful if one focuses on the channels at which "$\frac{Q_1+Q_2}{Q_t}$ versus Events" graph reaches 1 for some set of events and drops the ones not reaching 1.

7.10.1. First "Good Runs" in 2023

The first eight good runs in 2023 are given in table below in Table 7.10. The normalized ratio graph for these eight runs are given in Figure 7.30.

In Figure 7.30, the ratios are normalized to the ratio of 363294. However, there is a huge time period between 363294 and the other seven runs. Since this run is long before the start of the collisions, fibers may have some recovery also. Therefore it could be much better if 363294 is thrown away. Omitting 363294, the normalized ratio graph for the seven remaining runs are given in Figure 7.31.

Table 7.10. The list of the first eight good runs from 2023 data with corresponding dates.

	Run Number	**Date**	**Int. Lumi.(1/fb)**
1	363294	01/02/23	0
2	367152	08/05/23	2.208
3	367243	09/05/23	2.964
4	367283	10/05/23	3.558
5	367346	11/05/23	4.104
6	367460	13/05/23	4.744
7	367528	15/05/23	6.070
8	367558	16/05/23	6.364

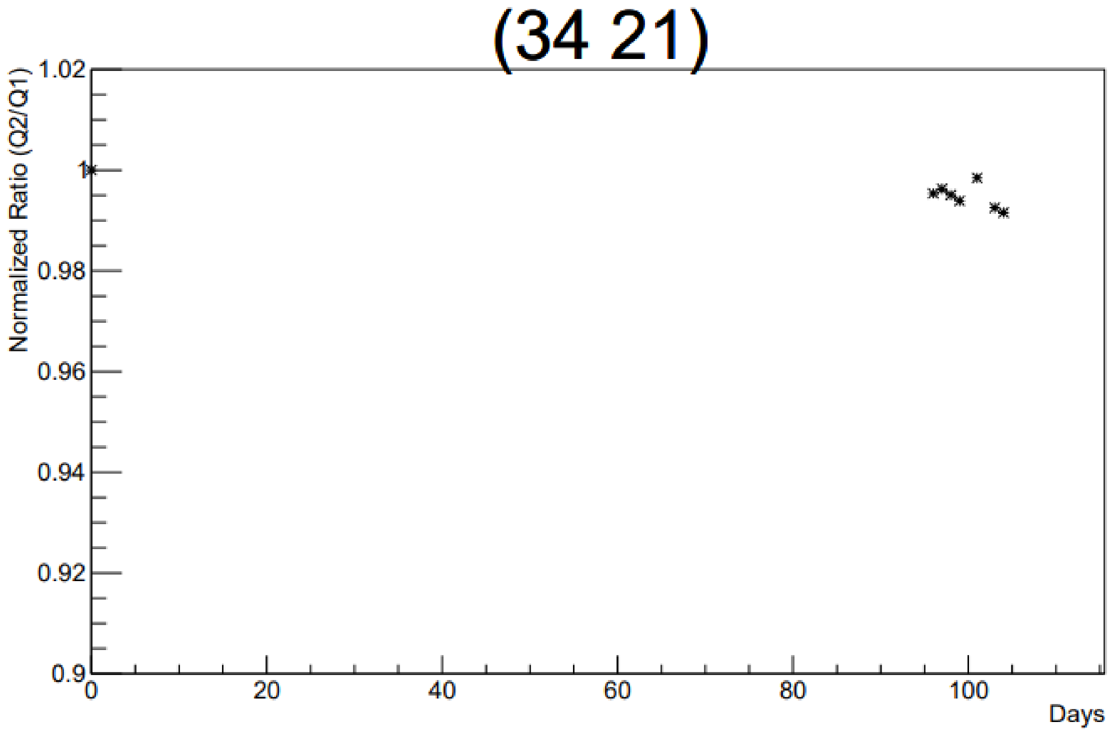

Figure 7.30. Graph of normalized ratio with respect to time for iEta 34 and iPhi 21 (normalized by 363294)

In Figure 7.31, it seems there is a recovery in 367460. This is due to the 14 hours of time duration between 367460 and preceding collision. Also, the preceding collision has a low delivered luminosity value. Therefore, run 367460 could be thrown away, as well. Omitting 367460, the normalized ratio graph for the six remaining runs are given in Figure 7.32.

7.10.2. Salvaging "Bad Runs" for 2023

In Chapter 7.10, "bad runs" are defined as the runs with "$\frac{Q_1+Q_2}{Q_t}$ versus Events" graphs which do not reach 1 at any set of events for some channels. In these runs, some results can be obtained from the channels where "$\frac{Q_1+Q_2}{Q_t}$ versus Events" graphs do reach 1 for some set of events.

Additionally, it is stated above that at 16th of July collisions stopped until September. Among these 80 runs, 56 runs are until 20th of July. These are taken into consideration for the analysis.

Inspecting which channels reach 1 and give proper results, the channels in Table 7.11 can be selected.

For iEta 30 and iPhi 1, the normalized ratio graph for these 56 selected runs are given below in Figure 7.33.

Then, 21 runs which took place in less than 1 hour after the nearest collision are selected and they are plotted separately in Figure 7.34.

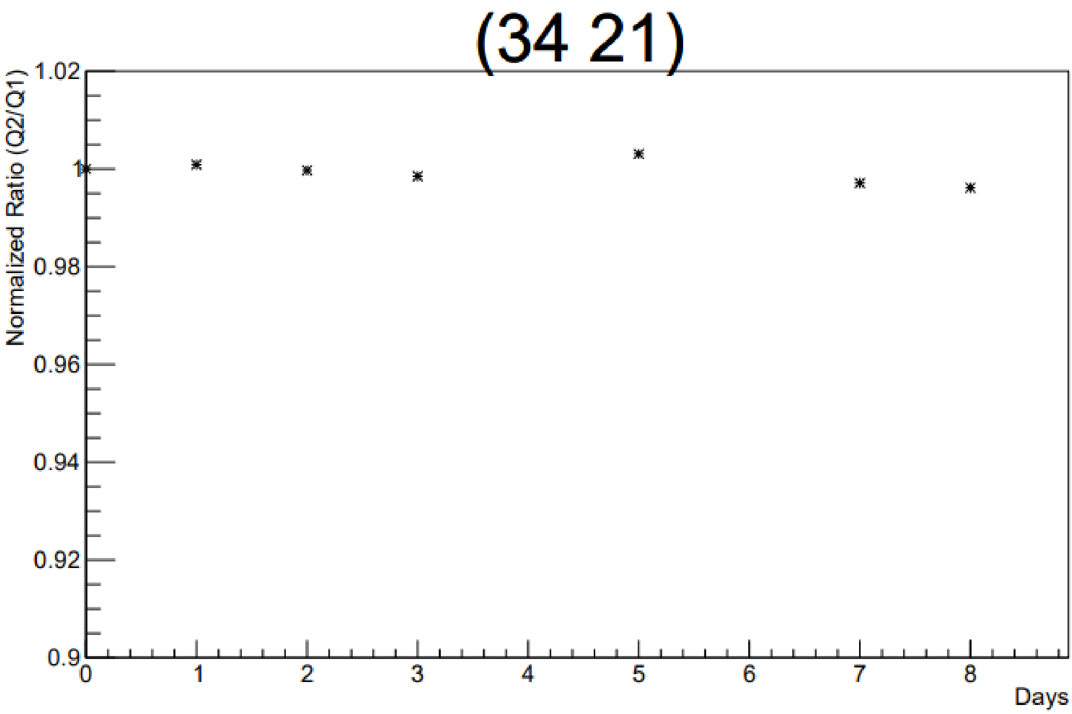

Figure 7.31. Graph of normalized ratio with respect to time for iEta 34 and iPhi 21 (normalized by 367152), omitting 363294.

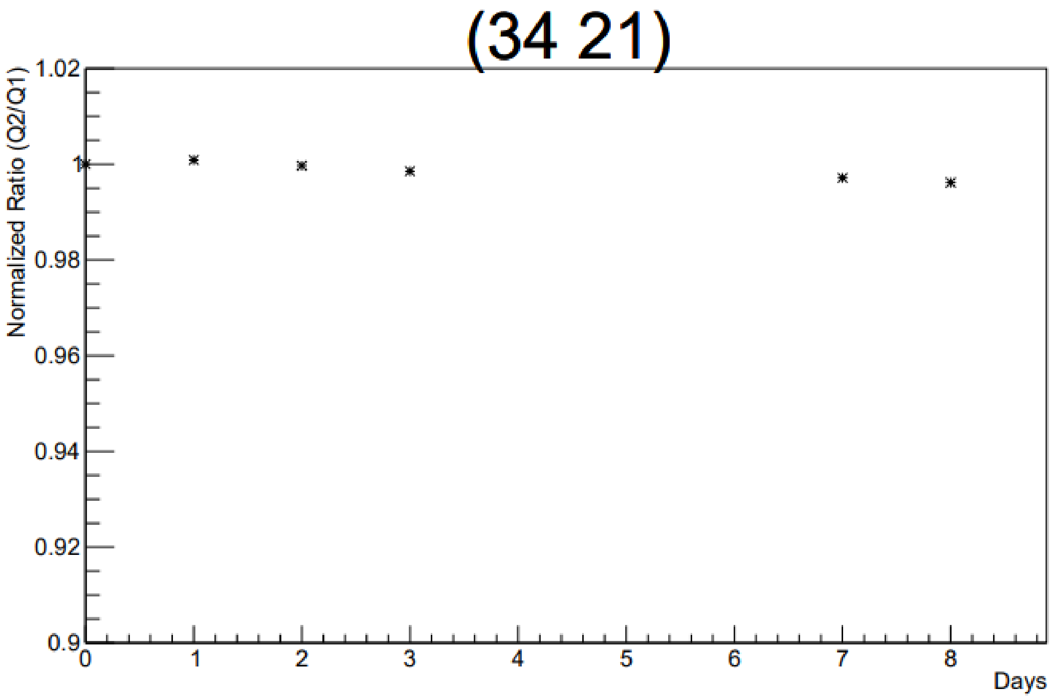

Figure 7.32. Graph of normalized ratio with respect to time for iEta 34 and iPhi 21 (normalized by 367152), omitting 367460 and 363294

Table 7.11. The possible good channels in “bad” runs.

	iEta	**iPhi**
1	30	1
2	30	37
3	30	57
4	32	57
5	34	57
6	-30	15

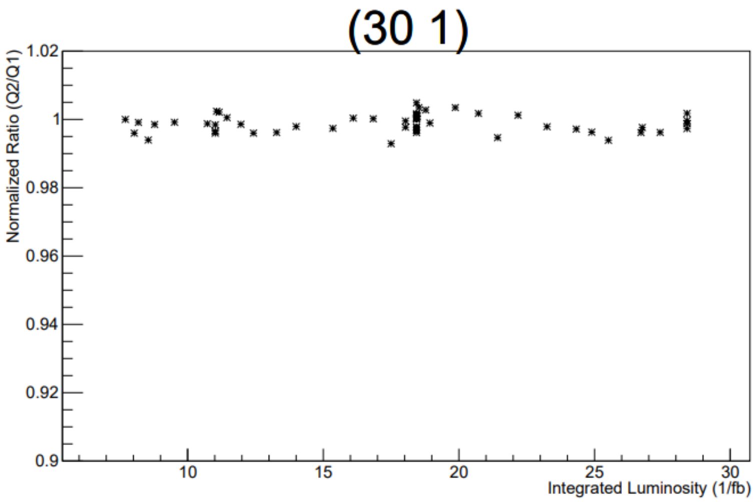

Figure 7.33. Graph of normalized ratio with respect to integrated luminosity for iEta 30 and iPhi 1.

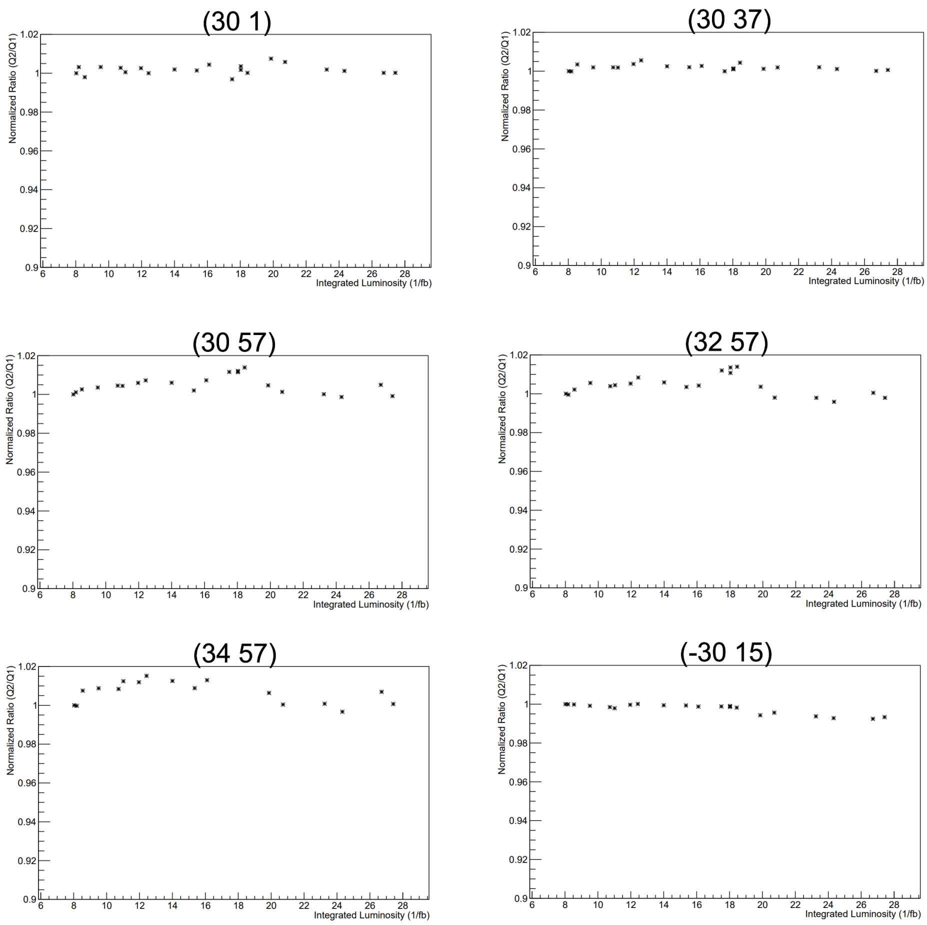

Figure 7.34. Graphs of normalized ratio with respect to integrated luminosity for the runs which took place in less than 1 hour after the nearest collision.

In pedestal graphs, some channels seems to have too much pedestal value. Apparently in these channels some of the events are like those events in the “broken runs” and there is noise in all the time slots producing large pedestal values. For these channels, it is thought that neglecting pedestals might give better results than subtracting pedestals. In this manner, the normalized ratio graphs are generated without subtracting any pedestals. After this, two more channels, namely (36, 1) and (41, 71), are better.

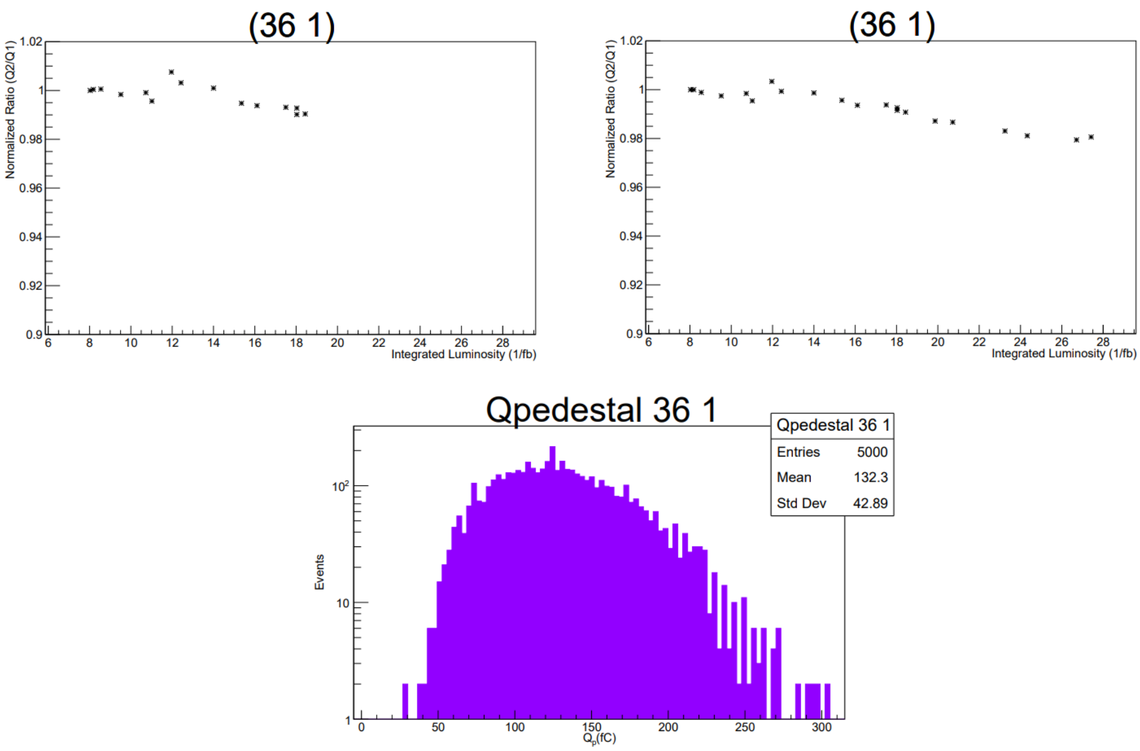

Figure 7.35. Graph of normalized ratio with respect to integrated luminosity for the runs which took place in less than 1 hour after the nearest collision for iEta 36 and iPhi 1 with(at top left) and without(at top right) pedestal subtraction. (Notice that with pedestal subtraction, some data points are out of the plot range.) The pedestal graph is also given (below).

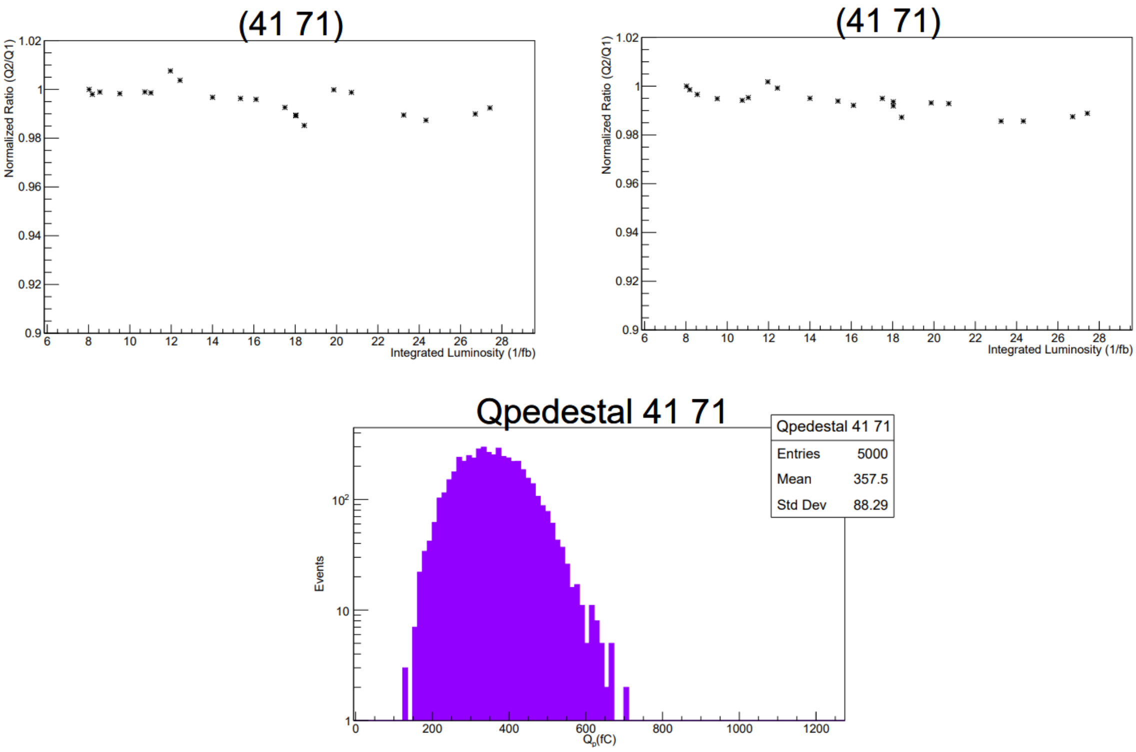

Figure 7.36. Graph of normalized ratio with respect to integrated luminosity for the runs which took place in less than 1 hour after the nearest collision for iEta 41 and iPhi 71 with(at top left) and without(at top right) pedestal subtraction. The pedestal graph is also given (below).

To understand the pedestal graphs of channels (36, 1) and (41, 71) better, the pedestal graphs of (30, 1) and (34, 57) are displayed in Figure 7.37 below.

It is obvious that the pedestal values of (36, 1) and (41, 71) are too high for some events and one can get better results if these high pedestals are not subtracted.

These 2023 runs have many complications and even though some of the data may seem to be corrected for these complications, as explained above, the results obtained still have large unexplained fluctuations and do not seem to be useful.

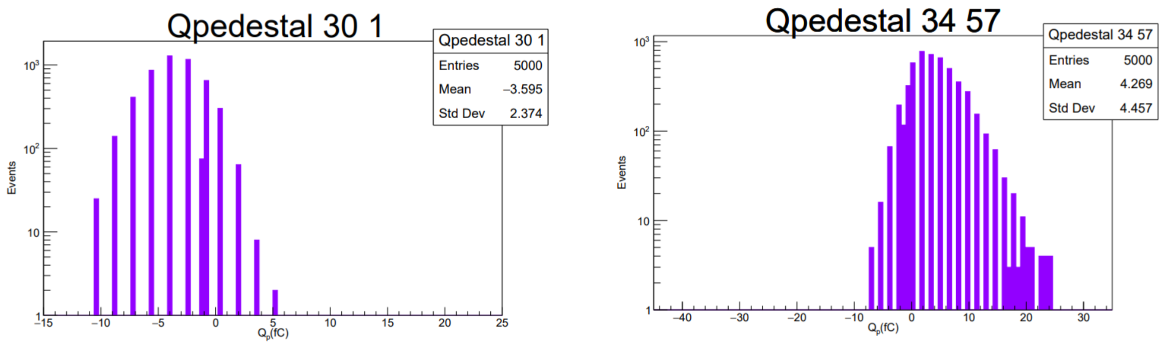

Figure 7.37. The pedestal graphs of (30, 1) and (34, 57).

7.10.3. Last "Good Runs" in 2023

There are 41 "good runs" after 16th of July, when collisions stopped. Therefore it is not expected to see any radiation damage in these runs. On the contrary, some recovery is expected. 15 runs are selected randomly from these 41 last "good runs". Each five of them are selected from different groups which are separated with "broken runs" mentioned above.

The normalized ratio graph for these 15 runs are given below in Figure 7.38. It seems that the results for these runs show a flat curve. Obviously, the fibers have recovered and stay recovered at a constant level. These results just confirm this fact and do not say anything about the radiation damage of the fibers in 2023 run.

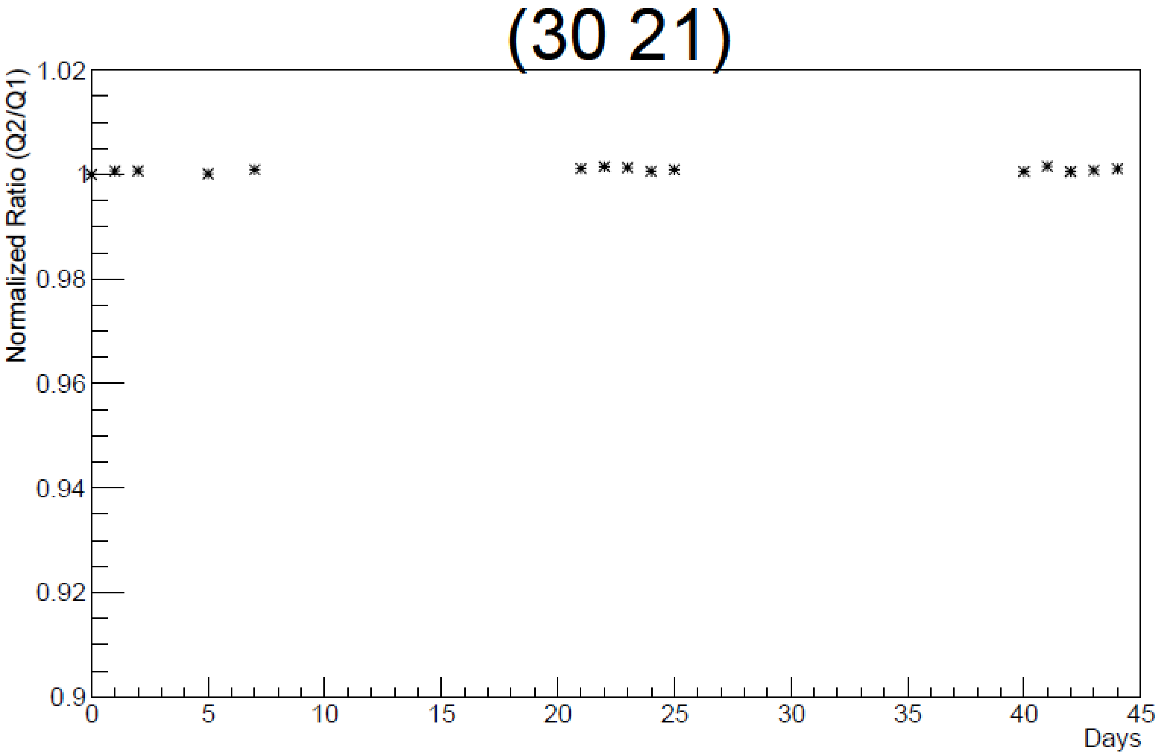

Figure 7.38. Graph of normalized ratio with respect to time for iEta 30 and iPhi 21 for randomly selected 15 runs from last “good runs” in 2023.

8. CONCLUSION

The HF calorimeter is based on quartz fibers. The transparency of these quartz fibers decreases due to the radiation damage. This radiation damage is monitored via the HF Online Radiation Damage Monitoring System. The data taken in 2022 and 2023 are analysed and reported in this thesis.

The regions with high η receive higher dose of the radiation. Therefore, the damage in the fibers in these regions are expected to be more whereas the damage is expected to be low in the lower iEta values. As expected, it can be seen that the damage of the fibers with higher iEta values is much more pronounced. In these high iEta parts, the recovery is also apparent when the collisions stop. The recovery which shows up soon after the collisions stop indicates that the runs taken with the HF Online Radiation Damage Monitoring system should be as close as possible to the collision runs.

The quadratic fits are imposed both on the normalized ratio with respect to integrated luminosity and on the doubly normalized ratio with respect to integrated luminosity. However, since the coefficient of quadratic terms are very small in general and even smaller than their uncertainty for some iEta values, as can be seen in Tables 7.2 and 7.4, linear fits are also imposed. From the linear fits of the normalized ratio and the doubly normalized ratio with respect to integrated luminosity, negative value for the coefficient of linear terms are obtained as expected (Tables 7.3 and 7.5).

The radiation damage does not depend on azimuthal angle as expected since the whole CMS is cylindrically symmetric. In addition, there is no difference between results from HF+ and HF- parts, which is also expected because of the symmetry in the CMS with respect to the collision point. Hence we can average the results for specific iEta values (averaged over iPhi values) of both sides to obtain a single set of representations for the HF detectors (section 7.9.5).

Looking at the graphs of normalized ratio with respect to integrated luminosity averaged over HF- and HF+ in Figure 7.25, a total of 2 to 4 % radiation damage is observed for all iEta values during the 2022 run period.

Comparing doubly normalized ratio graphs averaged over HF- and HF+ with the correction factors obtained from collision data in Figure 7.28, it is seen that these correction factors show less radiation damage than the HF Online Radiation Damage Monitoring System for 2022 for almost all iEta values.

On the other hand, 2023 data has many complications and it is necessary to abandon it. Only initial few runs produced acceptable results, but they are inconclusive to produce any useful information on the radiation damage for 2023 run period.

In 2024, we plan to make sure that the timing problems occurred during 2023 are resolved and the radiation damage monitoring in 2024 is run smoothly. Afterwards, we plan to analyze 2024 “local run” data. In addition to the “local runs” taken outside of the collision data, these measurements can be done in between collisions, so called “abort gap”. In fact, such data taking has started and we plan to analyze them. “Abort gap” data are expected to have minimal fiber recovery.

REFERENCES

1. Bilki, B. and Y. Onel, "Design, Construction and Commissioning of the Upgrade Radiation Damage Monitoring System of the CMS Hadron Forward Calorimeters", *2018 IEEE Nuclear Science Symposium and Medical Imaging Conference Proceedings*, pp. 1–4, Sydney, NSW, Australia, 2018.

2. Gülmez, E., I. Loc, B. Gönültaş and Y. Onel, "Commissioning Results of the CMS-HF Online Radiation Damage Monitoring System and Implications for Run III", *Proceedings of 41st International Conference on High Energy physics*, Vol. 414, p. 631, Bologna, Italy, 2022.

3. Gönültaş, B., E. Gülmez and Y. Onel, "Comparison of the Radiation Damage Results From the Collision Data and the HF Online Radiation Damage Monitoring System", *2023 IEEE Nuclear Science Symposium, Medical Imaging Conference and International Symposium on Room-Temperature Semiconductor Detectors*, p. 1, Vancouver, Canada, 2023.

4. Gülmez, E., B. Gönültaş and Y. Onel, "Performance of the New CMS-HF Online Radiation Damage Monitoring System", *20th International Conference on Calorimetry in Particle Physics*, Tsukuba, Japan, 2024.

5. Zöğ, I., *Radiation Damage Monitoring in Hadron Forward Calorimetry*, M.S. Thesis, Boğaziçi University, 2019.

6. Lopienska, E., "CERN's Accelerator Complex", 2022, `https://cds.cern.ch/record/2800984`, accessed on April 8, 2024.

7. Brice, M., "CMS Central Beampipe Installation", 2021, `https://cds.cern.ch/record/2758629`, accessed on April 8, 2024.

8. Brice, M., "Installing the ATLAS Calorimeter", 2005, `https://cds.cern.ch/`

record/910381, accessed on April 8, 2024.

9. Schweizer, M., “View of the ALICE Detector With Its Magnet Doors Closed”, 2008, https://cds.cern.ch/record/1095672, accessed on April 8, 2024.

10. Toeroek, F.-L., “LHCb Experiment Visit”, 2021, https://cds.cern.ch/record/2791987, accessed on April 8, 2024.

11. “LHC the Guide FAQ”, 2021, https://press.cern/resources/brochure/knowledge-sharing/lhc-facts-and-figures, accessed on October 27, 2023.

12. Hertzog, S. J. and J. M. Ordan, “CMS During the Final Stages of LS2”, 2021, https://cds.cern.ch/record/2777919, accessed on April 8, 2024.

13. Sakuma, T. and T. McCauley, “Detector and Event Visualization With SketchUp at the CMS Experiment”, 2013, https://cds.cern.ch/record/1626816/?ln=en, accessed on April 23, 2024.

14. Barney, D., “CMS Detector Slice”, 2016, https://cds.cern.ch/record/2120661, accessed on October 27, 2023.

15. CMS Collaboration, “ECAL Technical Design Report (TDR) Figures from Chapter 1”, 1997, https://cds.cern.ch/record/1327662, accessed on April 26, 2024.

16. CMS Collaboration, “The CMS Experiment at the CERN LHC”, *Journal of Instrumentation*, Vol. 3, pp. 1–334, 2008.

17. Brice, M., “Insertion of the Positive Hadronic Barrel Calorimeter Inside the Inner Vacuum Tank”, 2006, https://cds.cern.ch/record/951470, accessed on April 23, 2024.

18. Abdullin, S. *et al.*, “Design, Performance, and Calibration of CMS Forward Calorimeter Wedges”, *The European Physical Journal C*, Vol. 53, pp. 139–166,

2008.

19. Cankoçak, K., M. Bakırcı, S. Çerçi, E. Gülmez, J. Merlo, Y. Onel, F. Özok, I. Schmidt and N. Sönmez, "Radiation-Hardness Measurements of High OH^- Content Quartz Fibres Irradiated with 24 GeV Protons up to 1.25 Grad", *Nuclear Instruments and Methods in Physics Research Section A*, Vol. 585, pp. 20–27, 2008.

20. "ROOT, Data Analysis Framework", `https://root.cern/`, accessed on October 27, 2023.

APPENDIX A: NORMALIZED RATIO PLOTS FOR ALL IETA AND IPHI VALUES WITH RESPECT TO TIME

Normalized ratio plots for all iEta and iPhi values with respect to time are given below.

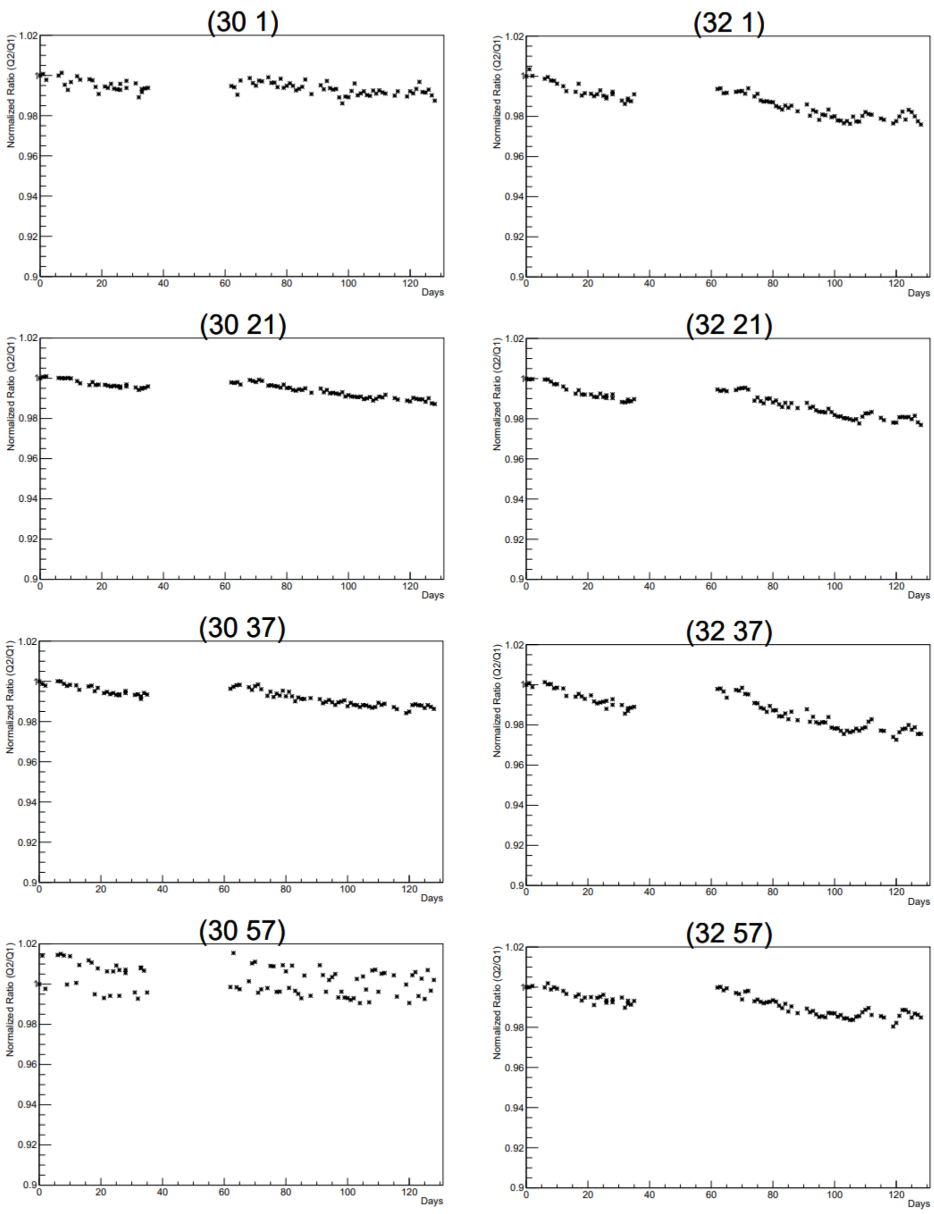

Figure A.1. Graphs of normalized ratio with respect to time for all (iEta iPhi) values.

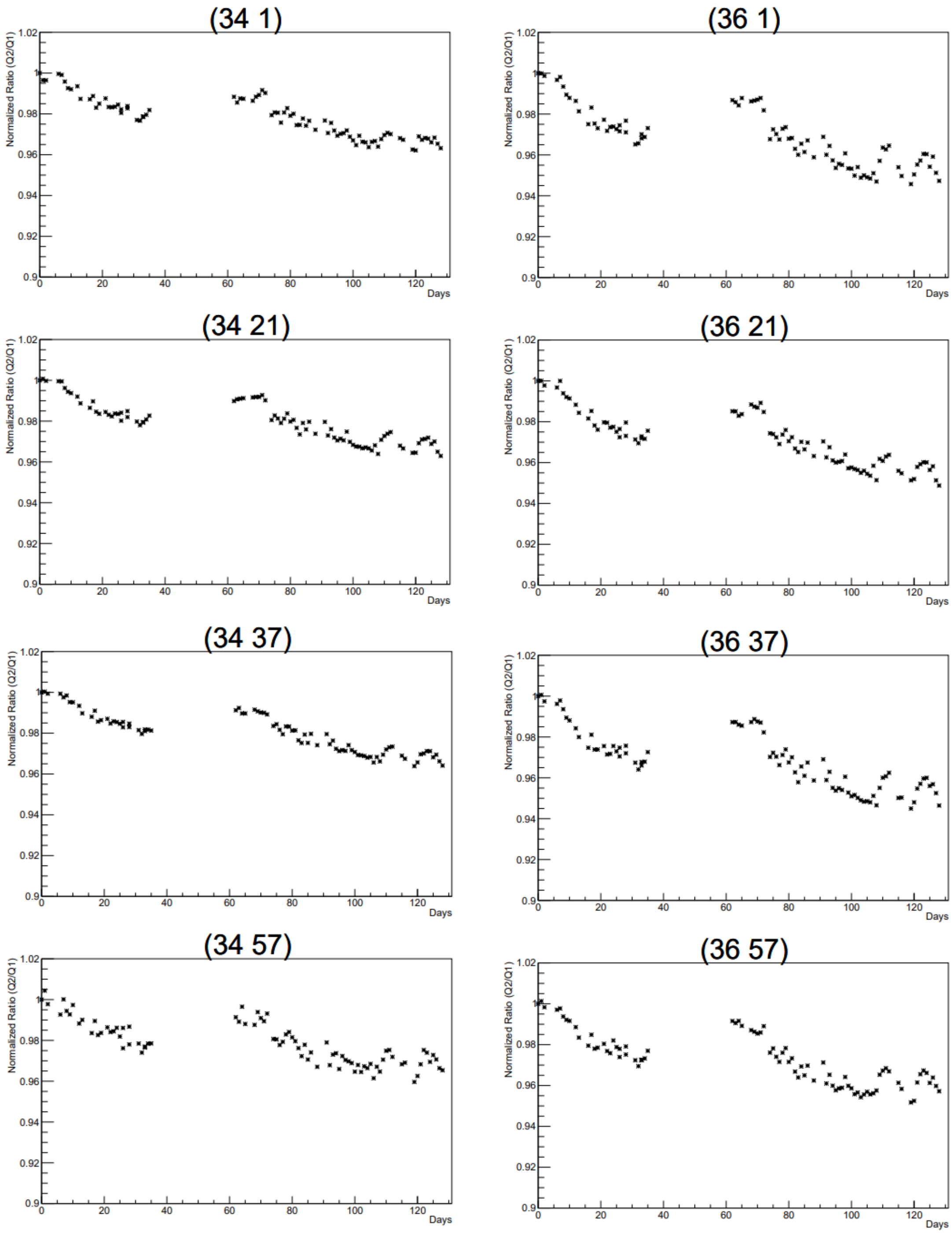

Figure A.1. Graphs of normalized ratio with respect to time for all (iEta iPhi) values. (cont.)

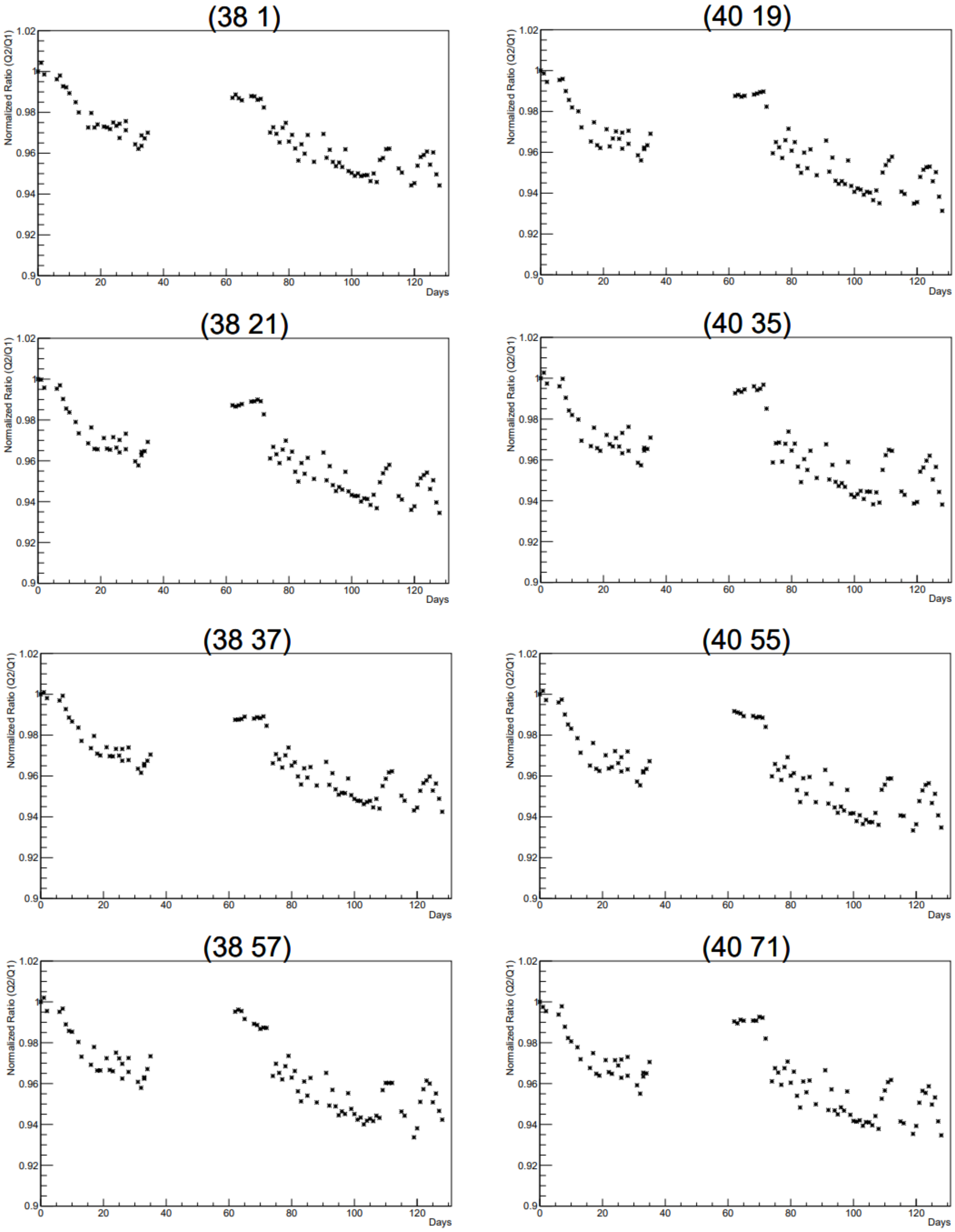

Figure A.1. Graphs of normalized ratio with respect to time for all (iEta iPhi) values. (cont.)

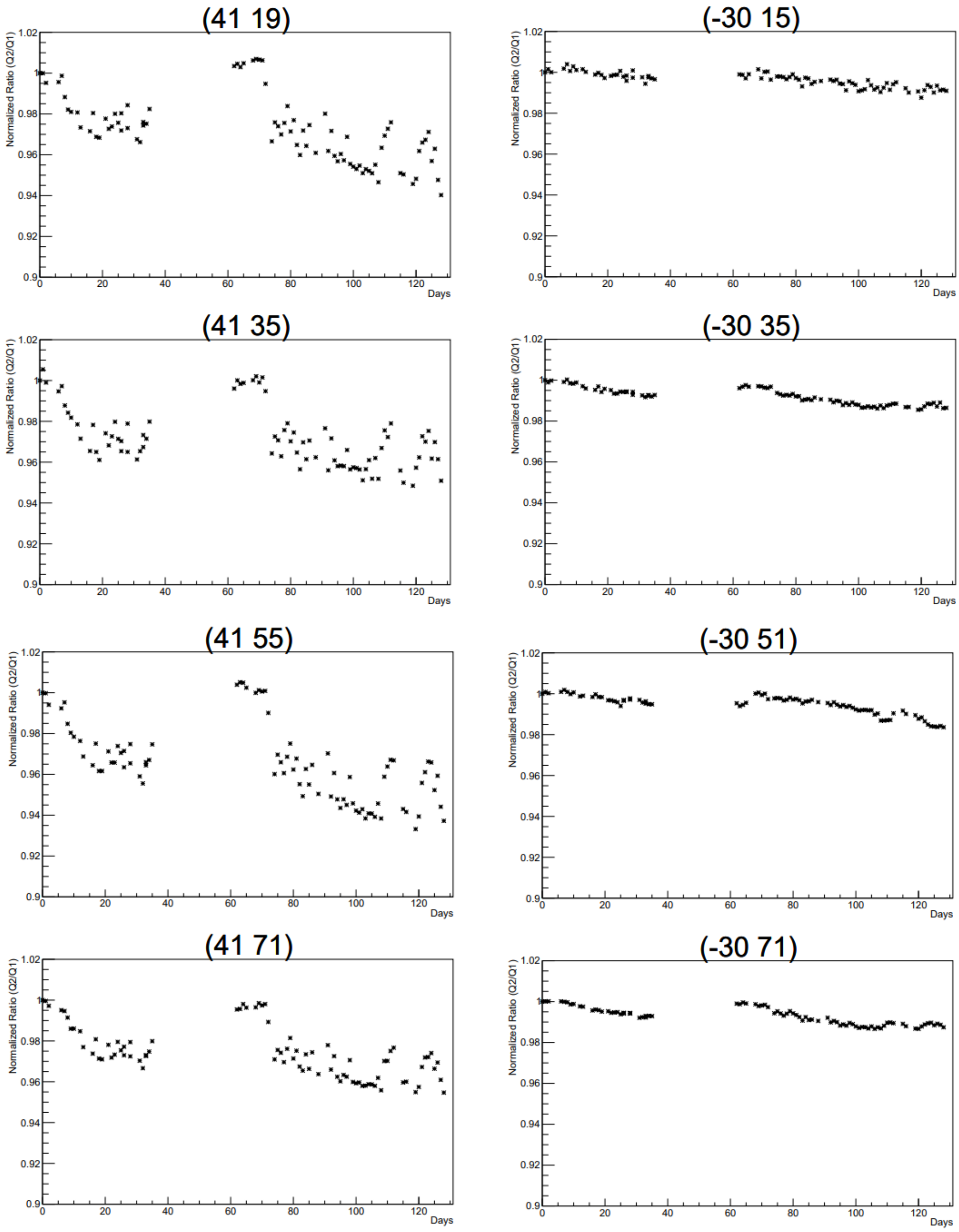

Figure A.1. Graphs of normalized ratio with respect to time for all (iEta iPhi) values. (cont.)

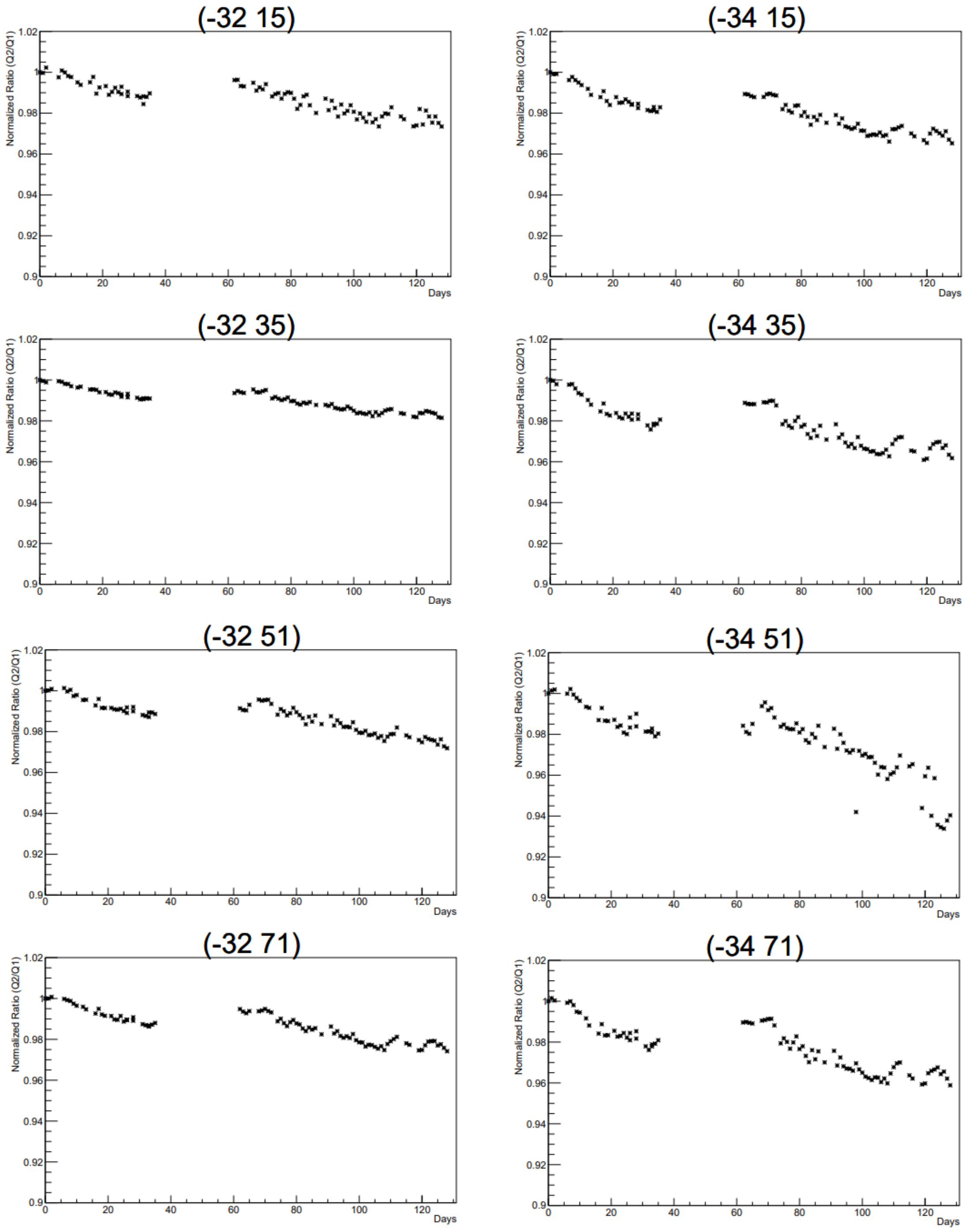

Figure A.1. Graphs of normalized ratio with respect to time for all (iEta iPhi) values. (cont.)

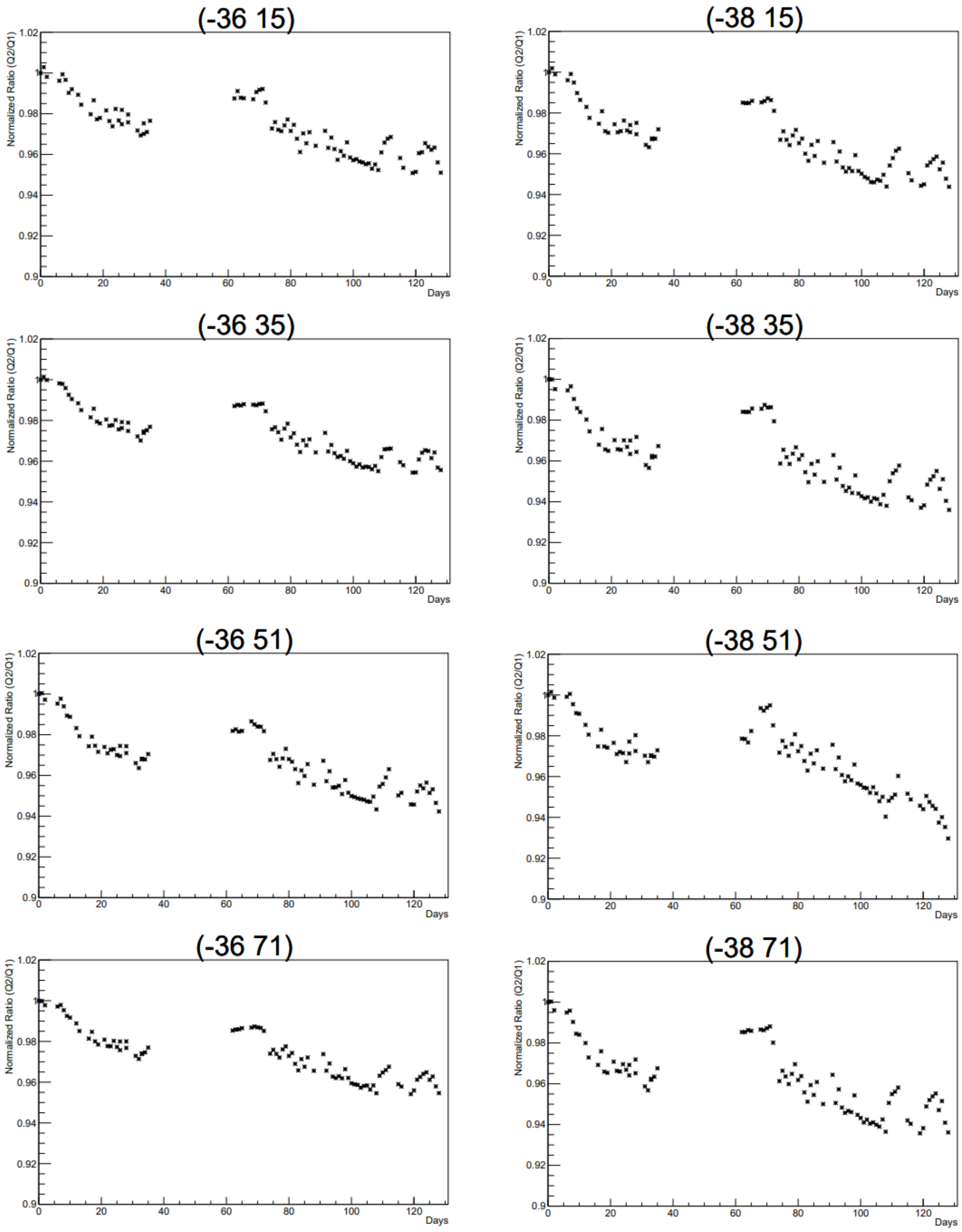

Figure A.1. Graphs of normalized ratio with respect to time for all (iEta iPhi) values. (cont.)

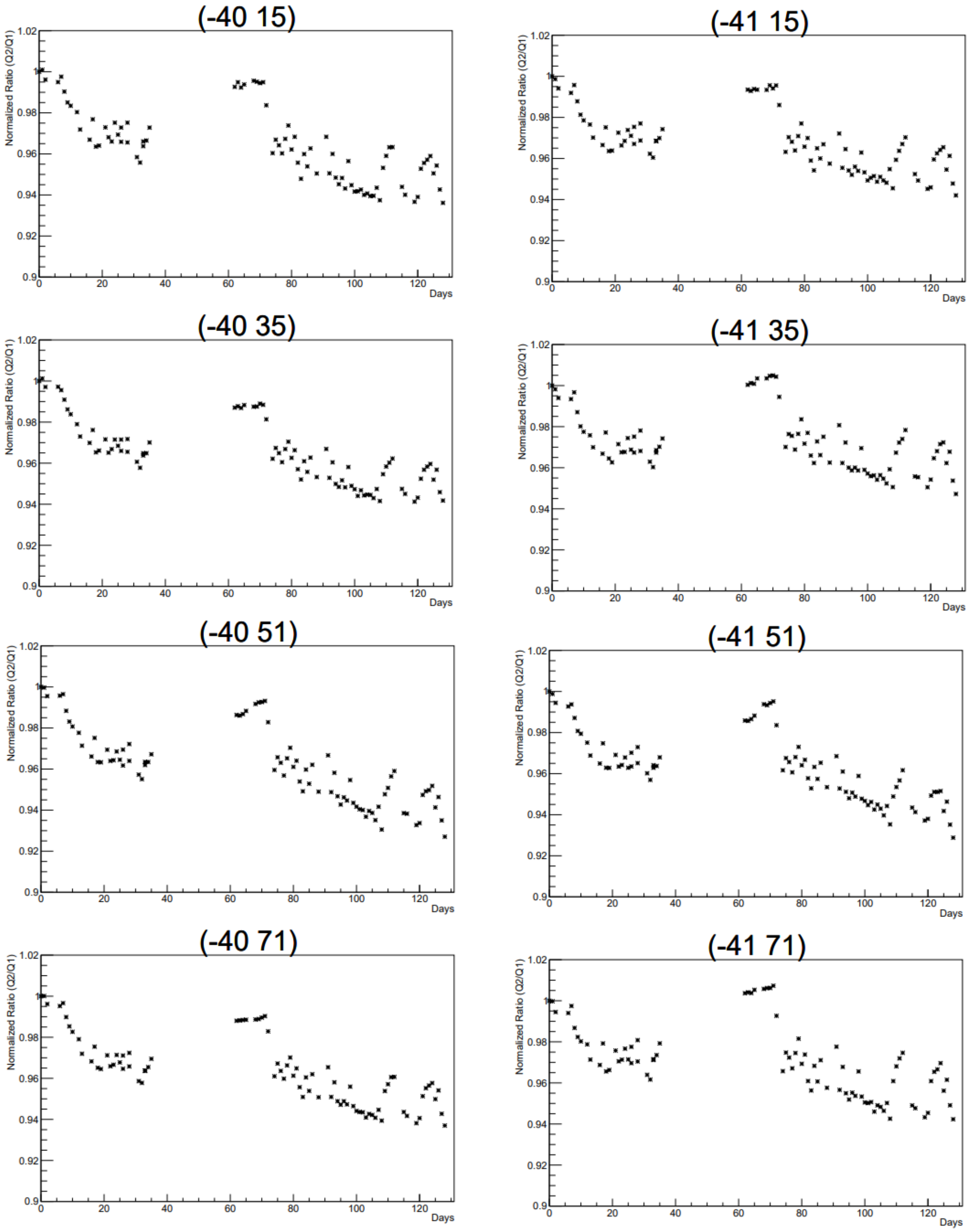

Figure A.1. Graphs of normalized ratio with respect to time for all (iEta iPhi) values. (cont.)

APPENDIX B: NORMALIZED RATIO PLOTS FOR ALL IETA AND IPHI VALUES WITH RESPECT TO INTEGRATED LUMINOSITY

Normalized ratio plots for all iEta and iPhi values with respect to integrated luminosity are given below.

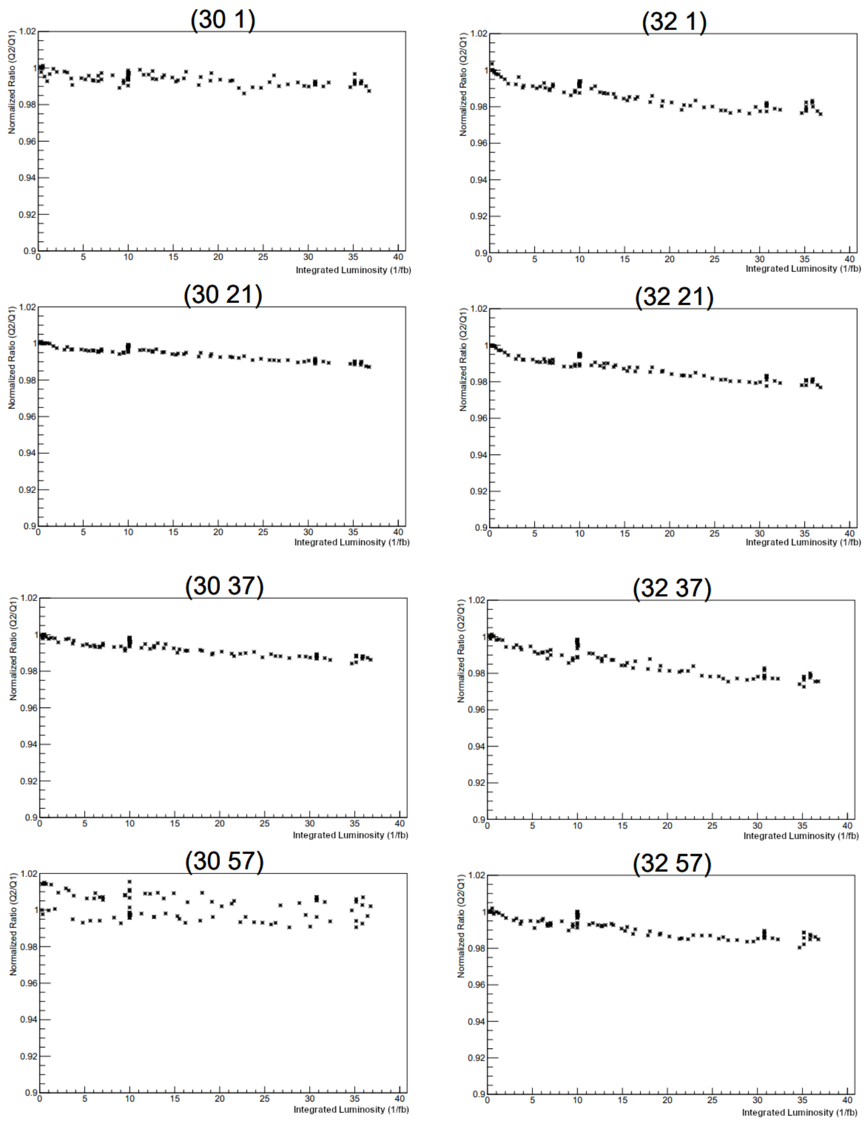

Figure B.1. Graphs of normalized ratio with respect to integrated luminosity for all (iEta iPhi) values.

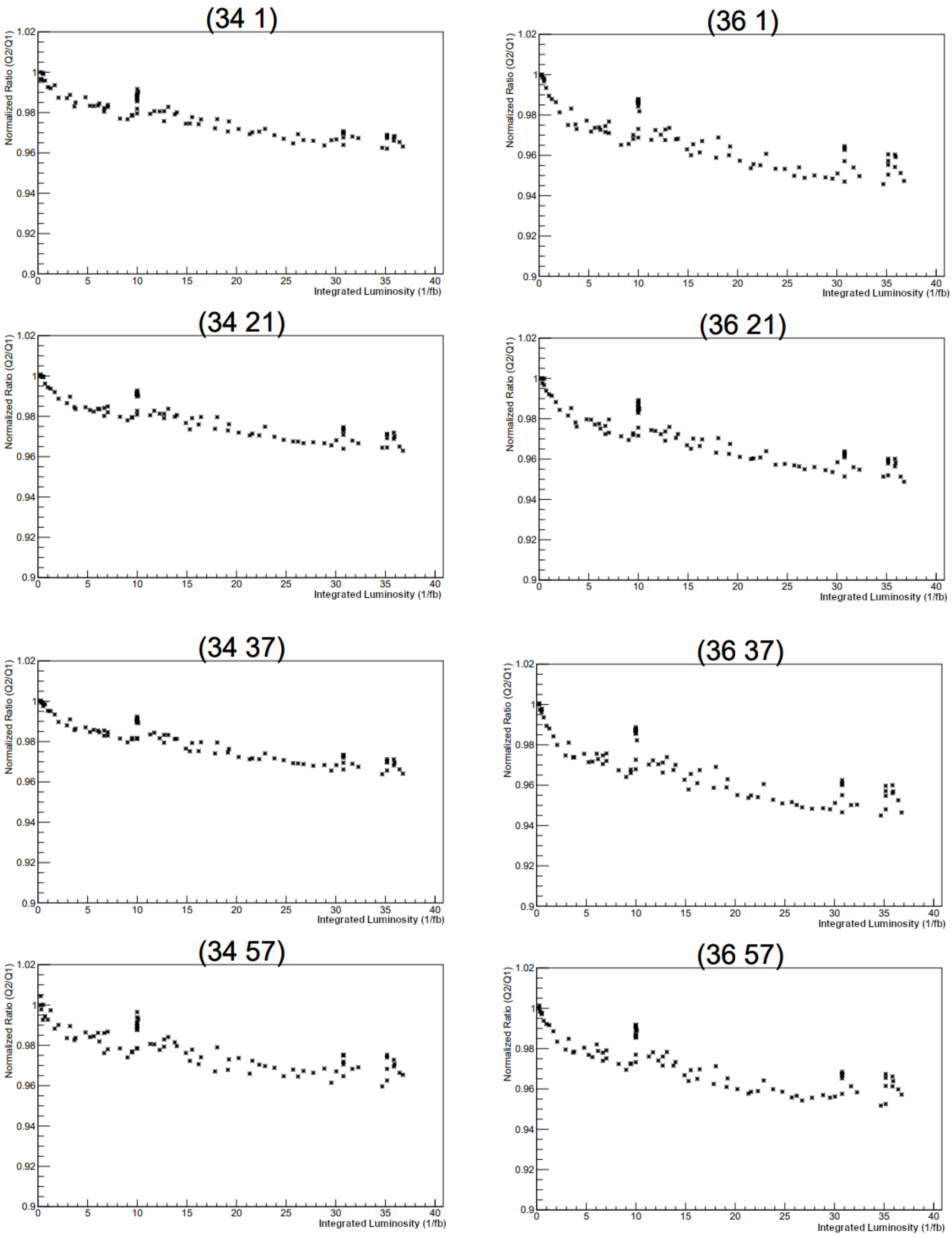

Figure B.1. Graphs of normalized ratio with respect to integrated luminosity for all (iEta iPhi) values. (cont.)

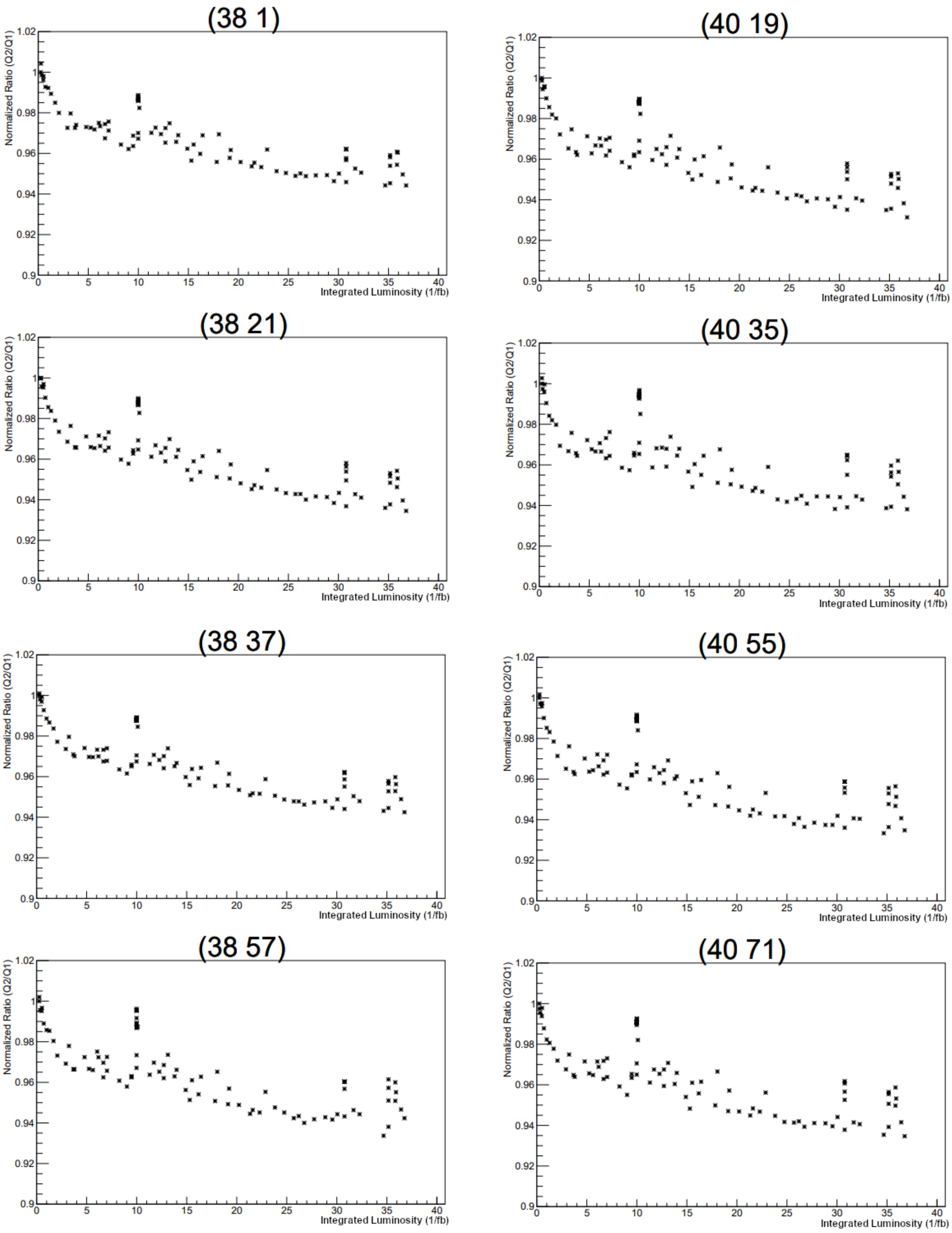

Figure B.1. Graphs of normalized ratio with respect to integrated luminosity for all (iEta iPhi) values. (cont.)

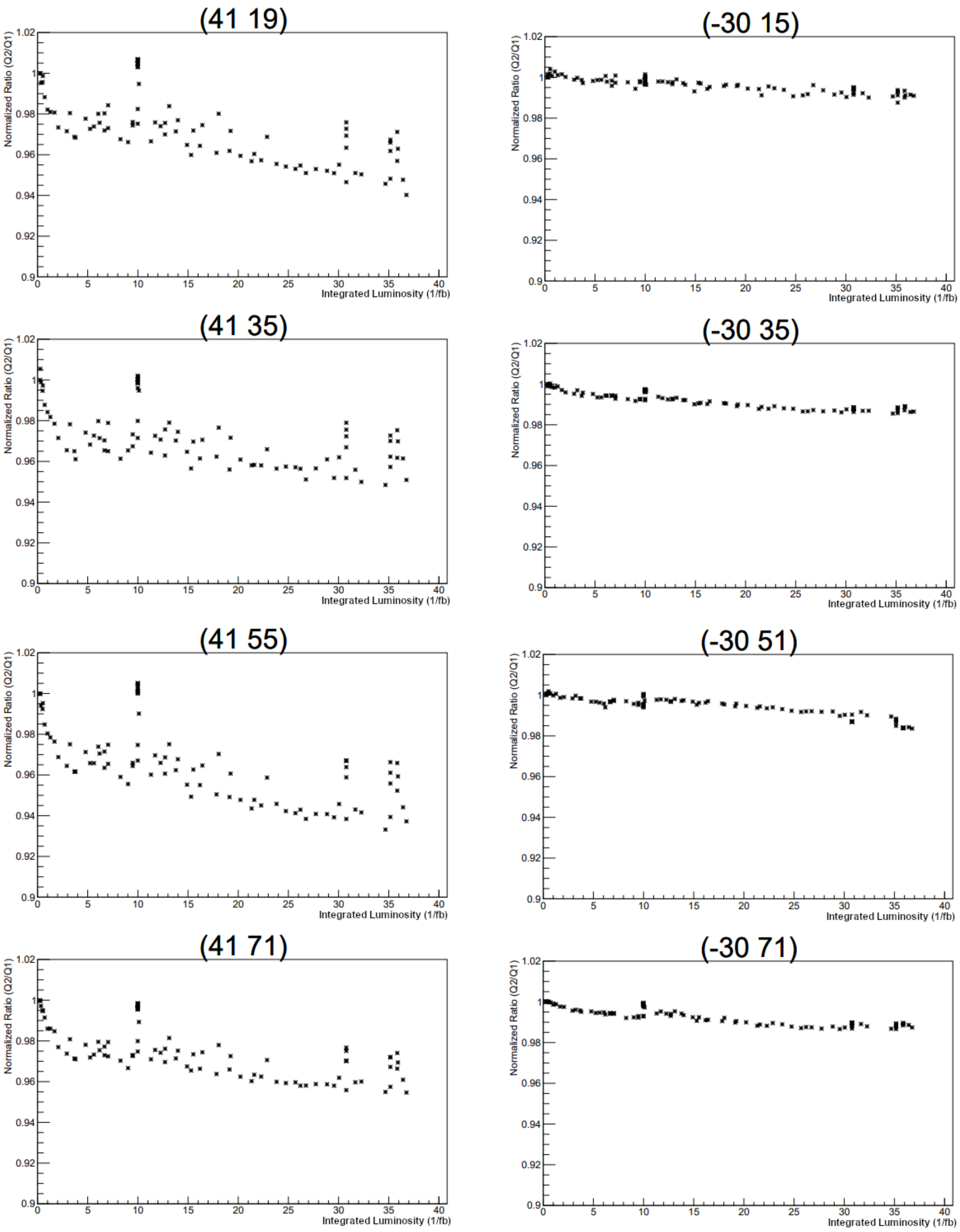

Figure B.1. Graphs of normalized ratio with respect to integrated luminosity for all (iEta iPhi) values. (cont.)

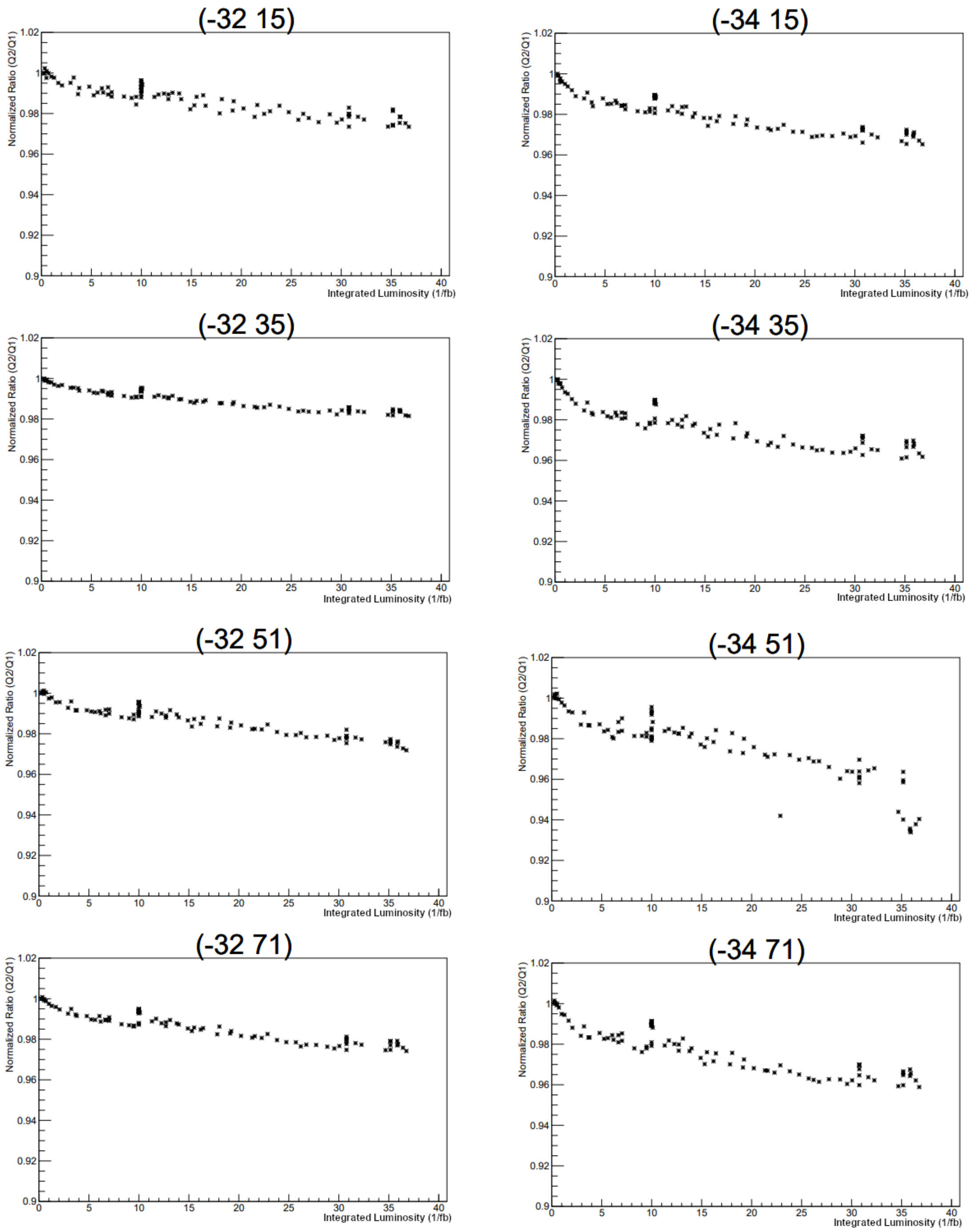

Figure B.1. Graphs of normalized ratio with respect to integrated luminosity for all (iEta iPhi) values. (cont.)

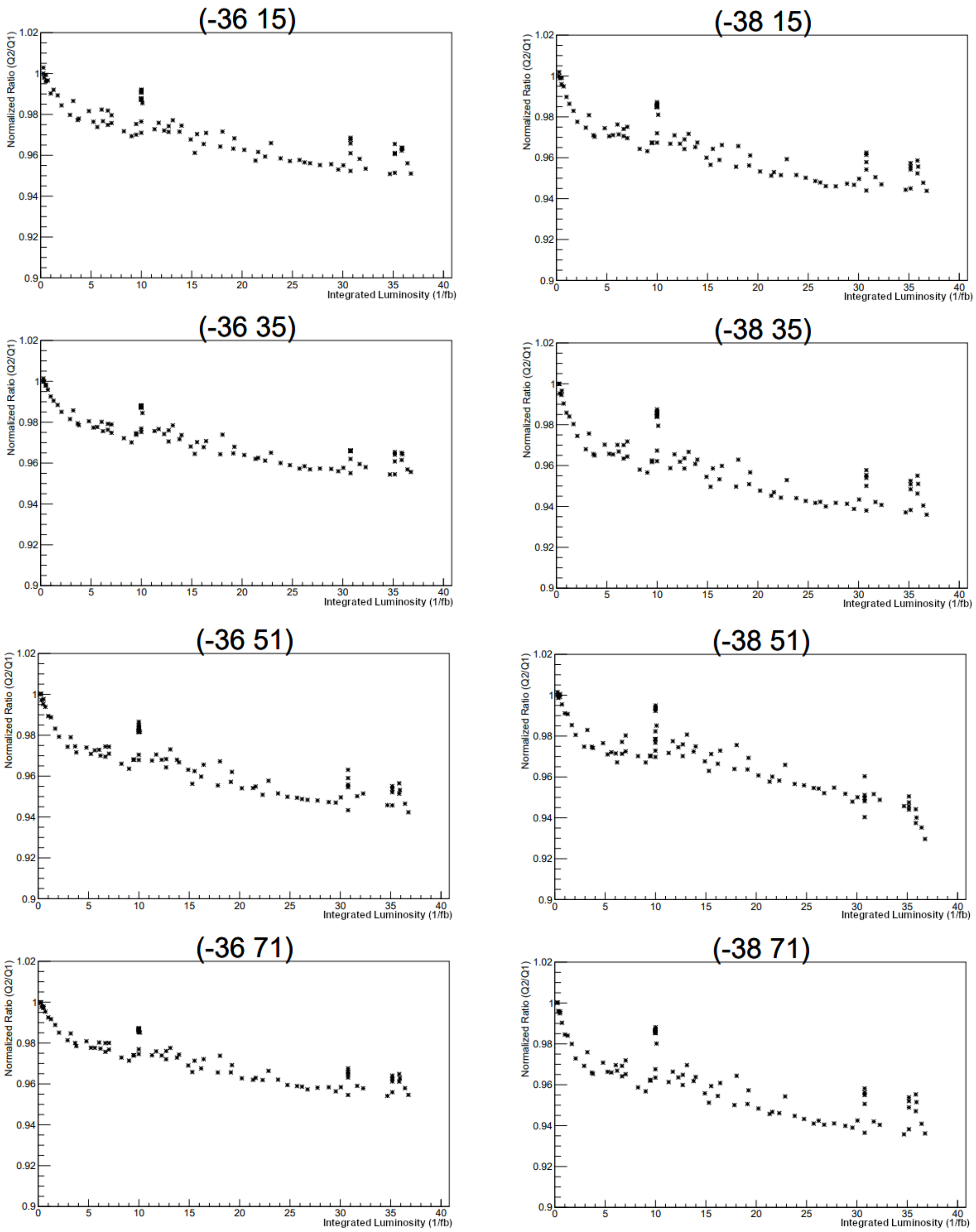

Figure B.1. Graphs of normalized ratio with respect to integrated luminosity for all (iEta iPhi) values. (cont.)

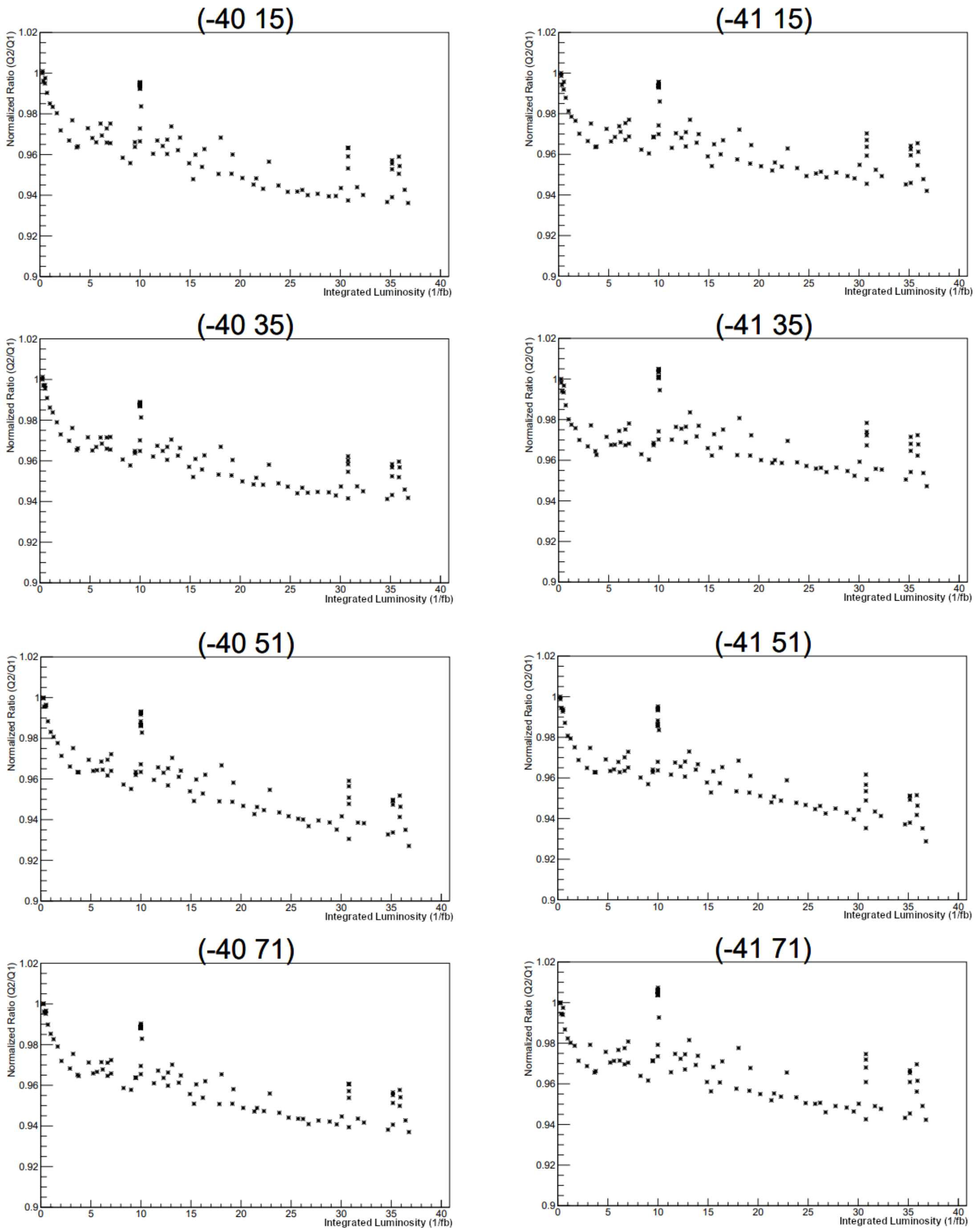

Figure B.1. Graphs of normalized ratio with respect to integrated luminosity for all (iEta iPhi) values. (cont.)

APPENDIX C: NORMALIZED RATIO PLOTS AVERAGED OVER IPHI FOR ALL IETA VALUES

Normalized ratio plots averaged over iPhi for all iEta values are given below.

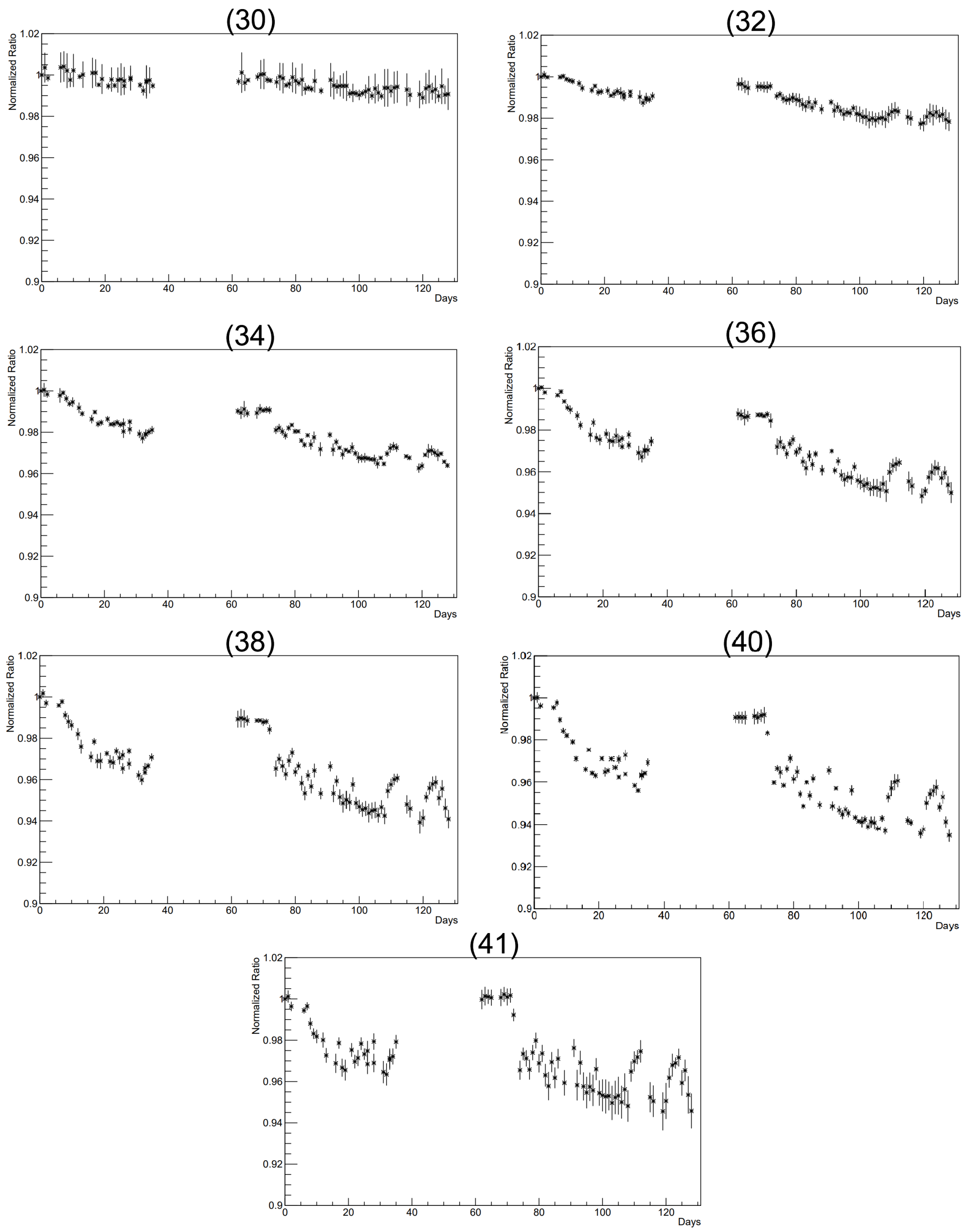

Figure C.1. Graphs of normalized ratio with respect to time averaged over iPhi for all positive iEta values.

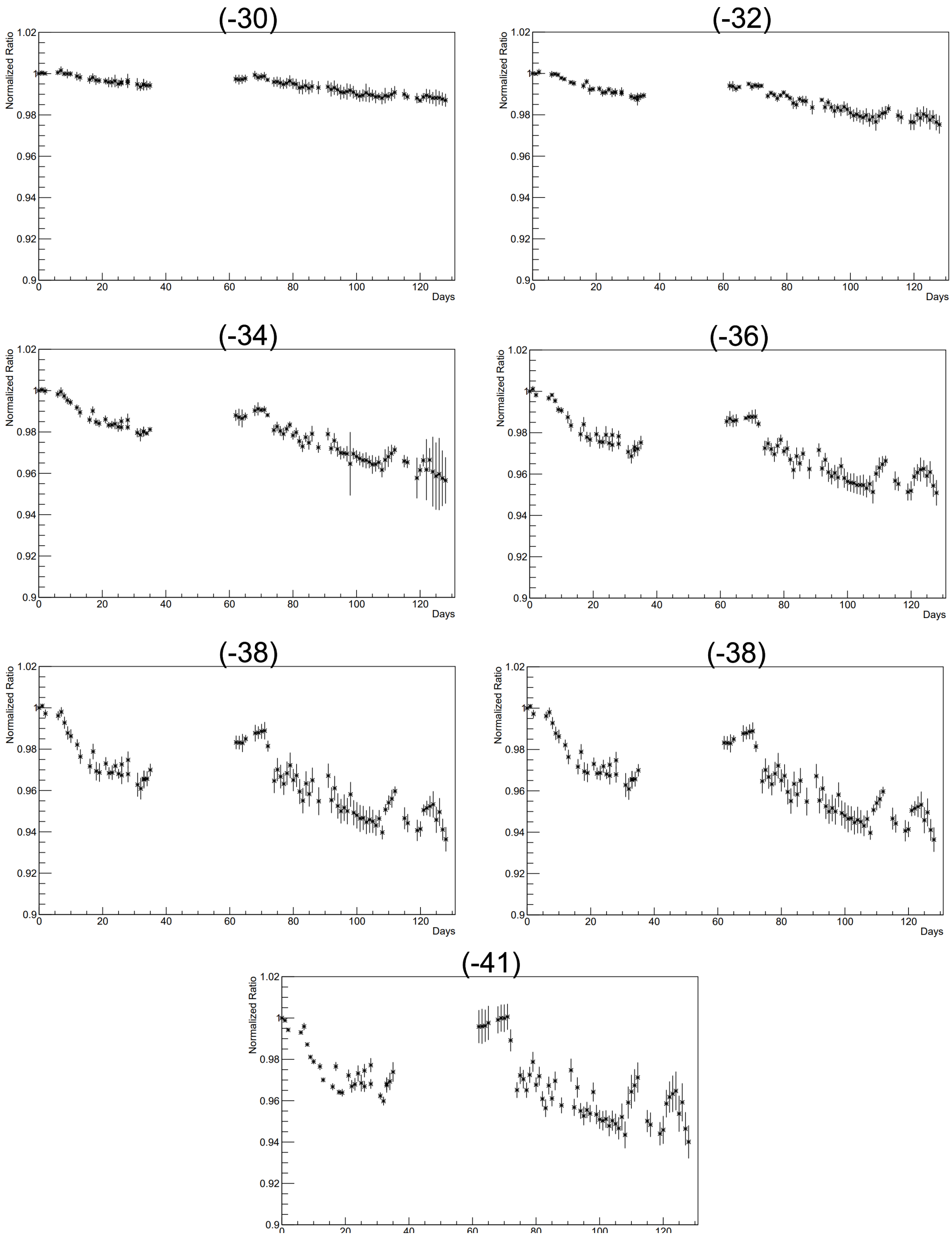

Figure C.2. Graphs of normalized ratio with respect to time averaged over iPhi for all negative iEta values.

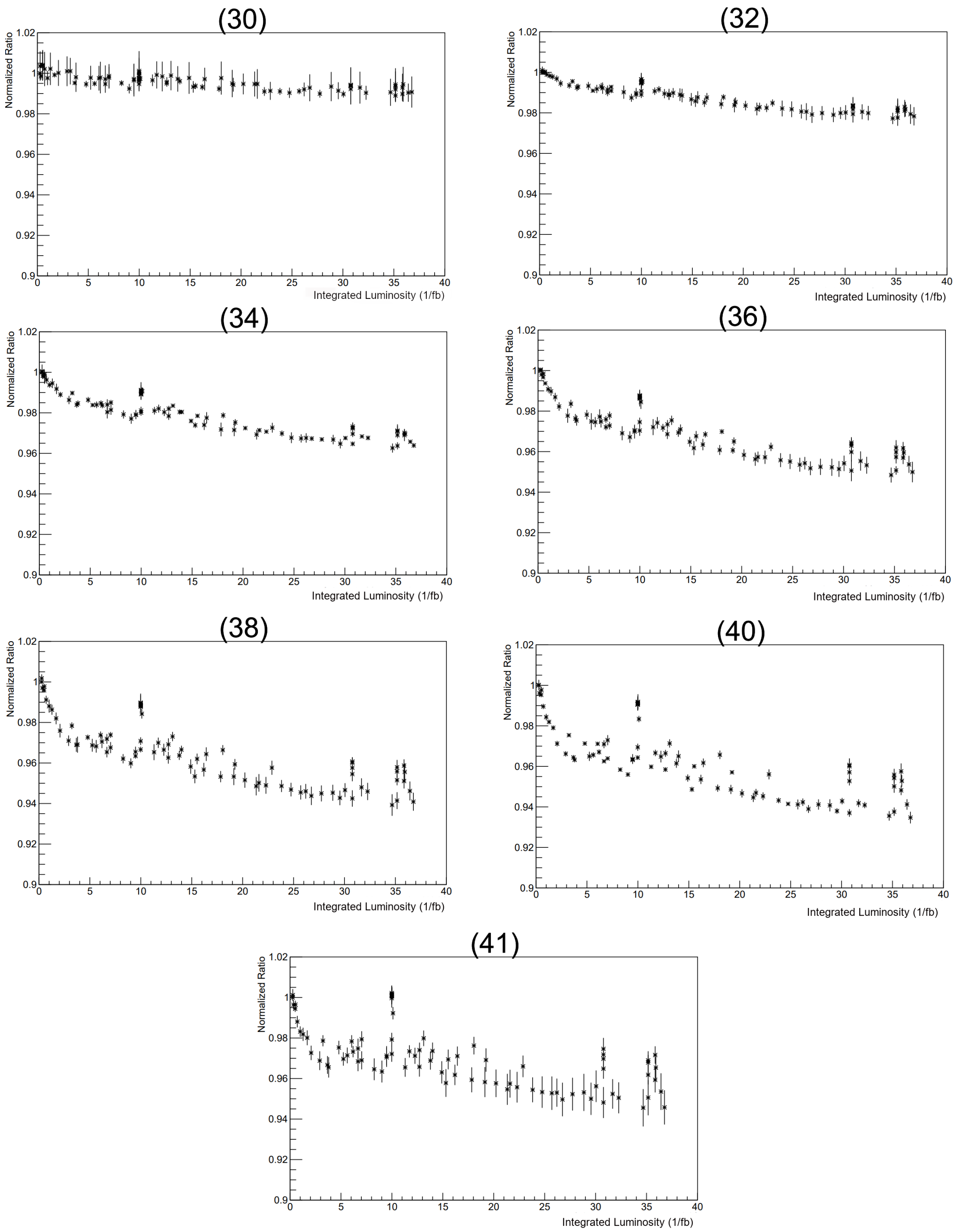

Figure C.3. Graphs of normalized ratio with respect to integrated luminosity averaged over iPhi for all positive iEta values.

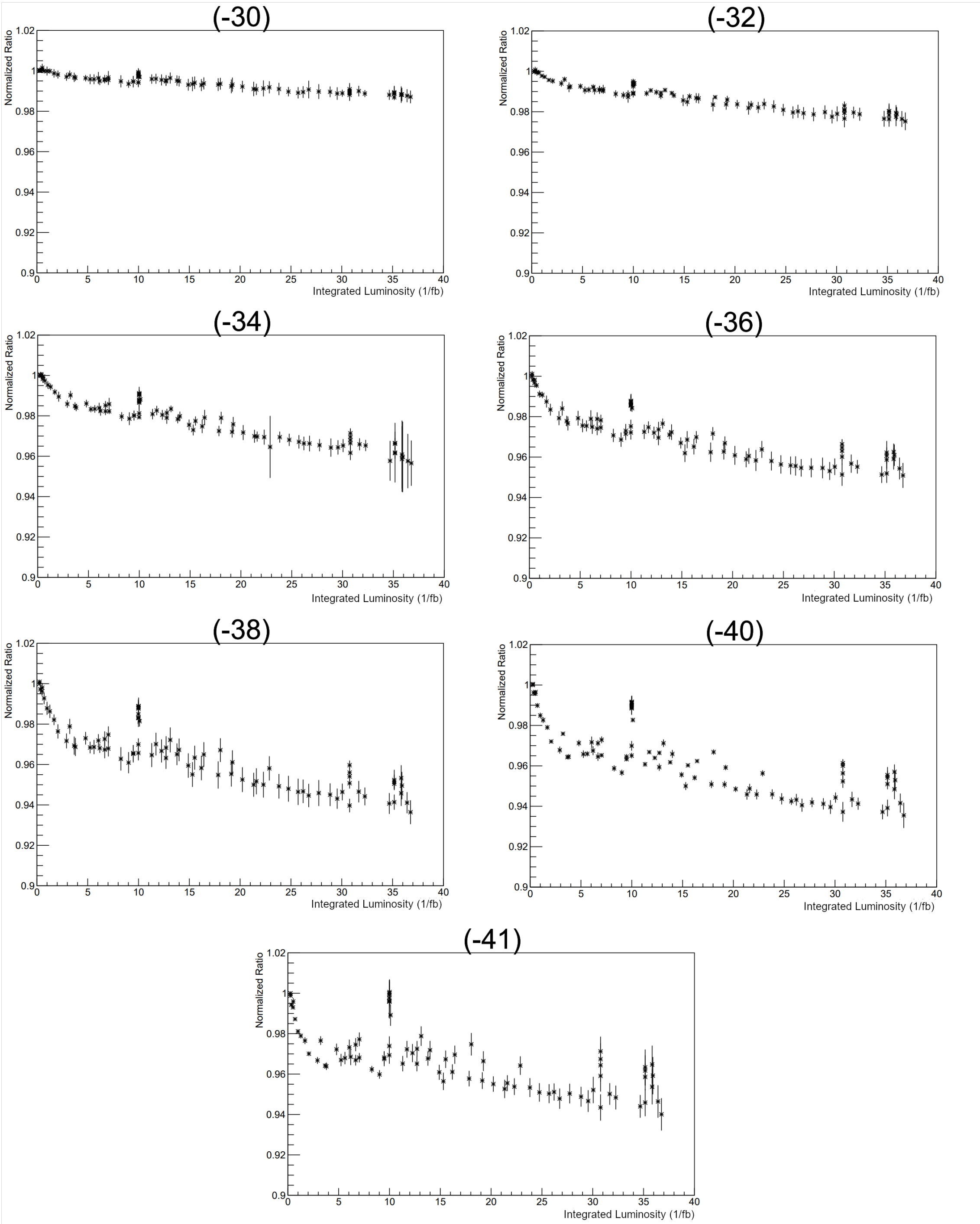

Figure C.4. Graphs of normalized ratio with respect to integrated luminosity averaged over iPhi for all negative iEta values.

APPENDIX D: NORMALIZED RATIO PLOTS AVERAGED OVER IPHI FOR ALL IETA VALUES FOR RUNS IN LESS THAN ONE HOUR AFTER COLLISION

Normalized ratio plots averaged over iPhi for all iEta values for runs in less than one hour after collision are given below.

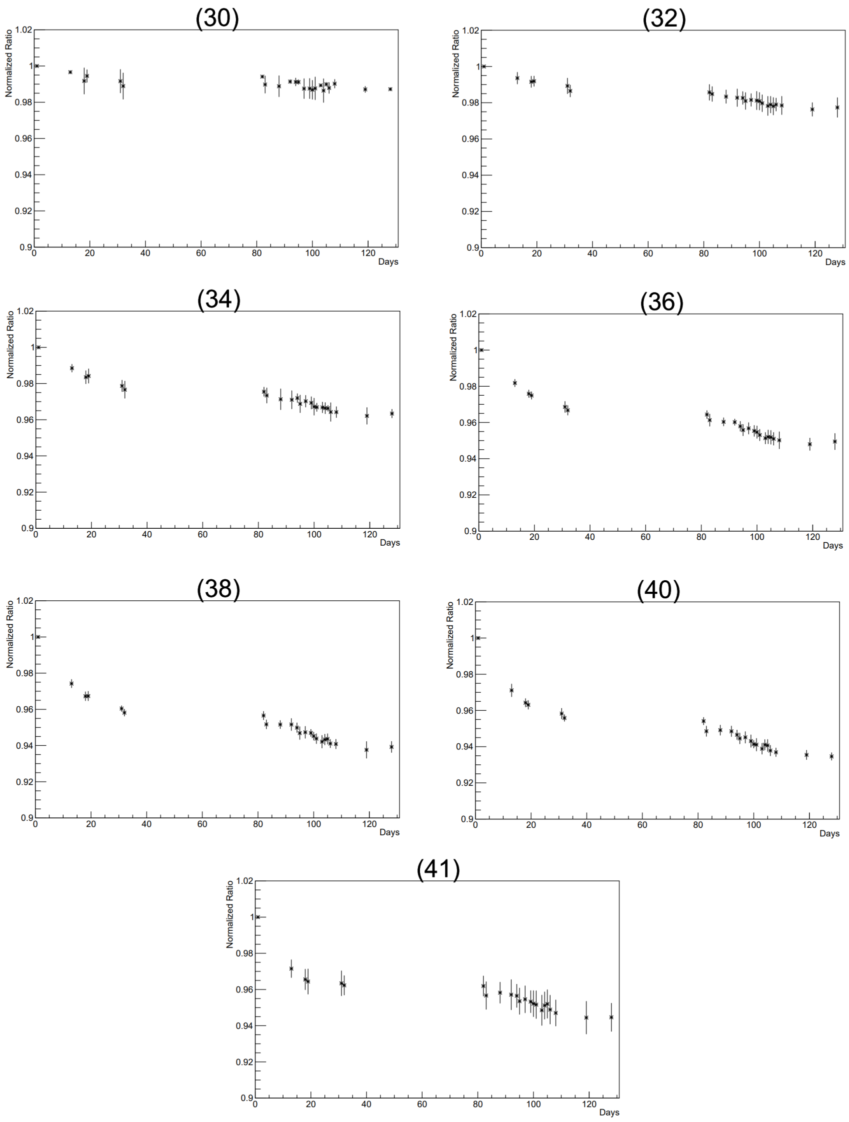

Figure D.1. Graphs of normalized ratio with respect to time averaged over iPhi for all positive iEta values for the runs which took place in less than 1 hour after the nearest collision.

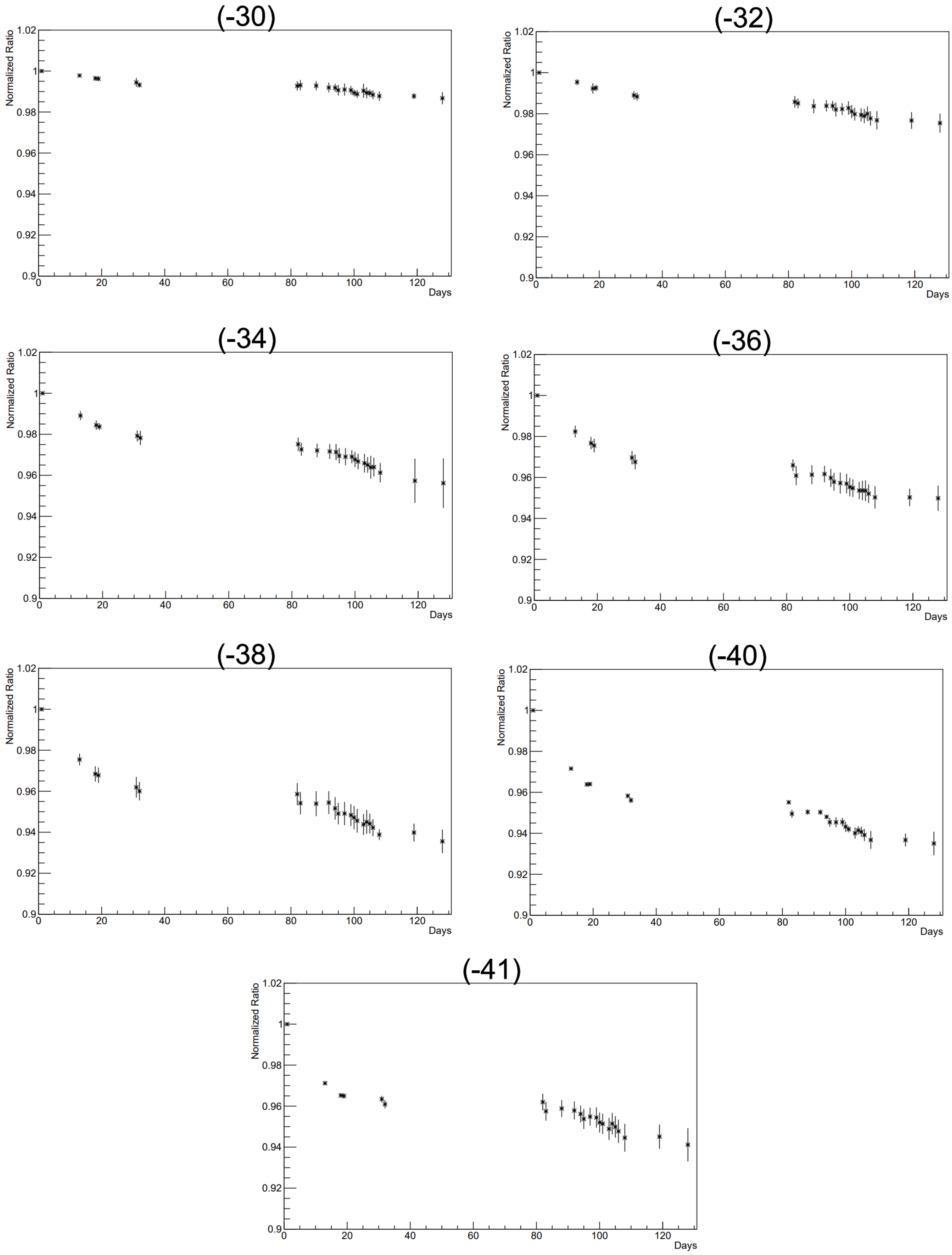

Figure D.2. Graphs of normalized ratio with respect to time averaged over iPhi for all negative iEta values for the runs which took place in less than 1 hour after the nearest collision.

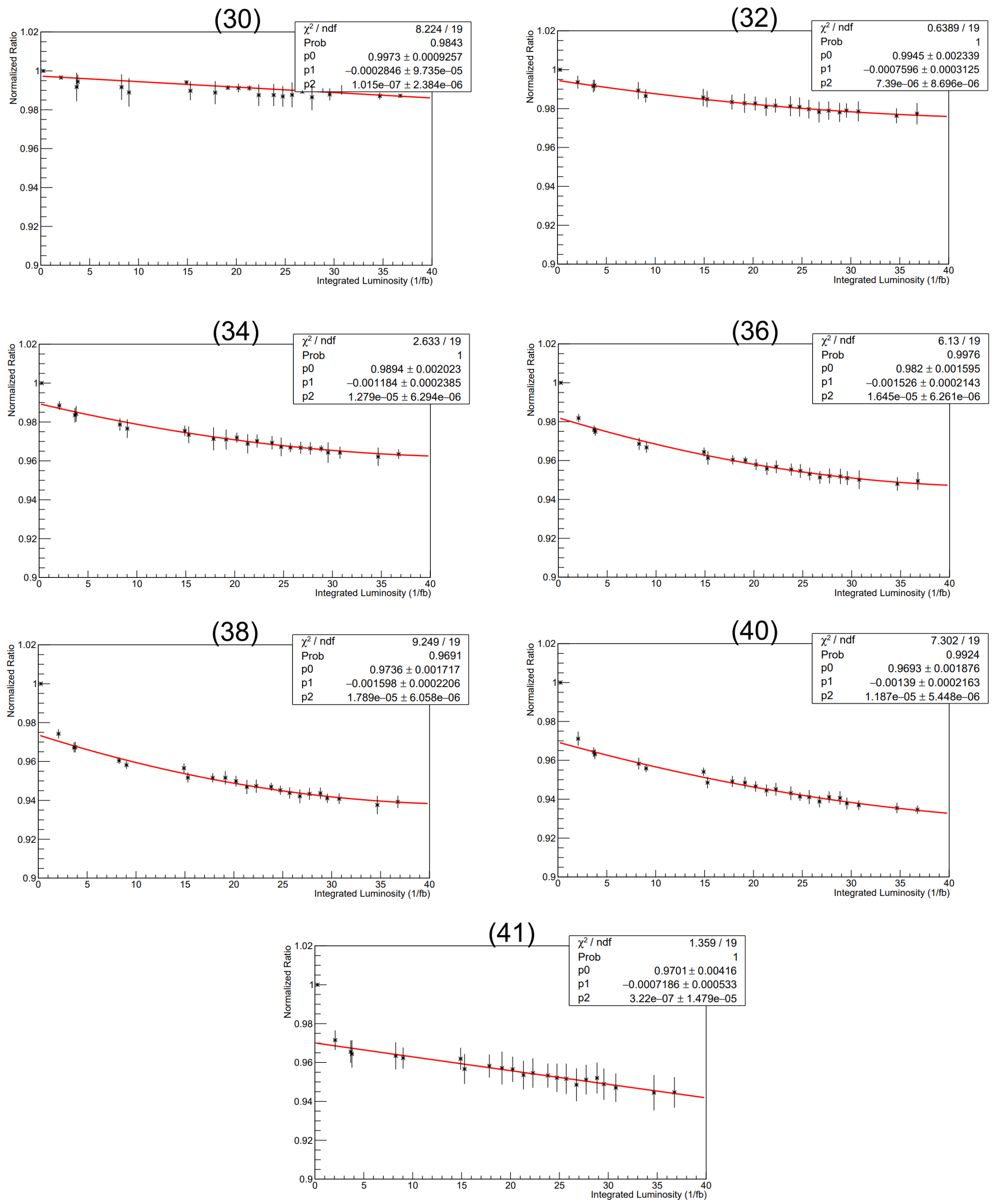

Figure D.3. Graphs of normalized ratio with respect to integrated luminosity averaged over iPhi for all positive iEta values for the runs which took place in less than 1 hour after the nearest collision (with quadratic fit).

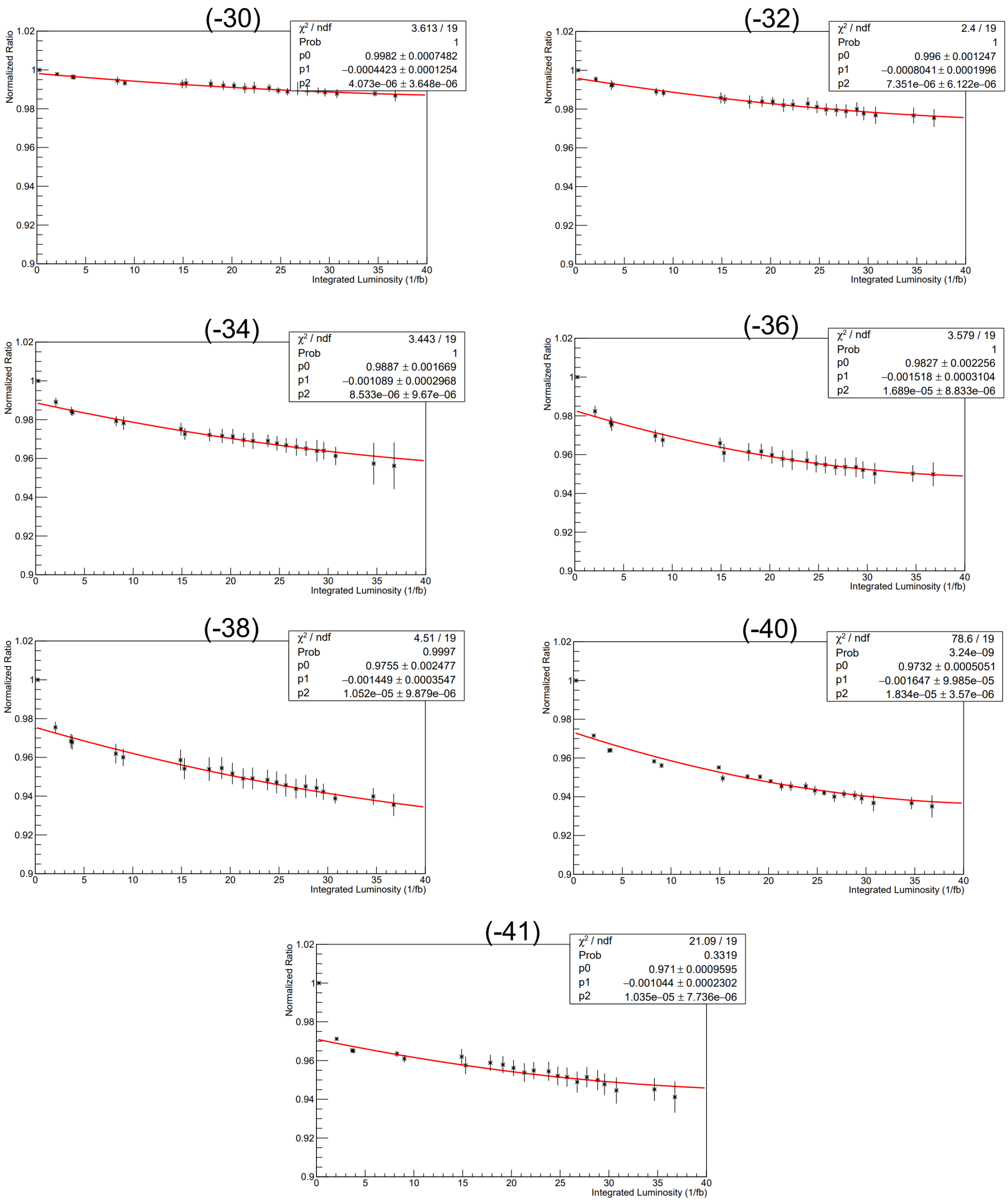

Figure D.4. Graphs of normalized ratio with respect to integrated luminosity averaged over iPhi for all negative iEta values for the runs which took place in less than 1 hour after the nearest collision (with quadratic fit).

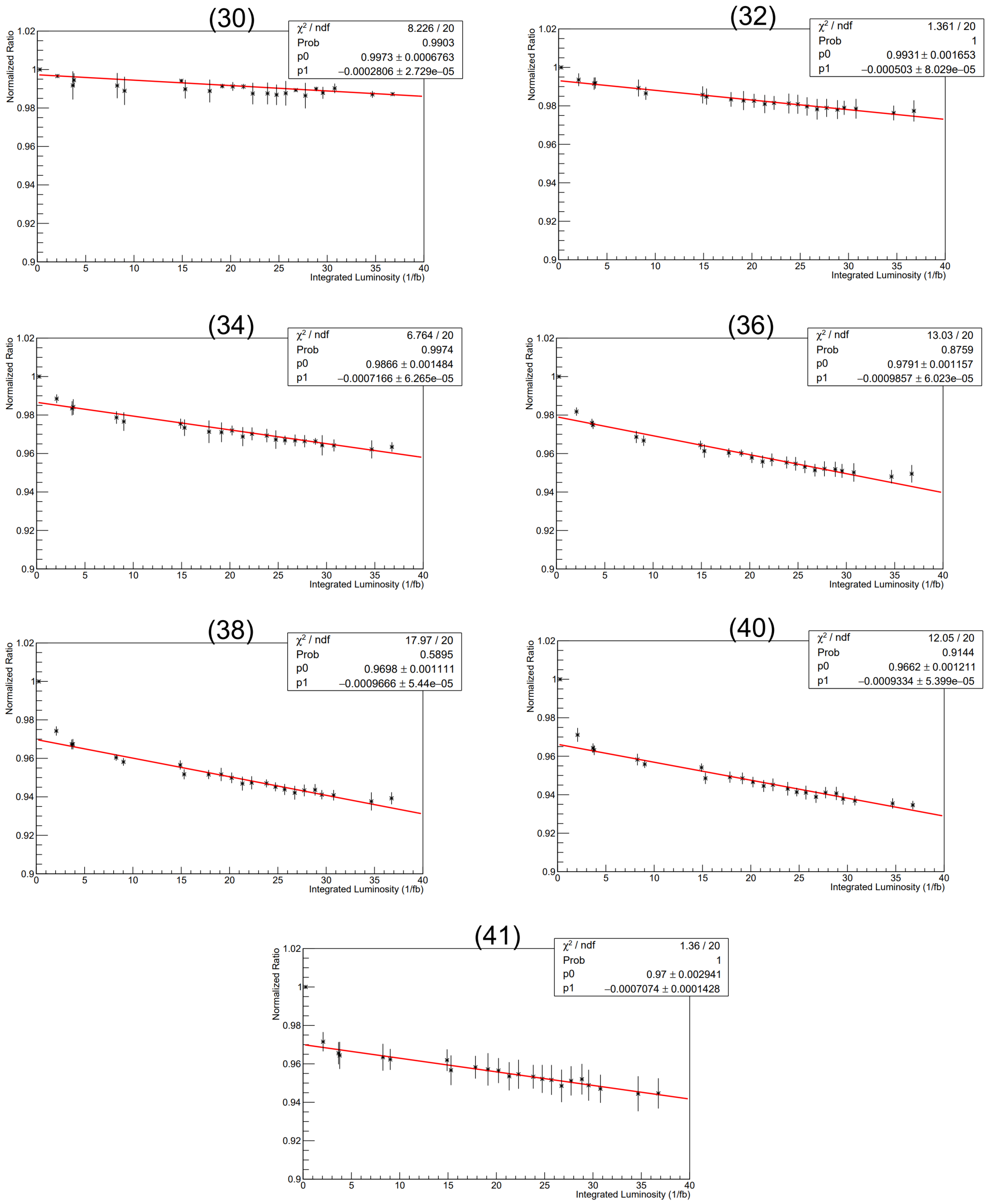

Figure D.5. Graphs of normalized ratio with respect to integrated luminosity averaged over iPhi for all positive iEta values for the runs which took place in less than 1 hour after the nearest collision (with linear fit).

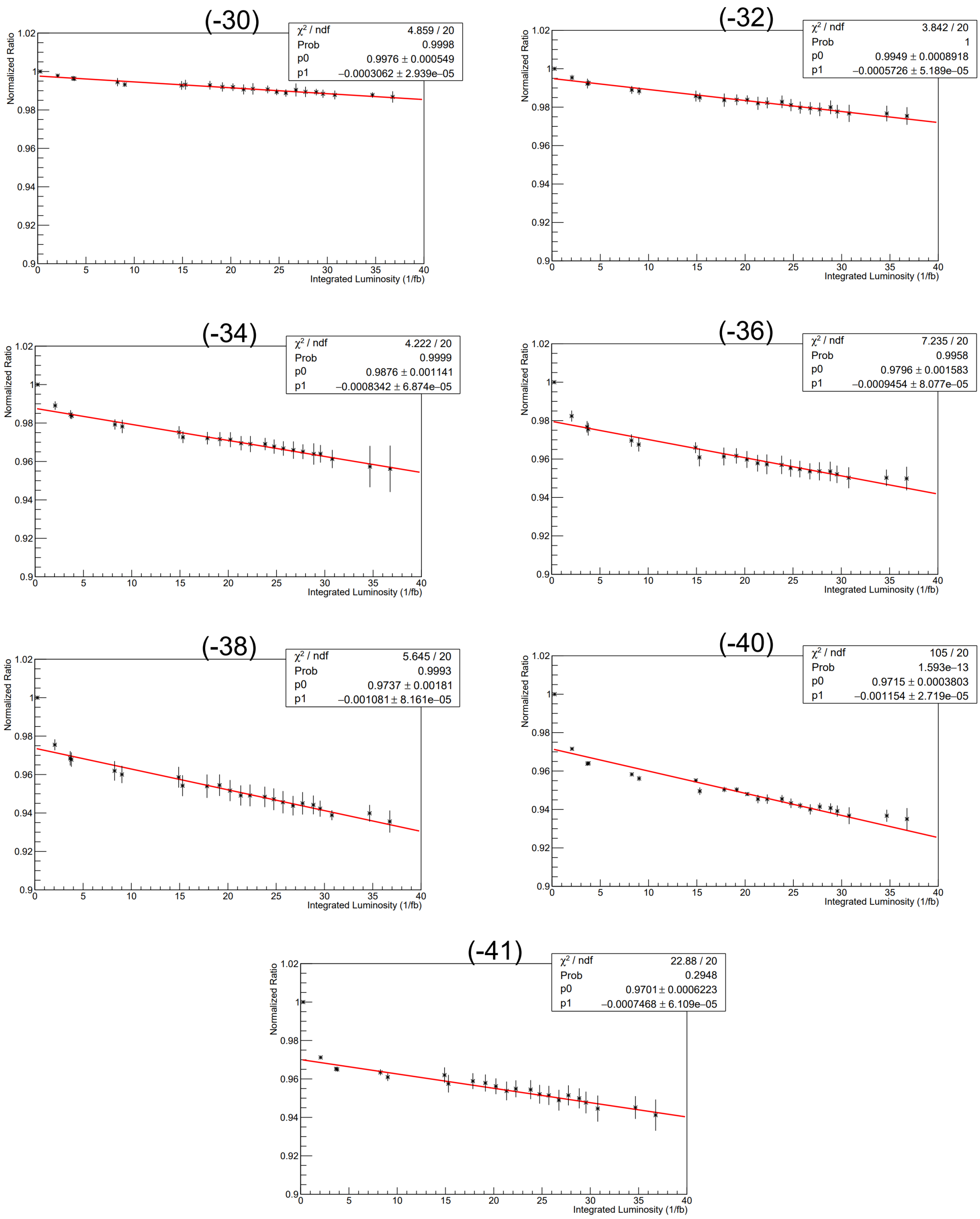

Figure D.6. Graphs of normalized ratio with respect to integrated luminosity averaged over iPhi for all negative iEta values for the runs which took place in less than 1 hour after the nearest collision (with linear fit).

APPENDIX E: DOUBLY NORMALIZED RATIO PLOTS AVERAGED OVER IPHI FOR ALL IETA VALUES

Doubly normalized ratio plots averaged over iPhi for all iEta values are given below.

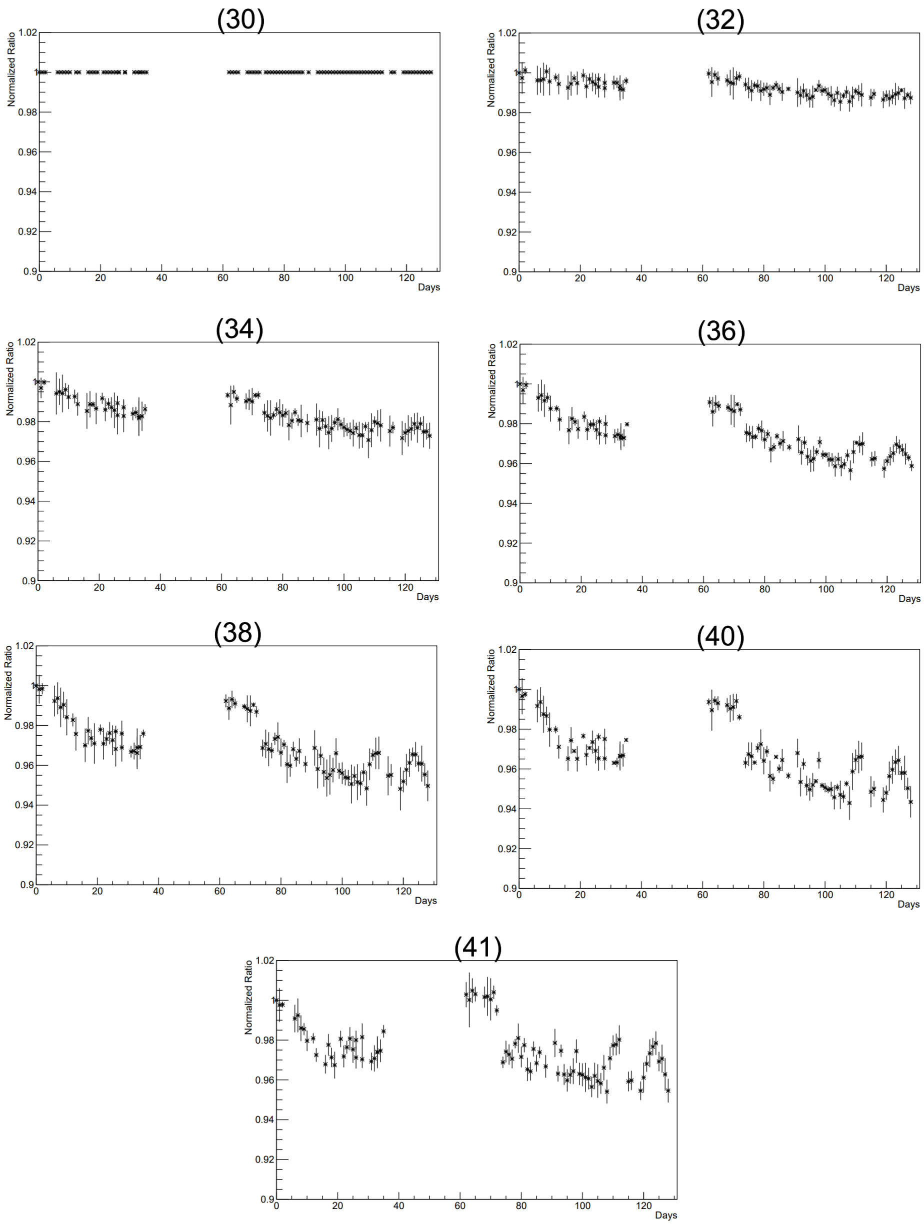

Figure E.1. Graphs of doubly normalized ratio with respect to time averaged over iPhi for all positive iEta values.

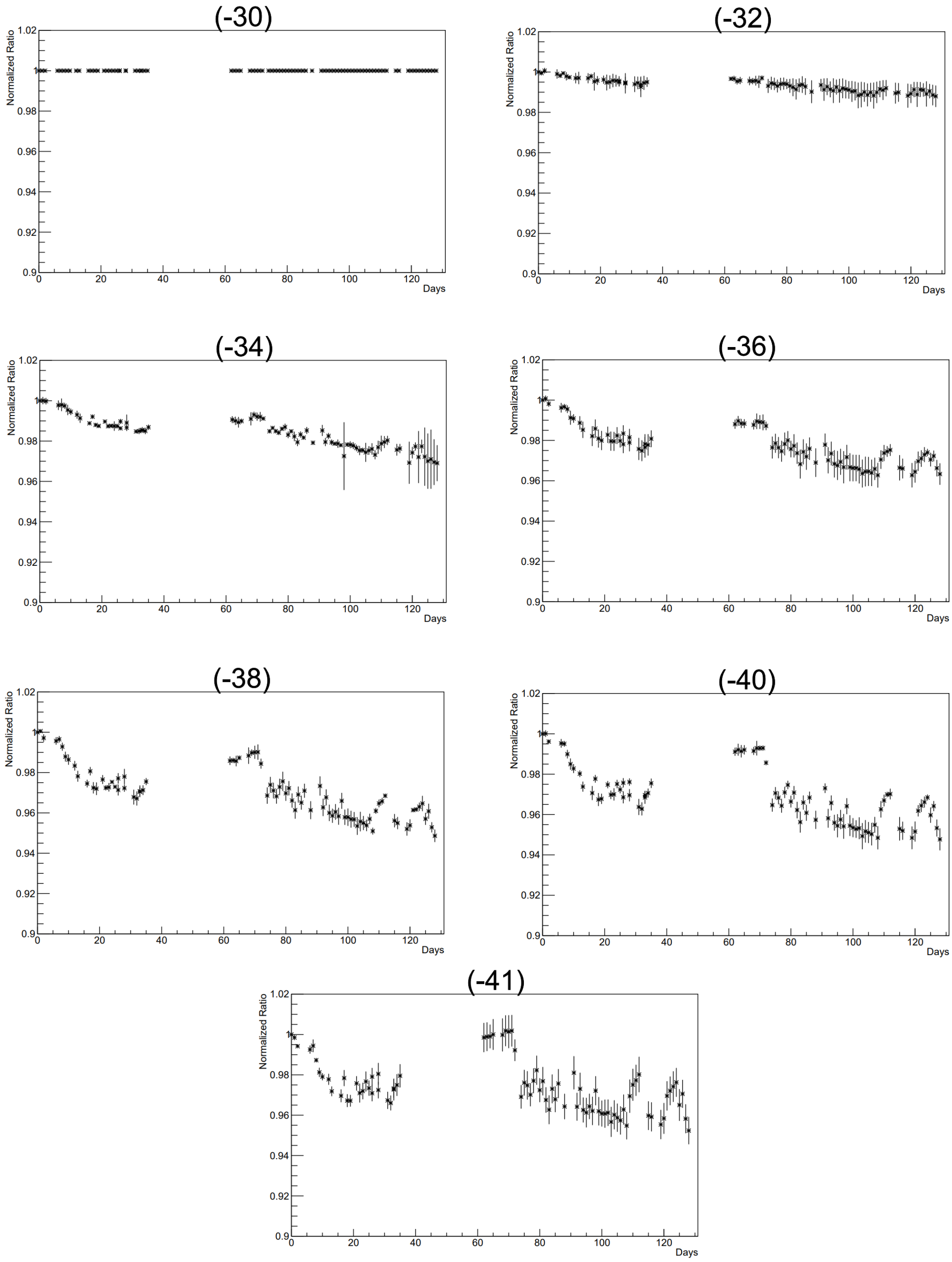

Figure E.2. Graphs of doubly normalized ratio with respect to time averaged over iPhi for all negative iEta values.

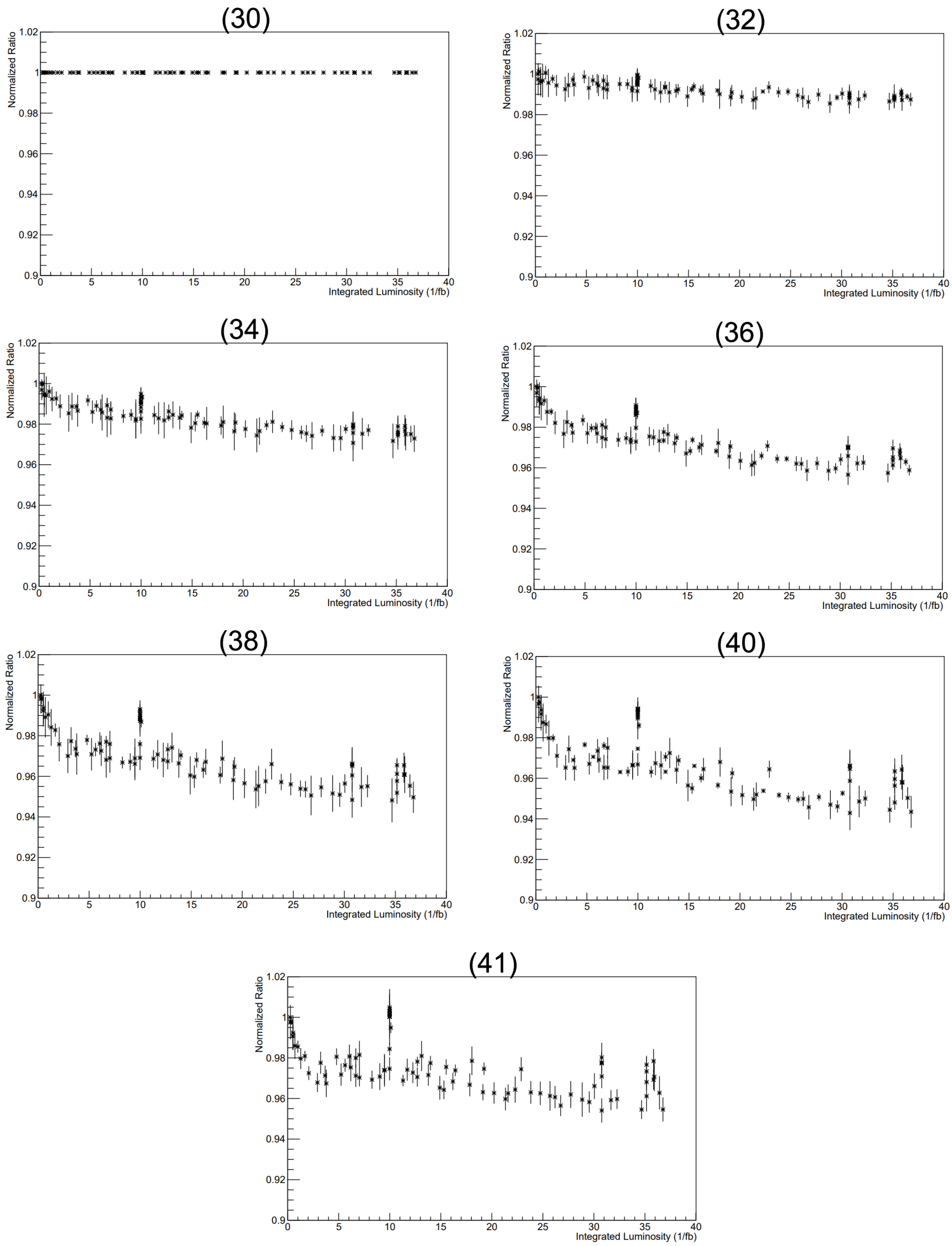

Figure E.3. Graphs of doubly normalized ratio with respect to integrated luminosity averaged over iPhi for all positive iEta values.

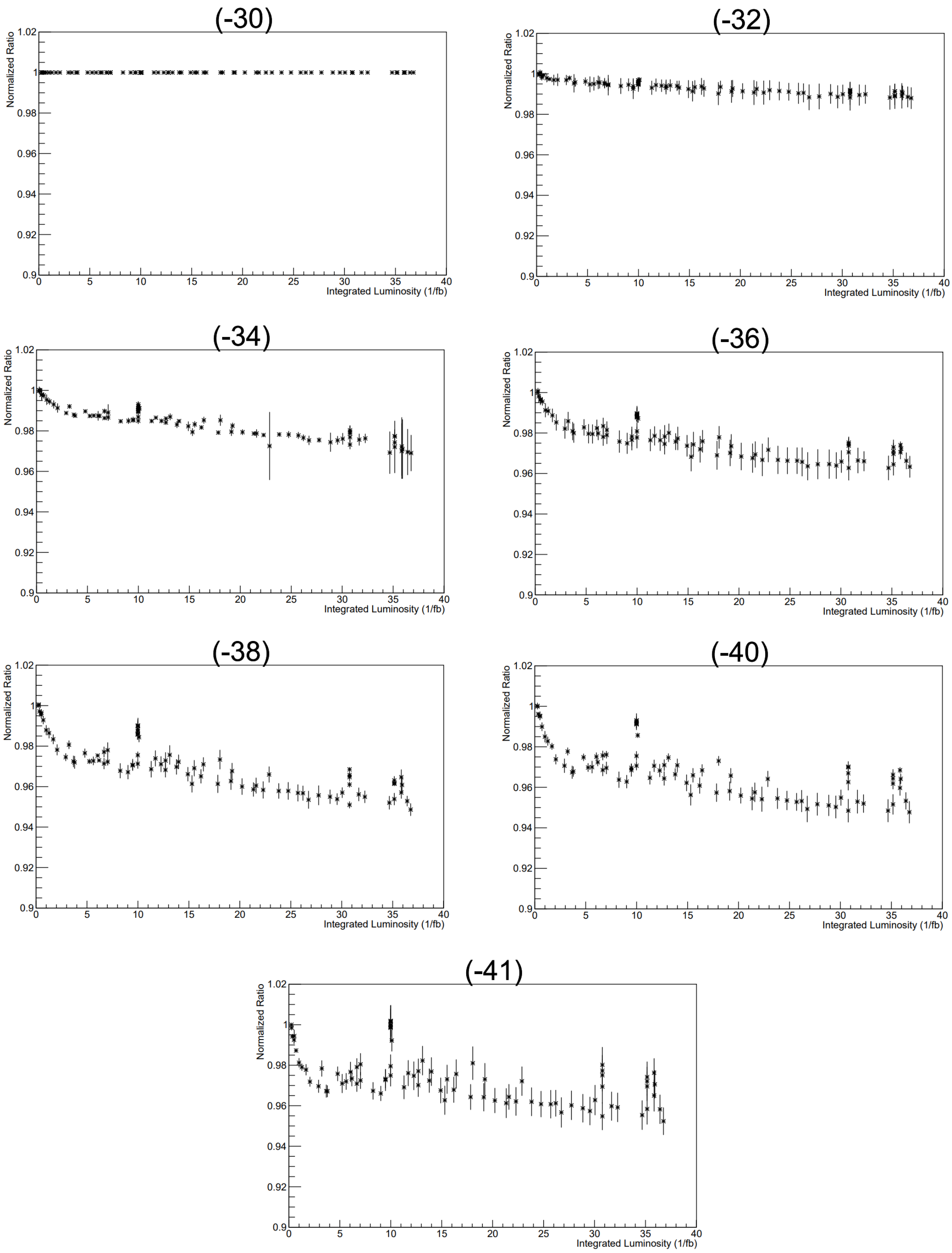

Figure E.4. Graphs of doubly normalized ratio with respect to integrated luminosity averaged over iPhi for all negative iEta values.

APPENDIX F: DOUBLY NORMALIZED RATIO PLOTS AVERAGED OVER IPHI FOR ALL IETA VALUES FOR RUNS IN LESS THAN ONE HOUR AFTER COLLISION

Doubly normalized ratio plots averaged over iPhi for all iEta values for runs in less than one hour after collision are given below.

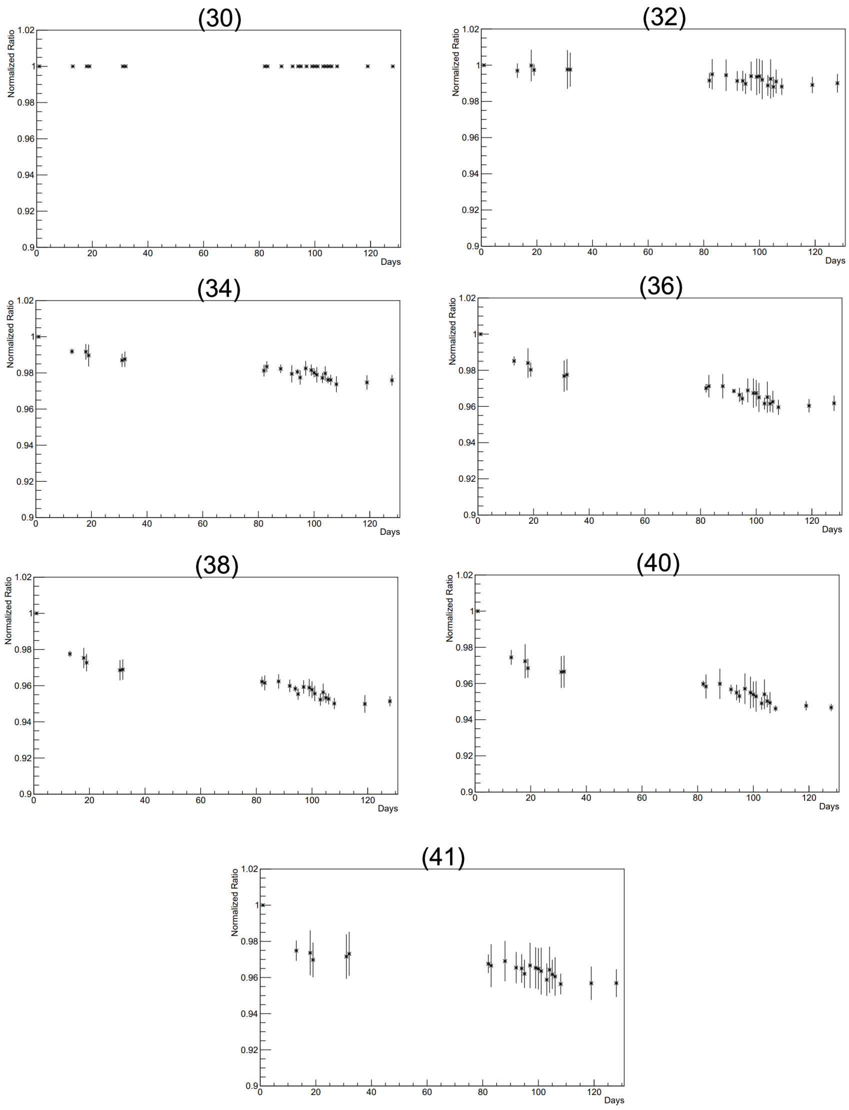

Figure F.1. Graphs of doubly normalized ratio with respect to time averaged over iPhi for all positive iEta values for the runs which took place in less than 1 hour after the nearest collision.

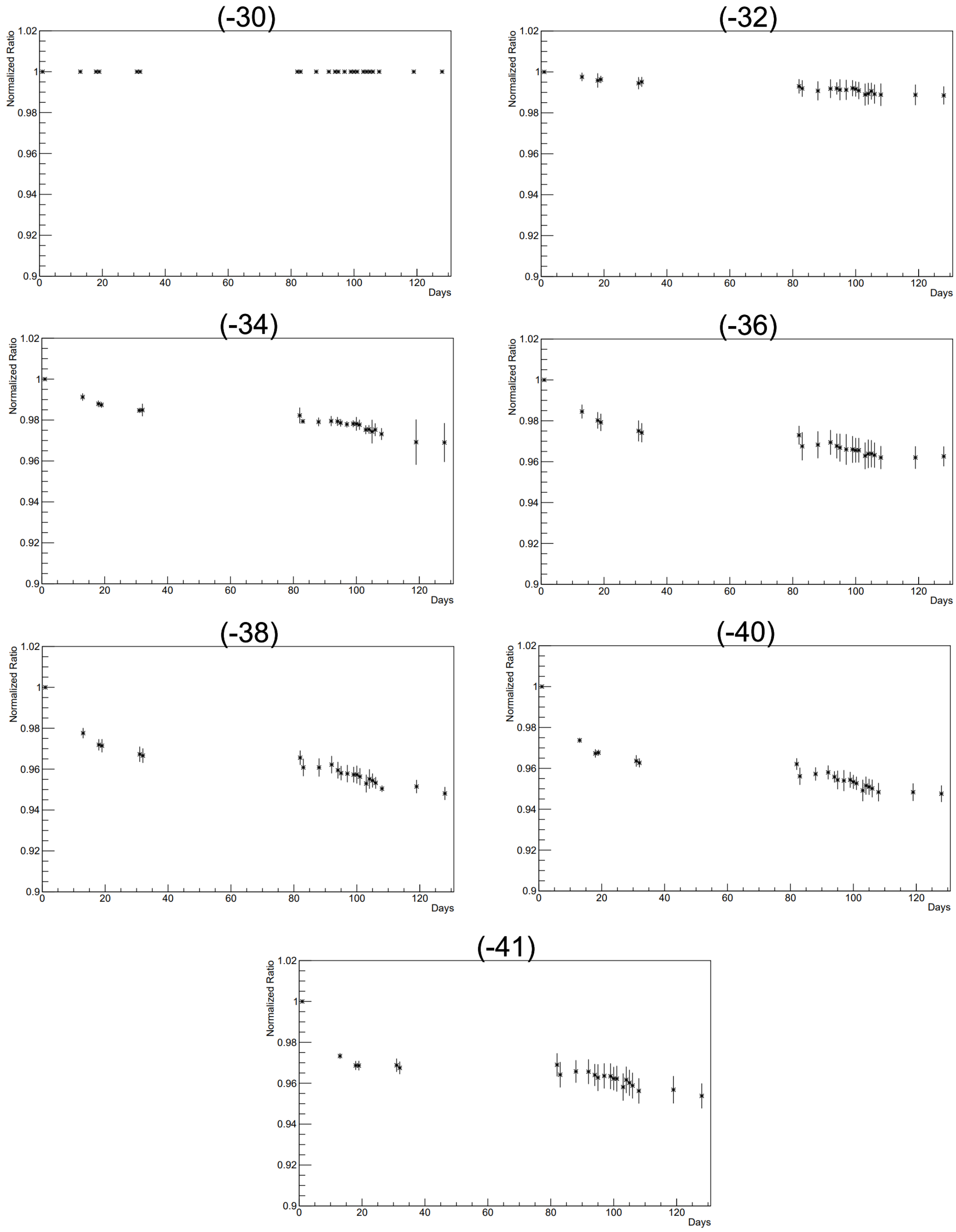

Figure F.2. Graphs of doubly normalized ratio with respect to time averaged over iPhi for all negative iEta values for all positive iEta values for the runs which took place in less than 1 hour after the nearest collision.

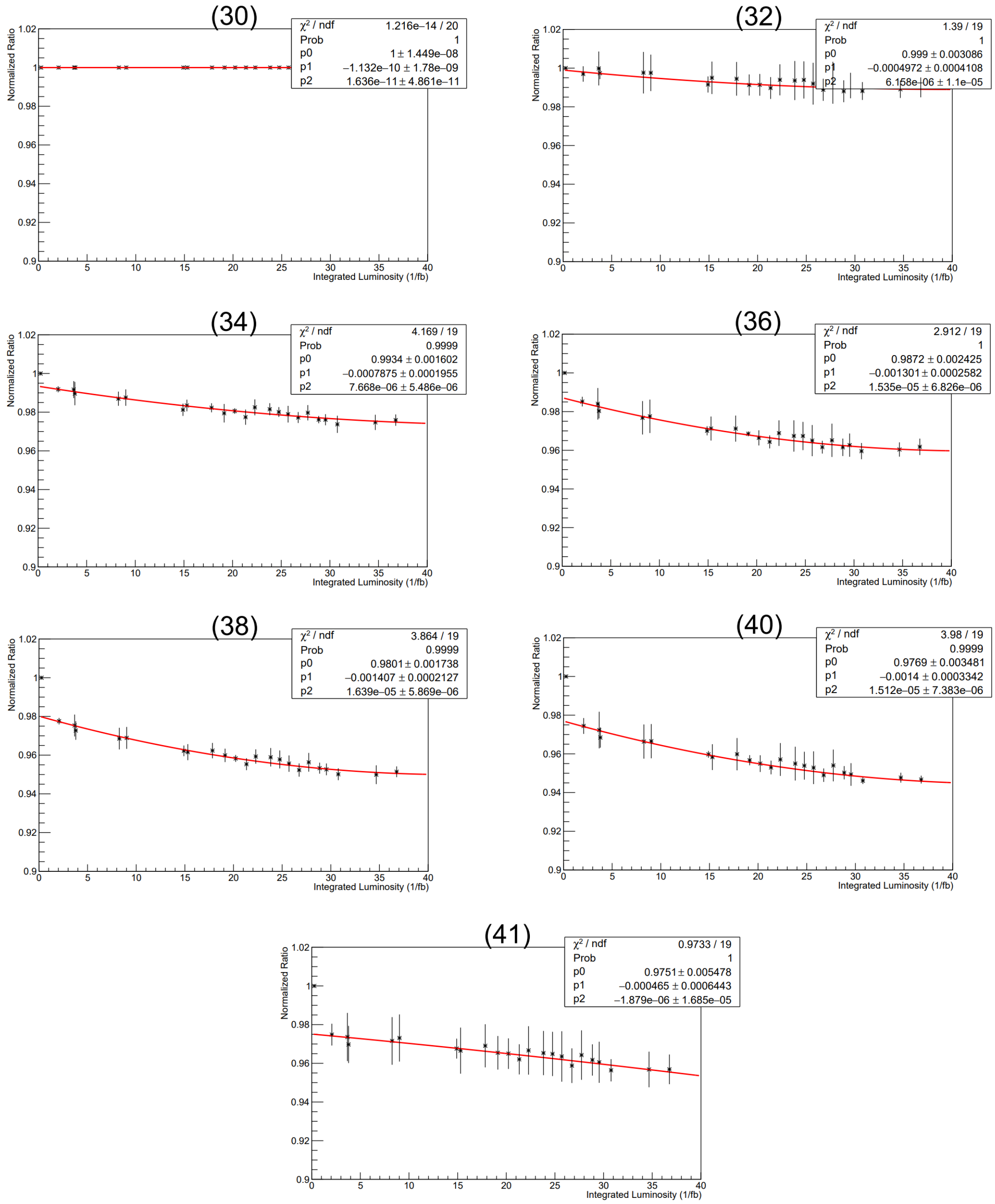

Figure F.3. Graphs of doubly normalized ratio with respect to integrated luminosity averaged over iPhi for all positive iEta values for the runs which took place in less than 1 hour after the nearest collision (with quadratic fit).

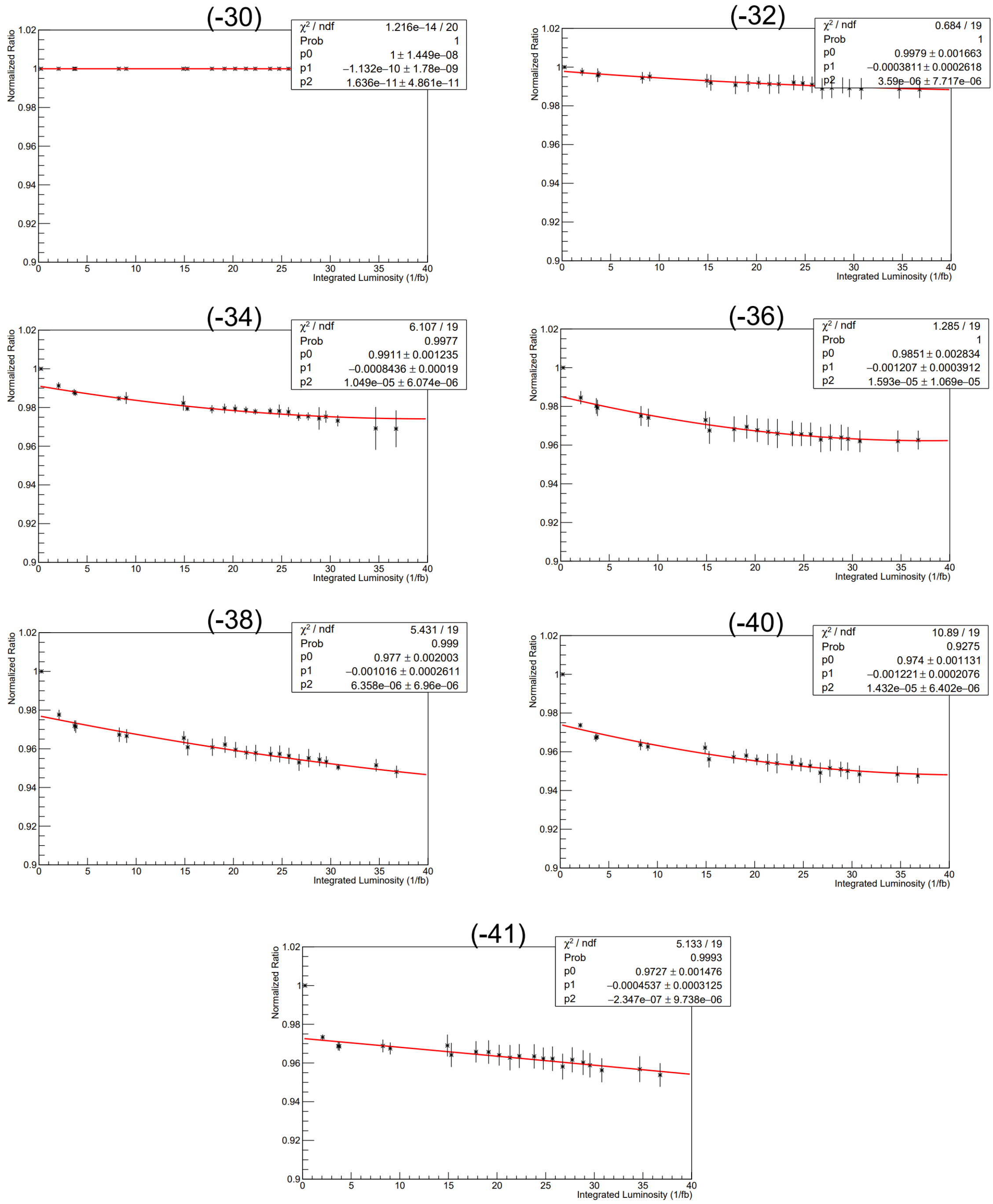

Figure F.4. Graphs of doubly normalized ratio with respect to integrated luminosity averaged over iPhi for all negative iEta values for the runs which took place in less than 1 hour after the nearest collision (with quadratic fit).

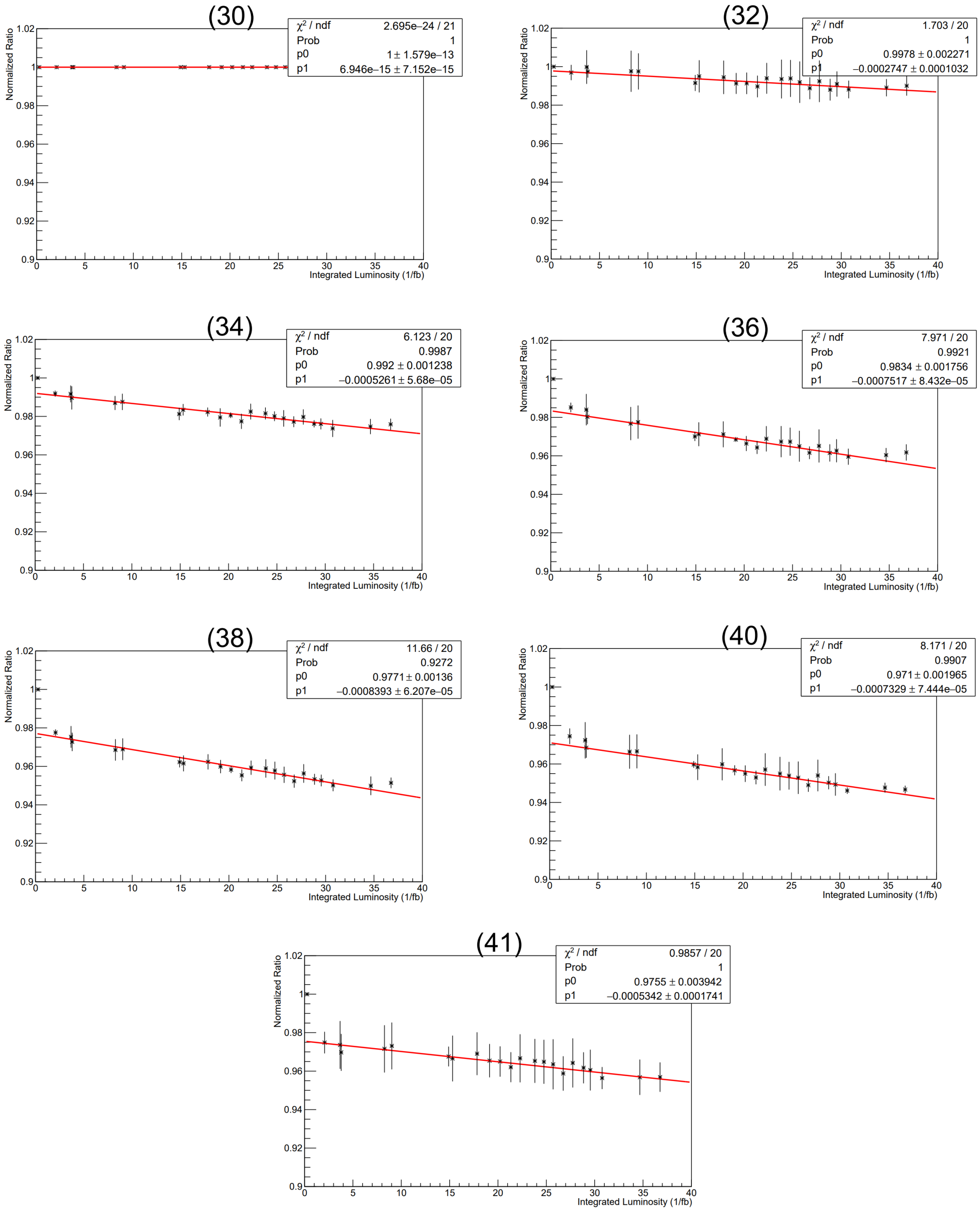

Figure F.5. Graphs of doubly normalized ratio with respect to integrated luminosity averaged over iPhi for all positive iEta values for the runs which took place in less than 1 hour after the nearest collision (with linear fit).

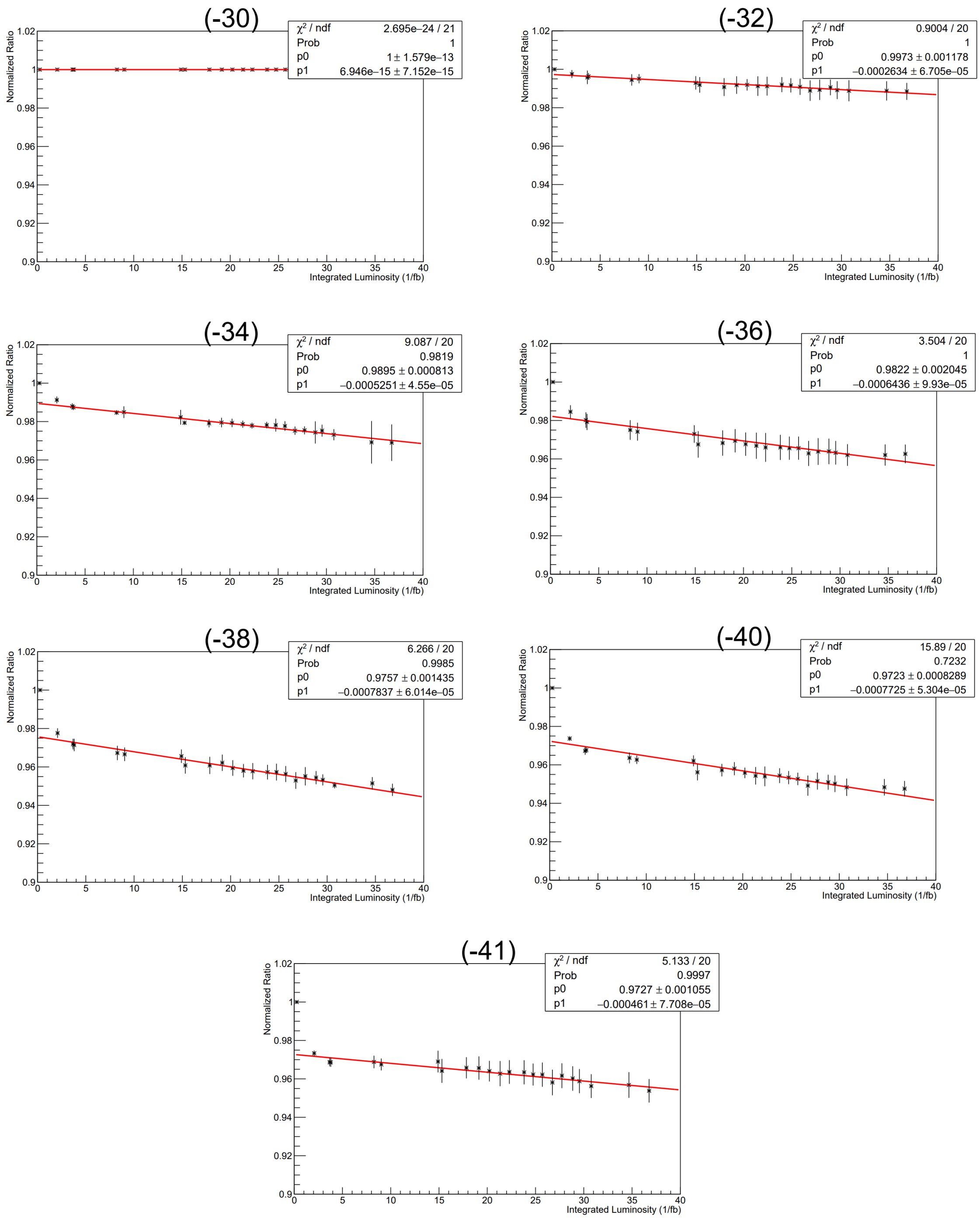

Figure F.6. Graphs of doubly normalized ratio with respect to integrated luminosity averaged over iPhi for all negative iEta values for the runs which took place in less than 1 hour after the nearest collision (with linear fit).